Linking the Characterisation of Cobalt-Bearing Copper Ore to Comminution Properties

Using a Geometallurgical Approach

L.T. Tijsseling

Linking the Characterisation of Cobalt-Bearing Copper Ore to Comminution Properties

Using a Geometallurgical Approach

by

L.T. Tijsseling

to obtain the degree of Master of Science
at the Delft University of Technology,
to be defended publicly on Wednesday October 18th, 2017 at 14:00 PM.

This thesis is confidential and cannot be made public until December 31, 2022.

An electronic version of this thesis is available at `http://repository.tudelft.nl/`.

TUDelft

Abstract

The metal cobalt is essential in creating a sustainable society, as it is an important component in lithium-ion batteries and wind energy turbines. About half of the Earth's land-based cobalt reserves can be found in the Democratic Republic of Congo (DRC). This study focusses on characterising cobalt-bearing copper ore from a DRC based mining operation and linking characteristic ore properties to the comminution behaviour. Portable X-ray Fluorescence (pXRF) is used to determine the geochemistry, while QEMSCAN, CT scan and InfraRed (IR) spectroscopy are used to assess mineralogy on different length scales. In terms of geotechnical properties, the surface hardness of the ore is determined using a rebound hardness tester. The comminution behaviour is assessed by crushing selected ore samples below 3.35 *mm* and by grinding the crushed samples for 21 minutes using a ball mill. The energy consumption required for different ore types is quantified using the crushing and sieving simulation package Bruno.

The chemical characterisation of ore samples showed significant variation in cobalt content, as the cobalt grade measured in the samples using pXRF varied from 0% to 33.5%. By applying QEMSCAN analysis to samples coming from different locations within the deposit, two different mineralogical zones have been identified: a weathered, and a sulphide zone, with large differences in modal mineralogy. In the weathered zone kolwezite and heterogenite are the principal cobalt bearing minerals, in the sulphide zone carrollite is the only mineral containing cobalt. The CT scan confirmed the unique mineralogy of certain samples, as the mineralogy of pure carrollite nodules found using QEMSCAN showed to continue in 3D. Both QEMSCAN and CT scan were able to detect differences in mineral texture of the studied samples.

In terms of geotechnical properties, differences between surface hardness of the samples were observed using the rebound hardness tester. An empirical formula has been derived to adjust the measured surface hardness of drill core samples with a mass below 300 grams. This formula aided in identifying the differences in surface hardness for the distinct mineral textures of the sulphide zone. Influence of mineralogy on the surface hardness has been observed, as areas containing only carrollite showed to have a lower surface hardness than areas with a mixture of Mg silicates, quartz and carrollite.

Fourier Transformed IR (FTIR) spectroscopy was used to identify a range of gangue minerals within the samples. Carrollite could be identified if it was present in significant proportions and no other IR active minerals were present. FTIR spectroscopy also allowed to refine mineralogical data, as it was possible to differentiate between talc or serpentine and muscovite or illite in the studied samples, which was not possible using QEMSCAN. In total 8 minerals were identified using IR spectroscopy. The relative proportions of the modal mineralogy showed to be in agreement with the mineralogy found through QEMSCAN.

The comminution experiments led to the identification of three different comminution classes. These three classes can again be linked to the identified mineral texture types. The surface hardness showed to be correlated to the p_{80} of samples with the same mineral texture. After 21 minutes of milling, the samples with a higher surface hardness had a coarser p_{80}. Simulation showed that the crushing energy requirements differ up to a maximum of 27% for different comminution classes. This research provides a foundation towards identification of geometallurgical domains in the sulphide section of the investigated cobalt-bearing copper deposit.

This MSc thesis was carried out at Camborne School of Mines (University of Exeter) as part of the NERC funded Cobalt: Geology, Geomicrobiology and Geometallurgy (CoG[3]) project.

Acknowledgements

A thesis can never be written without the right kind of support. First off, I would like to thank professor Hylke Glass for hosting me and for the time taken during the numerous meetings throughout the project. My gratitude goes out to dr. Mike Buxton, for allowing me to go to the United Kingdom for this project and for his help and suggestions on this thesis. My appreciation also goes out to dr. Jack Voncken, for taking place in the assessment committee and for evaluating my work.

I would like to thank Quentin Dehaine for his help and suggestions throughout the past six months, it was very helpful to have someone review the results and to exchange ideas with on a regular basis. The same goes for the technical staff at CSM, without their help and insights this project could not have been done. My gratitude also goes out to Marinus Dalm and Wouter van der Worp, for having taken the time to read my work and for their suggested improvements.

Besides that, the atmosphere in the PhD office and events out also made my time in Cornwall a very enjoyable one, so a big thanks to everyone who contributed to that!

And last, but definitely not least, I would like to thank my parents for their endless support and associated critical questioning of my decisions concerning both academic and extra curricular activities throughout my student life.

L.T. Tijsseling
Penryn, October 2017

Contents

List of Figures

List of Tables

1

Introduction

1.1. General Introduction

Metal extraction has followed a classical approach for as long as people can remember. A deposit is characterised based on the ore type, tonnage and metal grade that is present on a specific location (Moon et al. [66]). Due to an increase in demand for natural resources, but with a declination of grades and deposit sizes the industry needs to re-evaluate the way it utilises the current and future mineral deposits (Dunham et al. [26]). A method to improve the overall performance of the operation in terms of recovery and efficiency is through the use of geometallurgy (Lund and Lamberg [57]). By performing an in depth characterisation study and by evaluating whether comminution performance can be predicted using ore parameters, this thesis follows a geometallurgical approach.

1.1.1. Geometallurgy

Due to changes in the mining industry regarding environmental standards and on socio-economic level, there is a need for better understanding of the ore body of interest. Such an understanding contains more information than only mineralogy, tonnage and grade. Geometallurgy is a cross-discipline approach, that connects geology, mineral processing, metallurgy and mining (Lund and Lamberg [57]). The overall goal is to combine those disciplines and create a spatially predictive 3D model for mineral processing (Lamberg [52]).

At this moment there are few mining operations that actually apply geometallurgy in the planning and production process. One example is the Cu-U Olympic Dam mine in Australia, where the flotation and recovery parameters are used in mine planning (Liebezeit et al. [53]). It can be expected that geometallurgy will be used more in the future. The improved knowledge of the deposit reduces the overall risk of the operation and allows for a more accurate prediction of the economic evaluation (Jackson et al. [44]). Chapter 2 will give a more in depth outline on the concept and applications of geometallurgy.

1.1.2. CoG3

This MSc thesis is part of a larger NERC funded project that is known as Cobalt: Geology, Geomicrobiology, Geometallurgy: Investigating the Recovery of Cobalt (CoG^3). The goal of this consortium is to improve the cobalt production process and to ensure the supply of cobalt for the United Kingdom and the European Union in the near and distant future. This project has been divided in the following four work packages:

- Work package 1: New Sources of Cobalt

- Work package 2: Natural Biogeochemistry of Cobalt

- Work package 3: Bioprocessing of Cobalt

- Work package 4: Improving the Supply Chain of Cobalt

The University of Exeter is work package four leader. The supply chain can be improved by either discovering new deposits, securing the supply by improving the relationship between supplier and off taker or by

improving the extraction process of cobalt. The extraction process can be improved by using more environmentally friendly extraction methods, the implementation of innovating metallurgical methods or by making the extraction process more efficient. The latter can be done by introducing the use of geometallurgy in mine planning and production (National History Museum (NHM [72])).

1.1.3. Cobalt

Cobalt is a silvery metal and a transition element in the periodic table, positioned between iron and nickel. It has been used for the production of pigments for centuries, but it has been only since the 19th century that the metal industry started using cobalt for alloys and chemical processes (Mudd et al. [68]). More recently, it has been studied by Harper et al. [37] that 22 % of the annual cobalt production is used in superalloys, 22% in batteries, 11% in hard metals, 11% in catalysts and 27% in a range of more minor applications, such as pigments and tire adhesives.

As a result of the study of Mancini et al. [59], the European Union has identified cobalt as being a critical metal. The position of cobalt on the economic importance vs. supply risk chart is indicated by the arrow in Figure 1.1. The economic risk can be attributed to the requirement of cobalt in lithium - batteries and wind engine turbines, two aspects that are essential in making the current society more sustainable. In the mining industry cobalt is rarely recovered as the premium product (e.g. iron or copper), almost always as by-product (Mudd et al. [68]). NHM [72] states that 30% of the global cobalt is consumed in Europe, even though only 0.1% is produced on the continent.
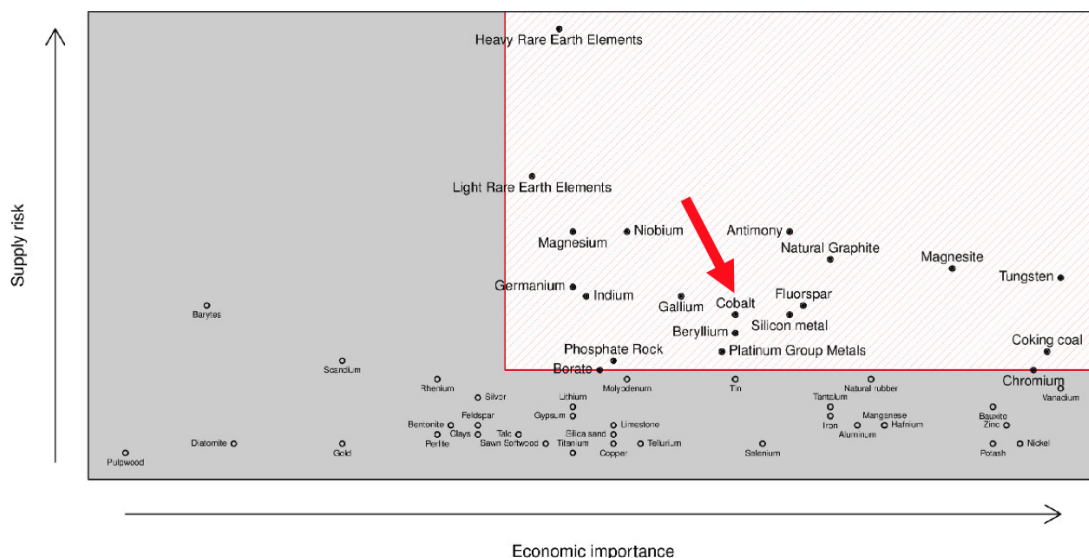
Figure 1.1: Economic Importance vs. Supply Risk of Metals - Emphasis on Cobalt (Modified after Mancini et al. [59])

According to Mudd et al. [68] the most important cobalt minerals are sulphides, such as cobaltite (CoFeAsS), siegenite (($Co,Ni)_3S_4$) and carrollite (($Co,Ni)_2CuS_4$). In general, cobalt mineralisation can be found in copper-cobalt sulphide, nickel-copper-cobalt sulphide or nickel-cobalt laterite ores. In all of those cases, cobalt is extracted as the by-product of the primary metal (nickel or copper). Mudd et al. [68] state that there are seven cobalt containing deposit types that are economically relevant. One of these is the stratiform sediment-hosted deposit, which is the deposit type studied within this thesis.

In the stratiform sediment-hosted deposits the cobalt mineralisation can be found in folded shales and dolomites that contain copper - cobalt sulphides. The most relevant region is the Katangan copper belt in Central Africa (Robb [82]). This region stretches over about 500 kilometres from Zambia into the Democratic Republic of Congo (DRC). The DRC is the leading country in both annual cobalt production and presence of reserves. The global cobalt mine production throughout 2016 and the global cobalt reserves as of 2016 are shown in Figure 1.2 (Ober [74]).
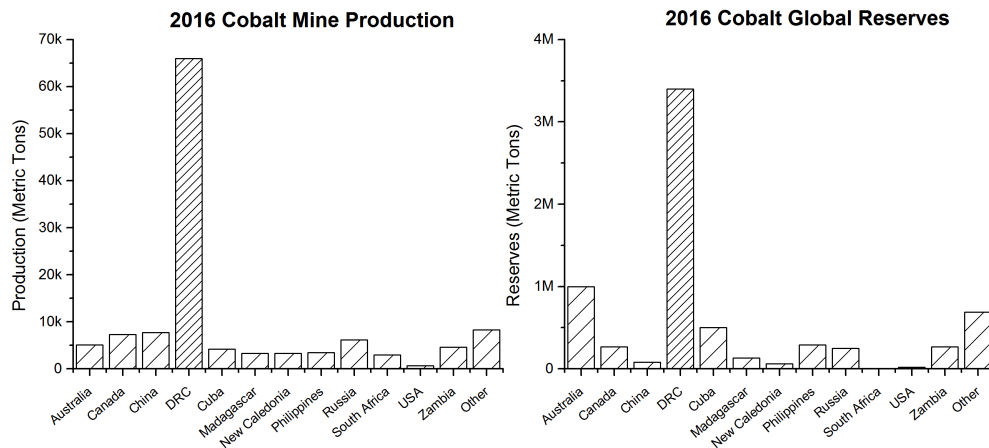
Figure 1.2: Overview of Global Cobalt Production and Reserves (Modified after Ober [74])

In 2016 more than 50% of the global cobalt production came from the DRC (66.000 out of 123.000 tons). With about half of the known land-based reserves also to be found in the DRC (3.4 out of 7 million tons), this is a trend that can be expected to continue for the upcoming years. Mining occurs using conventional open cut or underground methods (Crundwell et al. [23]). In the DRC cobalt is produced as a by-product of copper. Traditional methods are used to produce the cobalt, including crushing, grinding, flotation, leaching, solvent-extraction and electrowinning. It is estimated that about 44% and 26% of the cobalt is extracted for the sulphides and oxides respectively (Fisher et al. [27]). By considering cobalt not only as a by-product, it should be possible to improve those numbers. When considering Figure 1.2, one can understand the relevance for the global cobalt supply of optimising the cobalt extraction process of a DRC based mining operation.

Figure 1.3 shows the price change of copper (left) and cobalt (right) for the past five years. It can be deduced that an improved cobalt production process is also attractive from a revenue perspective for the DRC based miners. The cobalt price has been increasing in recent times due to a grow in cobalt demand and the lack of development of new mining operations extracting cobalt. Some experts say that this sudden increase may lead to an eventual downfall of the cobalt price cobalt and that the ramp up of the KCC mine in DRC will bring production and demand back into balance (Sanderson [87]). However, it is safe to say that the cobalt price will stabilise around a higher average compared to the price of the last five years.
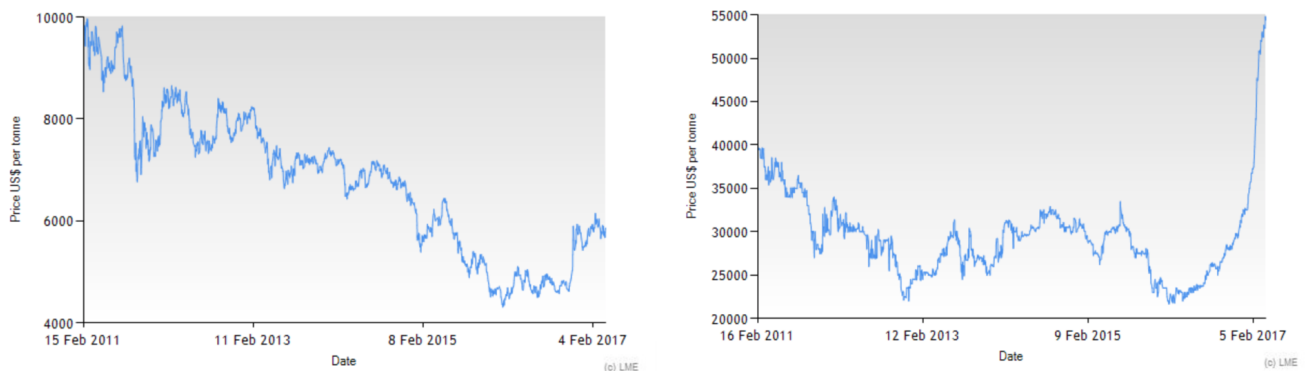
Figure 1.3: Overview of Copper and Cobalt Price per Ton (LME [54])

1.2. Project Outline

This project will focus on characterising cobalt-bearing copper ore and study whether it is possible to link measured ore characteristics to the behaviour in a comminution process. Ore samples have been supplied by a DRC based mining operation. The effectiveness of different characterisation methods will be evaluated and the comminution behaviour will be assessed in lab-scale experiments and through simulation. So far, studies carried out on cobalt in the DRC mainly have focussed on the metallurgical part of cobalt production

(Kongolo et al. [50], Fisher et al. [27], Swartz et al. [93] and Sole and Tinkler [91]), but have not considered the comminution. This section sets out the path taken during this project: the research questions, research objectives and methodology used.

1.2.1. Research Questions

The main research question can be formulated as follows:

Is there a correlation between the outcome of different characterisation techniques and the comminution properties of the ore present at the Mutanda Mining operation?

Based on this research question, several sub-research questions can be formulated to provide guidance throughout the project.

1. What is the variability in geochemical and mineralogical characteristics for different samples from the deposit?

2. Can a sensing technique, e.g. Infrared Reflectance (IR), be used to determine variation in mineralogy and the presence of a cobalt containing mineral?

3. Can differences in sample surface hardness be determined and be linked to mineralogical characteristics or comminution properties?

4. What is the influence of varying mineralogy and mineral textures on the comminution behaviour of carrollite containing ore?

5. What are the energy requirements for processing different ore types from the same deposit?

1.2.2. Research Objectives and Methodology

A schematic overview of the project is shown in Figure 1.4. To answer the research questions, the following objectives have been fulfilled using different methods:

- 1. Find the geochemical parameters. This is done using portable XRF, which is a non-destructive technique. The geochemical information will be used for selecting samples for further characterisation.

- 2a. Evaluate IR as a technique to determine different mineralisation types within the ore samples. IR is a non-destructive method. The applicability shall be evaluated using a part of the Mid InfraRed region: from 2500 to 15500 *nm*.

- 2b. Quantitatively describing the surface hardness. This is done using a rebound surface hardness tester. The applicability will be evaluated by studying in what range that type of equipment can be used, considering the measured differences on core samples and determining till what level of detail it is effective.

- 3a. Accurate description of the mineralogy, mineral textures and grain sizes using QEMSCAN. QEMSCAN will provide an automated mineralogical assessment that can be used for classification of the ore types. This data is again used to validate and classify the IR and surface hardness results.

- 3b. Three dimensional density assessment of selected samples. A CT scan shall be used to assess the continuity of the mineralisation found using QEMSCAN from selected samples in three dimensions.

- 4. Determine till what extent the ore parameters can be linked to comminution behaviour. To study that effect, laboratory based crushing and grinding tests will be performed on selected ore samples.

- 5. Quantify the industrial relevance of different comminution parameters by simulating a crushing sequence and comparing the differences in energy requirement. This is done using Bruno, a software package developed by Metso.
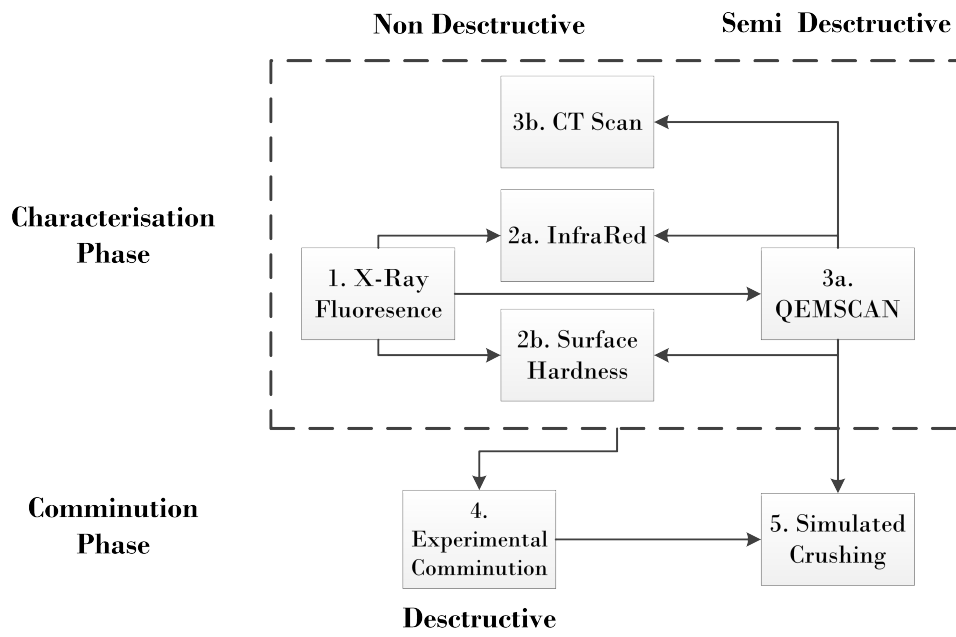
Figure 1.4: Overview of Distinct Operations within the Project

2

Geometallurgy

The goal of this chapter is to give a broad description about geometallurgy, outline the benefits and give examples of where it has been put to use. To do so, first an outline will be given about the classical approach to mineral resource extraction and metal production. This is followed by an outline of the concept and advantages of geometallurgy and concluded by reviewing geometallurgical applications.

2.1. Classical Approach

The classical approach here is what is considered to be a best practice route when developing a deposit into an operational mine site. This is the methodology used when working on a (pre-)feasibility study, based on Moon et al. [66], Benndorf [7] and the experience of the author.

Geologists define the deposit based on ore properties that define the boundaries and extension of the mineralisation. Information is provided about grades, tonnage and main ore and gangue types. The operators at the processing plant understand the impact of the feed grade on the processing properties. High grades imply easier processing properties and higher recoveries. Low grades make the processes more difficult. The ore types and lithology provided by the geologists can be linked to the metallurgical response of the ore. This variation in lithology can be large for extensive deposits. In the extraction sequence the main parameters are grades and tonnages, meaning that a variation of ore types can be present in the plant feed that is considered to be identical. A schematic view of the classical approach is shown in Figure 2.1. It must be noted that Phase I takes place before Phase II and that Phase II A and B take place parallel to each other.

1. **Phase I** - This is the phase where the deposit is discovered, investigated and turned into a resource. The deposit is normally discovered using geophysical methods, e.g. by considering anomalies in the magnetic field of the Earth. This is followed by exploration drilling, where drill core is studied for mineralogy, grade and indications of geological features. This data is used for the modelling and interpretation phase, where the drill core information is used for modelling an initial deposit. Using geostatistical techniques, parameters such as grade and mineralogy are estimated. Based on those estimations a mineral resource is created. If it turns out that the defined resource could have economic significance, the classical approach advances to Phase II A and B.

2. **Phase II.A** - The main point of focus in this phase is determining whether the economic significant deposit can also be extracted whilst making a profit. Based on the information obtained in Phase 1, a preliminary design of the mine is made. This is based on the main geological features and the location of concentrations of high grade areas in the deposit. If the resource is defined to be mineable, it is turned into a reserve. Based on the reserves an optimal mining sequence and an accompanying production schedule is set up. The production schedule combined with plant performance is an essential part in the economic valuation of the project.

3. **Phase II.B** - Based on the mineralogy and grade found during the characterisation of the deposit, a method is developed to extract the valuable constituents from the minerals. This is initially done using laboratory tests and followed by using those results as input for a computational plant. Based on the

results, a pilot plant is designed and tested. The results from the pilot plant test can be used as quantitative input for the plant performance, which combined with the production scheduling forms the basis for the economic valuation of the project.
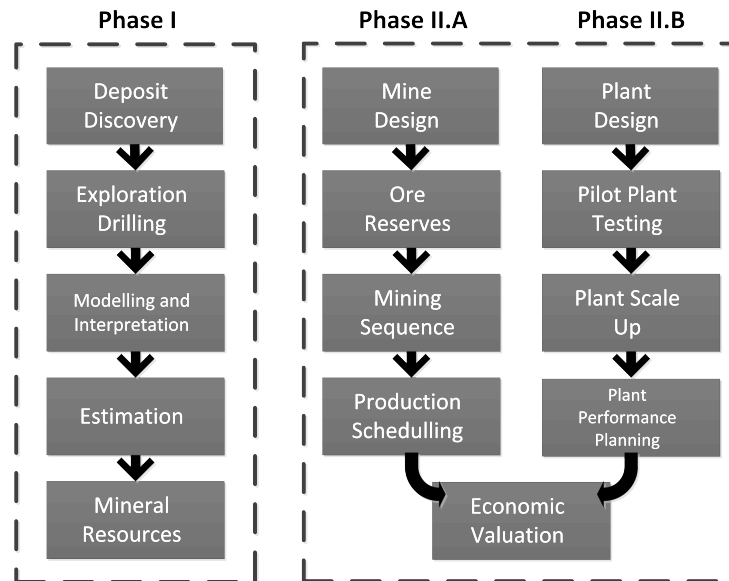
Figure 2.1: Schematic View of Classical Approach in Resource Extraction Development

Phase I and Phase II indicate the main steps taking place in characterisation of the deposit and calculating the economic value of the project. Even though this method is considered to be best practice in the mining industry, this sequence has not been updated or adjusted in recent times. In each step new methods have been tested, such as optimisation algorithms and different raffinate types used in solvent extraction, but the process itself has not been subject to change. This traditional approach to the evaluation of the mineral deposit has several shortcomings (Dehaine et al. [24]):

- In the deposit the ore is assessed only on variation of grades, tonnage and lithology.

- No information is present on spatial variability of metallurgical parameters throughout the deposit. These can be useful in predicting the performance of the processing plant.

- The risk management is done partially, as the risk of variation in the resource is not well evaluated. This increases the overall risk of investment in the operation.

- No knowledge on variation of metallurgical parameters can lead to non-optimal production.

- Non optimal production implies non-complete utilisation of the deposit.

It is clear that even though the classical approach covers all aspects required to construct a successful and risk assessed operation, it is not fully optimised when it comes to risk management and knowledge on the interaction of the different constituents of the operation. However, there is a concept that can be used to overcome these discrepancies and construct a fully integrated model.

2.2. Geometallurgical Approach

The concept of geometallurgy was first introduced in 1968 by McQuiston and Bechaud. It was stated that:
'...geo-metallurgy...since geology is inextricably interwoven with metallurgy in gaining an understanding of the complexities of a deposit, eventually leading to a definition of mineable reserves, with the development of a flowsheet and engineering criteria for the planning of a successful and profitable operation'. (McQuiston and Bechaud [62]).

Since the term first appeared, it has received a wide range of definitions. Jackson et al. [44] states that this variation can be attributed to the background of the person and purposes of the perspective. In general, the goal is to optimise the mineral processing by taking account for the geology, mineralogy, processing techniques and metallurgy for different domains within the deposit. This is done by combining geological and metallurgical information and use that to create a spatially based predictive model for mineral processing, that can be used in the production management or to integrate geology and mineralogy with resource processing and extraction (Lamberg [52]). This information combined into a model of the deposit is called a geometallurgical model. The knowledge of the ore body is improved, as the additional parameters provide more insights in the variability of the deposit and the eventual metal recovery.

In the last fifteen years the field of geometallurgy has been evolving rather fast. This can mainly be attributed to the development and increased availability of measurement methodologies and analytical techniques. Another reason is the increase in demand for raw materials and depletion of high grade and near surface mineralisation (Dunham et al. [26]). The industry can react to that by optimising the overall efficiency of a mining operation. A tool to optimise the efficiency is geometallurgy (Lund [56]).

According to Lund [56] there are three different modern views on geometallurgy. The first vision solely considers the ore, the spatial variation in the mineralogical factors and how to sample in a representative way. The spatial variability of processing behaviour is mentioned to influence the process, but no solutions are given on how to assess that variability.

The most common view considers quantifying variability to be an essential part of geometallurgy (Jackson et al. [44]). This perspective includes variation of processing parameters in the ore body. These parameters are used to optimise the mine design, mine scheduling and processing planning.

The third view is the broadest term and uses the term 'geometallurgical sustainability performance' (Jackson et al. [44]). This view discusses whether the geometallurgical field should incorporate more external factors that can influence geometallurgy on a global scale. These factors include mine planning, risk management, sustainability and geotechnics. A full geometallurgical model would require all these factors.

There are two different approaches that can be used to obtain the information required to construct a geometallurgical model:

- Mineralogical assessment: the goal of these tests is to determine the variation in mineralogy throughout the deposit. For similar particles a similar processing method can be used, despite differences in the spatial origin of those particles. Mineralogical features that need to be obtained are mineralogy, size, shape, liberation degree and density.

- Geometallurgical testing: this route focusses on directly measuring the metallurgical response of an ore. Based on analysing the response for a range of samples, one can determine how the different ore types throughout the deposit will behave in a metal extraction process. Examples of different experiments are geotechnical and chemical tests, such as uniaxial compressive strength tests and leaching experiments.

However, based on the mineralogical data a different metallurgical test could be required. It is thus also a possibility to combine the mineralogical assessment and geometallurgical testing to create a more complete geometallurgical model. According to Lund and Lamberg [57] there is a series of steps that need to be taken to create a fully integrated model, visualised in Figure 2.2:

1. Collection of geological data through drilling, drill core logging, geotechnical testing, chemical testing and mineralogical testing.

2. An ore sampling program where geological data is used to select the relevant samples for metallurgical testing.

3. Laboratory testing of the selected samples to determine the process model parameters.

4. Confirm the metallurgical relevance of the selected ore types and use these to create geometallurgical domains.

5. Develop or choose a correct mathematical relationship for estimating these geometallurgical parameters across the whole geological domain.

6. Set up a processing method that can be used to extract the valuable constituents from the ore. These are unit operations based on the variation of metallurgical parameters.

7. Evaluate the set up processing method using plant simulation with the metallurgical parameters as the input data set.

8. Calibrate the method by comparison with existing operations.
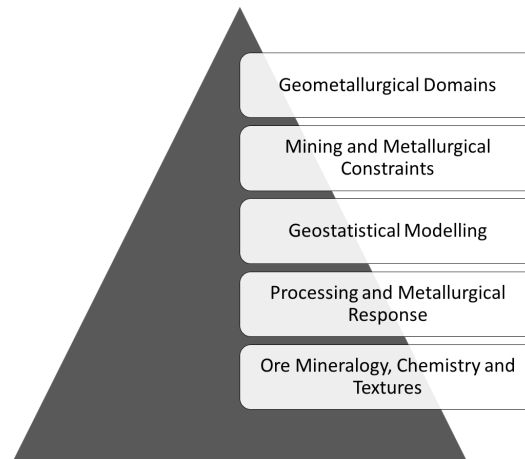
Figure 2.2: Different Phases within the Geometallurgical Concept (modified after Lund [56])

The geometallurgical domains mentioned at Point 4 are borrowed from geostatistics, where a domain is defined as a closed volume where grades follow the same rule. Establishing such a domain is an iterative process where geological data is used to divide the ore body in several domains, after which the differences between those domains are assessed using geostatistics. This process can be used for determination of the geometallurgical domains, which again is an iterative process. A review of the host rock, alteration, grain size, grade and structural geology is required (Lotter et al. [55]). This can be used to set up a block model, which is dividing the ore body into equal blocks containing the geometallurgical data. One important aspect to keep in mind is that not all parameters are additive. Grades are additive, but lithology is not. Comminution and metal recovery are not necessarily additive parameters. This will be a matter to keep in mind when creating the geometallurgical model.

When comparing the geometallurgical approach with the classical approach described in section 2.1 there are several advantages according to Lund and Lamberg [57]:

- The ore resources are better utilised due to the definition of ore boundaries in terms of predicted metallurgical performance.

- Metallurgical performance is improved as the metal extraction process can be fine-tuned based on the plant feed being know prior to inflow.

- The processing plant is optimised as there should be less variation in the plant feed.

- The mining sequence can be optimised due to increased knowledge of the orebody.

- Allows for implementation of new technological solutions, as ore-derived problems can be identified in time for significant research to be done.

- The overall risk of the operation is decreased, as the knowledge on the ore body is increased and there is a more controlled process chain.

- Larger chance of full economical optimisation of the operation.

2.3. Geometallurgy in Practice

The benefits can only be completely utilised when the geometallurgical model is available throughout the pre-feasibility stage (Lund and Lamberg [57]). Setting up the model when the operation is already taking place can lead to an improved strategy and financial forecast. An example has been demonstrated by Macfarlane and Williams [58], where a geometallurgical model was applied to an existing operation. This led to a shorter life of mine, but an improved cash flow from the original predictions: + US$127 Million in the revised situation. Lund and Lamberg [57] state that the main benefit of applying a geometallurgical model to an existing operation mainly comes from knowing what the limitation is of the material coming at different times, allowing to construct a realistic production forecast.

In 2011 Montoya et al. [65] used geometallurgical testing during the pre-feasibility phase of the La Colosa Au project, to differentiate between zones with similar comminution behaviour. Montoya et al. [65] differentiated between seven zones based on the response in comminution, evaluated using the Bond Mill Work Index and A x b tests. The results are shown in Figure 2.3. It was concluded that this aids in future mill and mine design and economic modelling of the resource. This was based on samples from 59 different drill holes. It was stated that more tests are required for definitive geometallurgical zoning of comminution.
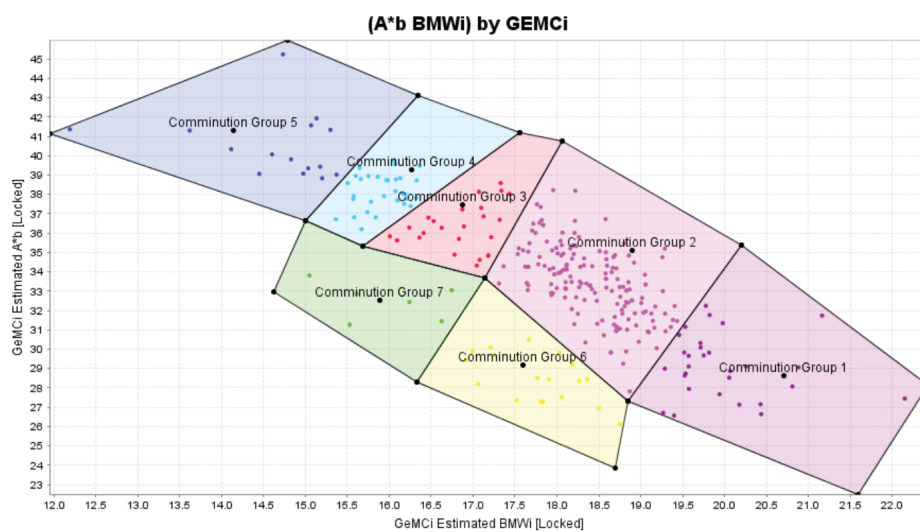
Figure 2.3: Division of Drill Hole Data in Comminution Zones (Montoya et al. [65])

Brissette et al. [14] used a similar approach, to refine the calculated costs associated with comminution throughout project development. Two new tests were developed: the SAG Variability Test (SVT) for SAG Milling and Bond Variability Test (BVT) for the SAG ground ore coming from the SVT. These two factors link variability in sample hardness to variability in comminution performance, thus more accurately predicting costs associated with the comminution process.

Vargas et al. [96] simulated the performance of geometallurgical characterised ore in a SAG mill. About 250 *kg* was characterised and divided into 10 geometallurgical units. For these zones actual plant performance information was used as the basis for a simulation in JKSimMet, leading to simulated comminution factors that would be assigned to the geometallurgical units. These factors were again used for the prediction of SAG mill performance in future production, making it a recursive calculation.

Geometallurgical testing was used in optimising the NPV of a Cu-Mo-Au project in Chile, by King and Macdonald [46]. An interesting aspect that is studied is the difference between the energy consumption following the average Bond Work Index and the Geometallurgical Bond Work Index. A slightly lower value is found using the geometallurgical approach, thus increasing the NPV. King and Macdonald [46] use a similar method to determine sulphuric acid consumption in the metallurgical process. All together the newly calculated Geometallurgical NPV is 10% higher compared to the NPV calculated following a classical approach.

Bennett and Rosa [8] published an example of where geometallurgy is used in a feasibility study. A model is developed that includes critical factors that influence the plant performance. The produced model mainly focusses on mineralogical features, such as differentiating between zones where chalcopyrite, pyrite or magnetite is dominant. However, mill performance factors are not yet included. Bennett and Rosa [8] emphasise

that in a future model, processing and metallurgical variability need to be part in order to construct an actual geometallurgical model.

At this moment not many publications can be found that evaluate the use of geometallurgy in actual mine planning and process optimisation. One example where a geometallurgical block model is used in mine planning is the Olympic Dam mine (Liebezeit et al. [53]). The designed block model contains 84 variables, including flotation recoveries and comminution properties. The characteristics of different zones are obtained by performing different tests on drill core and considering till what extent those characteristics can be spatially calculated using geostatistics. The parameters are used in the short, medium and long term mine planning and in the design of stopes. Liebezeit et al. [53] conclude that the incorporation of geometallurgical data makes the long term mine plane more holistic.

At a producing Chilean copper mine geometallurgical variables such as copper recovery and acid consumption are added to the resource model by Chait and Schiller [18]. The different zones vary between 60 and 80% for copper recovery and have an acid consumption that varies from 4.29 to 8.82 kg per ton. That is considerably different form the historical results, with an assumed copper recovery of 75% and acid consumption of 5.5 kg per ton. It is not mentioned whether this model is used in mine planning and production forecasting.

The comminution tests used in the previous studies require a large number of samples. Mwanga [69] developed a new method to define geometallurgical comminution domains using a small sample mass, under 0.5 kg. It is stated that all rock mechanical parameters that can be measured (e.g. UCS tests and point load tests) are material dependent and cannot be directly correlated to comminution performance. A relative comparison of different samples liberated following the same and simple comminution process is enough to distinguish between zones for mineral processing performance, but also contains enough information for simulations.

Mwanga et al. [70] continued to develop the method by performing an adjusted experiment with a range of ore types, leading to an empirical relationship that allows to link comminution data to the Bond Mill Index within a 5% accuracy. A similar approach is used in this thesis, the details associated with this experiment can be found in section 5.6.

3

Mutanda Mining - Overview

Mutanda Mining is a 100 percent Glencore owned subsidiary (Sheppard et al. [89]) that has been extracting ore since 2008 and has a life of mine of approximately 20 years. The main product that is produced on site is copper cathode, whereas cobalt is extracted as the only by-product (Glencore [31]). The mine is located in the South-West of the Democratic Republic of Congo, where copper has been extracted since the 1970s. A schematic view of the location of this mining operation is shown in Figure 3.1.

This chapter will consist of a description of the geological setting and the mining and metallurgical processes of the Mutanda Cu-Co operation. First, the geology and mineralisation will be discussed. This is followed by a description of the current operations and the chapter is concluded by an assessment of the future prospects of Mutanda Mining.
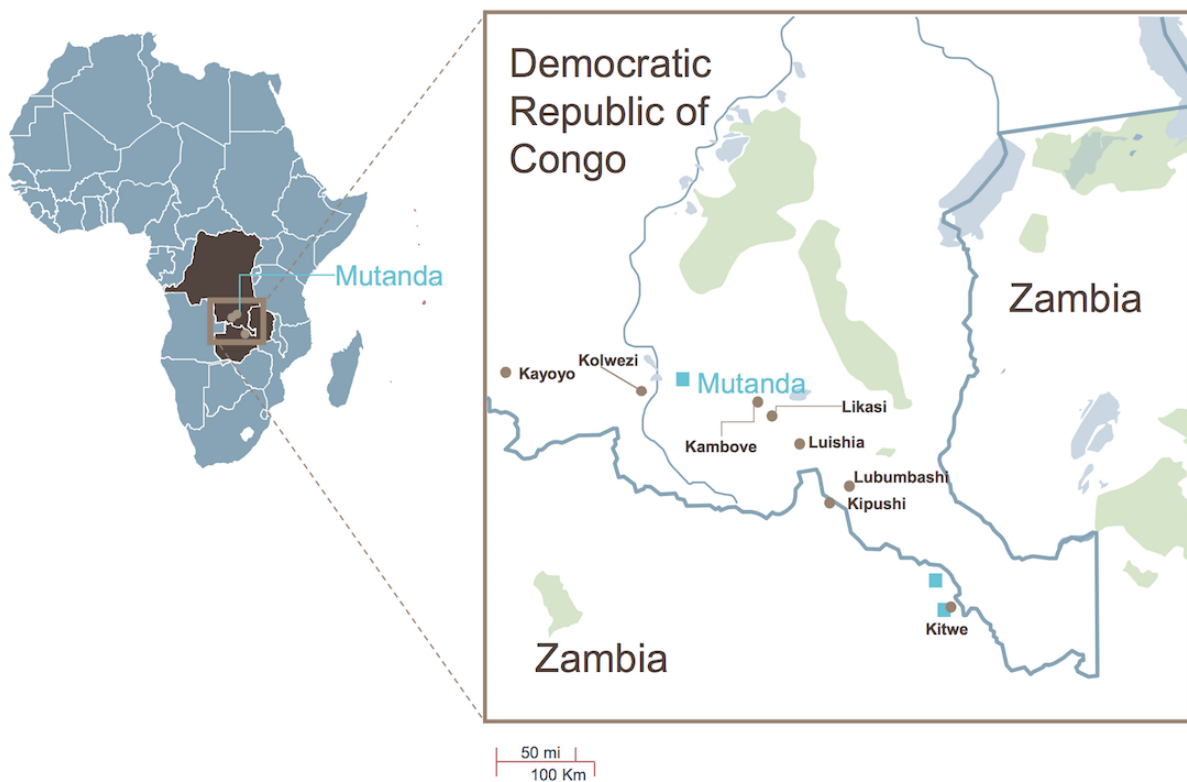
Figure 3.1: Location of Mutanda Mining on the African Continent and within the DRC (Glencore [31])

3.1. Geology

The project is located in the Katanga province of the DRC and part of the non-Proterozoic Central African Copperbelt. The total belt covers an area of 450 *km* by 260 *km* and is said to contain about one-tenth of the global copper reserves and half of the global cobalt reserves. The belt formed when the Kalahari craton and Congo craton collided (Crundwell et al. [23]). The part of the belt that runs through the south of the DRC and northern Zambia has a high concentration of sediment-hosted stratiform copper cobalt mineralisation (Mbendi [61]).

3.1.1. Regional Geology

The Mutanda deposit is located in the Congolese Copperbelt, covering an area of 350 by 50 *km*. The deposit shares characteristics with the majority of the deposits that lie within the Copperbelt, with stratiform mineralisation that is associated with carbonate/carbon-rich lithologies deposited in an evaporitic environment (Cailteux et al. [16]).

Within this belt there is a lower basement that consists of Eburnean age rocks, such as granites, gneisses and schists. This is overlaid by the Katangan Supergroup, that was deposited after emplacement and erosion of the granite (Herman [38]). This group is again subdivided into three main stratigraphic zones: the Roan, Nguba and Kundelungu groups, that again contain a number of sub units. A schematic overview of the stratigraphy is shown in Figure 3.2.
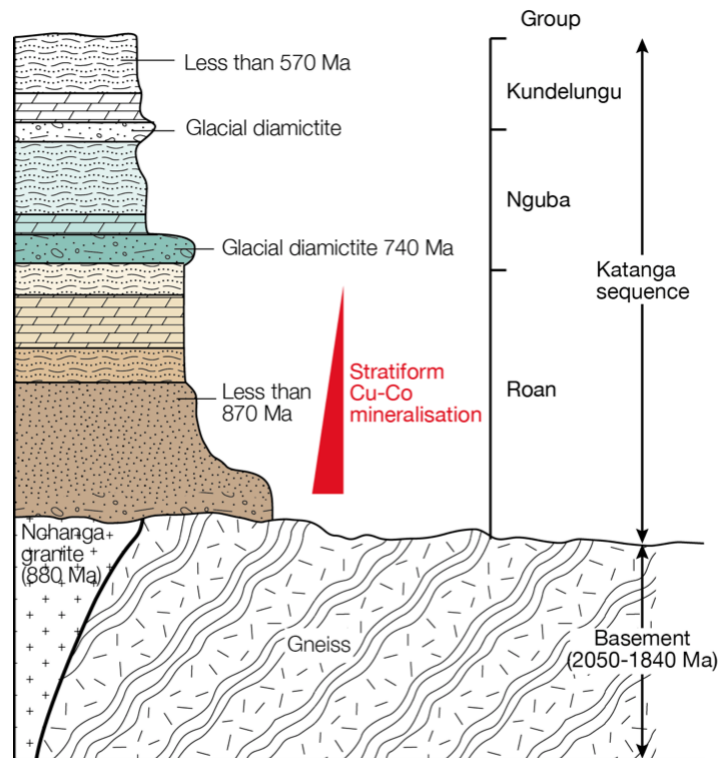
Figure 3.2: Schematic Overview of the Stratigraphy within the Katangan Supergroup (Dehaine et al. [24])

The Roan group is divided into four subgroups known to be the R1 (bottom) to R4 (top) subgroups (Cailteux et al. [16]):

1. R.A.T. (R1)
   Abbreviation of *Roches Argilo Talqueuses*, mainly consisting of massive or irregular detrital formations that contains hematitic, reddish, chloritic and dolomitic siltstones. In general, detrital quartz, micas, chlorite and dolomite can be found in most bands. No sulphides are found within this zone.

2. Mines (R2)

This is a carbonate unit, containing the richest stratiform copper-cobalt mineralisation, as indicated by the gradient in Figure 3.2. The zone is again divided into three subzones, based on three different marine environments.

3. Dipeta (R3)
   The Dipeta zone consists of four different formations. Mainly argillaceous and siliciclastic formations are found at the base and carbonate formations at the top.

4. Mwashya (R4)
   The transitional sequence goes into a finer and reduced clastic sequence that is accompanied by mafic intrusion and volcanism.

Due to numerous major techno-thermal events the belt has stretched into a convex arc. Throughout the arc, deposits are found in the external fold and thrust belts. The economic deposits are mainly found in one tectonic structural feature: the Kafue Anticline. That is known to be a late tectonic structural feature consisting of Katangan Supergroup meta sedimentary rocks (Herman [38]).

The origin of the sediment hosted stratiform copper cobalt deposits has so far been a controversial subject. The main theories are syngenetic hypothesis, where sulphide precipitation results directly from anoxic seawater, epigenetic hypothesis (related to magmatic intrusions or late hydrothermal) and diagenetic hypothesis. The metallogenic history of the Katanga province is complex and a wide range of mineralisation styles have been recorded, including stratiform copper-cobalt mineralisation and iron-oxide-copper gold occurrences (Herman [38]).

Traditionally, the Copperbelt ore deposits are considered to lie within the Lower Roan Subgroup and are composed of coarse siliciclastics (conglomerate to arkose and siltstone, with fewer carbonate rocks). The stratabound mineralisation is restricted to host rocks in the Mines (R2) and Mwashya (R4) Roan Subroups (Herman [38]). An overview of the different mining operations and stratigraphic groups in Southern DRC is shown in Figure 3.3.
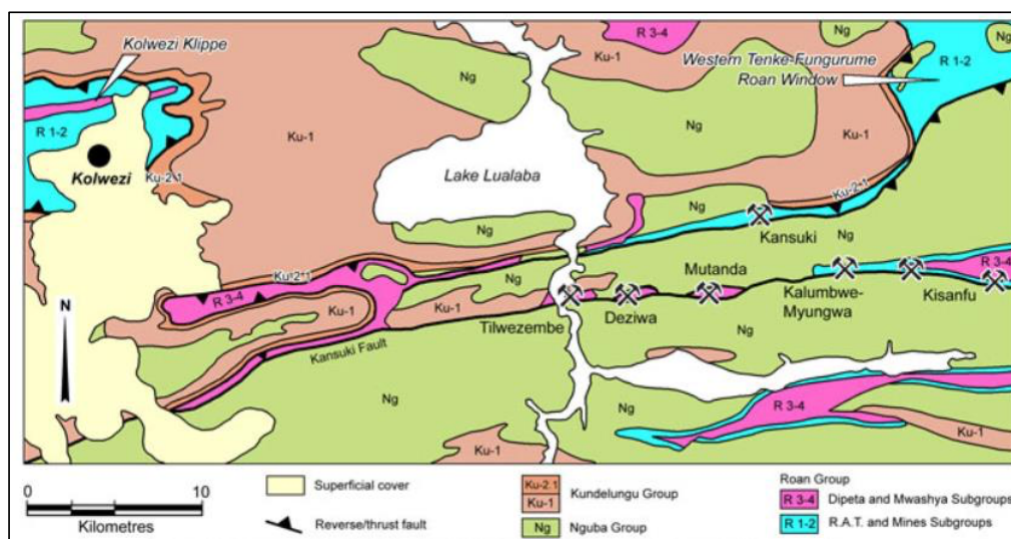
Figure 3.3: Schematic Overview of the Geology of the South of the DRC and Northern Zambia (Herman [38])

3.1.2. Project Geology

The Mutanda deposit is located within a thrust slice of the Roan Group sedimentary rocks, developed within the steeper Kansuki fault zone. The majority of the copper cobalt deposits are stratigraphically controlled and occur in the Mines subgroup. The orebodies can extend for hundreds of meters to several kilometres, but are often interrupted by faults. In general, there is lateral variation of the sulphides within the mineralised layers, with copper-rich ores grading into copper-poor ores. Other copper-cobalt sulphide mineralisation occurs in dolomites of the lower Mhashya, with Mutanda being one of those deposits.

The Kansuki fault zone is a major dislocation that stretches out for approximately 75 *km*. In that fault zone the South part of Mutanda is located. The main stratigraphic units include R3 and R4 of the Roan group, but also two subgroups of the Nguba group. In general, there is poor exposure of the property rocks as these lie under a cover of red soil and laterite, with local nodules of heterogenite (Herman [38]).

The oldest and highest zone is the Dipeta R3 zone, consisting of argillite. This zone is highly weathered and contains broken and jointed surfaces. In general, the R3 is weathered to greater depths compared to the other units. No fresh rock was intersected in the boreholes, these all pass through on the way to the R4 zone. Near the surface the R4 zone is highly weathered and contains significant amounts of copper-cobalt oxide mineralisation. Both malachite and heterogenite occur in these zones, but in varying proportions. Other near surface alteration includes silicified, friable iron-rich oxide material. In the Central Zone there is a collapse breccia filled with iron altered rock.

In the deeper part of R4 region a very different zone is found, mainly consisting of recrystallised stroma-tolitic dolomite with veins and disseminations of chalcocite, carrollite and sometimes bornite. In the lower parts the dolomite is interlayered dolomitic argillites that are finely bedded containing disseminations of veinlets with copper and cobalt sulphides. In the upper part of the R4 unit one can find a hematite layer that is in close proximity with a thin jaspilite layer. Above the dolomite layer there is a black shale layer that is highly mineralised with sulphides. A schematic overview of the project geology is shown in Figure 3.4.
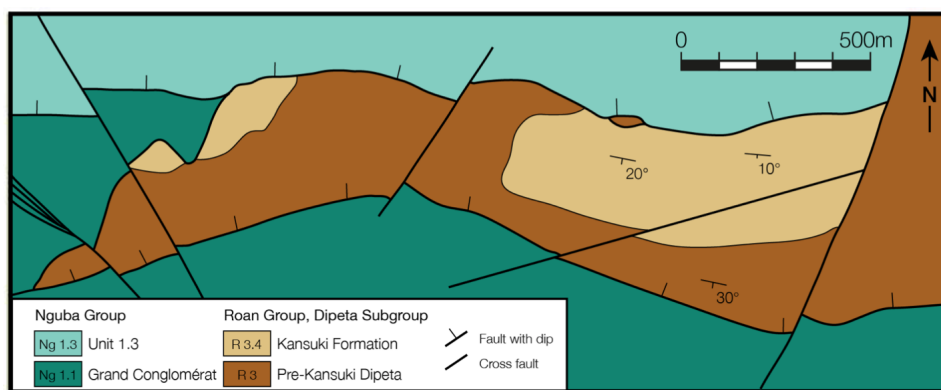
Figure 3.4: Schematic Overview of the Project Geology (Dehaine et al. [24])

According to Robb [82], the metasedimentary rocks that form the Katagan supracrustal sequence were deposited in an initially terrestrial and Aeolian environment. That environment became marginal marine due successive layers being laid down and flooding of seawater overland. Temporary anoxic conditions gave rise to intercalations of evaporitic rocks in the siliciclastic carbonate successions. The Mutanda South deposit has characteristics that are relatively similar to most of the other Copperbelt deposits that are hosted by carbonate or carbon-rich units of the Roan group.

3.1.3. Mineralogy

There are different mineralisation zones present in the Mutanda deposit. In general, it is possible to differen-tiate between a weathered zone, a sulphide zone and a transitional zone in between (mixed). From a resource perspective there are three main ore zones: the larger East, the Central and North West zones. The oxidised minerals are mainly present in the Central zone and North West zone. This is also the case for the upper part of the East zone, but sulphides appear at greater depths (Herman [38]).

This East area contains the largest ore body, following a strike along the South East - North West direction for 1500 meters, extending up to 800 meters below surface. The zone of interest is the R4 dolomite zone, with sulphides intersecting at depth. That area does require a more in depth investigation. The Central area extends along a North East to South West strike for about a 1000 meters, going to 200 meters in depth. The majority of the minerals in this area are oxidised, but there are portions of sulphides found as well. The North West zone has similar parameters as the Central zone, but a shallower vertical extend (Herman [38]).

The main copper oxide minerals are malachite and pseudomalachite. For cobalt, the identified minerals are heterogenite and lithiophorite. Quartz and chlorite are the main gangue component in the samples. Other gangue minerals that have been identified are iron and aluminium oxyhydroxides, including hematite and

goethite, and clays, such as kaolinite. The mineralogical make up differs per sample, but variable amounts of malachite, pseudomalachite and heterogenite are associated with fragments of quartz, quartz-chlorite and quartz-illite. In some cases, an intergrowth of these minerals is found. Almost in all cases both malachite and heterogenite are found to be intergrown with quartz and chlorite. An overview of the main copper, cobalt and gangue mineralisation in the weathered zone is shown in Table 3.1.

Table 3.1: Overview of the Minerals in the Weathered Zone of the Mutanda deposit (Dehaine et al. [24])

	Mineral	Valuable Material	Formula	Relative Abundance
Valuable	Malachite	Copper	$Cu_2CO_3(OH)_2$	+++
	Pseudomalachite	Copper	$Cu_5(PO_4)_2(OH)_4$	+
	Heterogenite	Cobalt	$CoO(OH)$	++
	Lithiophorite	Cobalt	$(Co,Mn)O(OH)$	+
Gangue	Quartz		SiO_2	++
	Chlorite		$(Fe,Mg,Al)_6(Si,Al)_4O_{10}(OH)_8$	+
	Illite		$(K,H_3O)(Fe,Mg,Al)_2(Si,Al)_4O_{10}[(OH)_2,H_2O]$	+
	Hematite		Fe_2O_3	+
	Goethite		$FeO(OH)$	-
	Gibbsite		$Al(OH)_3$	-
	Kaolinite		$Al_2Si_2O_5(OH)_4$	-

The major copper sulphide minerals have found to be chalcopyrite and bornite. For cobalt, the main sulphide mineral is carrollite. The copper sulphides finely disseminate along bedding planes in the dolomitic argolites and in the dolomite. Carrollite has a similar behaviour, but is more fine grained than both the copper sulphides. The copper-cobalt sulphides are both finely intergrown with quartz and also have a presence of chlorite and dolomite. Carrollite occurs as two different types of mineralisation, being present as larger crystals (up to 3 *mm*) in the dolomite and argillic rocks. The second type of mineralisation is similar to a type found in the Kamoto and Kambove deposit (Dewaele et al. [25]), in dolomite associated small veinlets. An overview of the main copper, cobalt and gangue minerals in the sulphide zone is shown in Table 3.2.

Table 3.2: Overview of Minerals in the Sulphide Zone of the Mutanda deposit (Dehaine et al. [24])

	Mineral	Valuable Material	Formula	Relative Abundance
Valuable	Chalcopyrite	Copper	$CuFeS_2$	+++
	Bornite	Copper	Cu_5FeS_4	++
	Chalcocite	Copper	Cu_2S	+
	Carrollite	Cobalt	Co_2CuS_4	+++
Gangue	Dolomite		$CaMg(CO_3)_2$	++
	Quartz	-	SiO_2	++
	Chlorite		$(Fe,Mg,Al)_6(Si,Al)_4O_{10}(OH)_8$	+
	Illite		$(K,H_3O)(Fe,Mg,Al)_2(Si,Al)_4O_{10}[(OH)_2,H_2O]$	+

The sulphide mineralogy has not been studied in great detail at Mutanda, both in literature and by the provided consultancy reports. It was mentioned by Herman [38] that the deposit has similar features to the other deposits in the Congolese Copper belts. Dewaele et al. [25] did an in depth study to the origin of the Cu - Co sulphide deposits in the Katanga region and stated that there are two periods of mineralisation:

- First mineralisation phase - consists of pyrite precipitation with disseminated copper and cobalt sulphides in nodules and lenses. These are often present as pseudomorphs after evaporites.

- Second mineralisation phase - characterised by the occurrence of copper and cobalt sulphides in dolomite and quartz veins, cross cutting the nodules and lenses of the first mineralisation phase and replacing the pyrite.

Of these different mineralisations the petrography was analysed as well. Mutanda is not specifically mentioned, but the neighbouring Kambove deposit is considered. This can give an indication whether other types of sulphide mineralisation can be expected at Mutanda. Dewaele et al. [25] state that two different types of samples are present, related to the first and second mineralisation phase. The first phase is associated with authigenic quartz and contains chalcopyrite, bornite, digenite and chalcocite. The second type consists of dolomite small veinlets, where the dolomite is coarse and is observed together with carrollite, as discussed previously. It is mentioned that the found mineralogy is again similar to the Kamoto deposit, neighbouring Mutanda on the other side.

3.1.4. Resource Estimation

The resources and reserves have been defined for the different pits, but not the mineralogical zones of the deposit. The most recent update performed by RHC Consultancy, considers the complete deposit without differentiating between the different mineralogical zones. In 2013 a life of mine was expected of 20+ years, assuming measured resources of about 100 Million tons. The resource estimation for the complete deposit is shown in Table 3.3 (Glencore [31]).

Table 3.3: Resource Estimation Mutanda Deposit as of 31st of December 2012 (Glencore [31])

Category	Tonnage	Copper	Cobalt
Measured Resources	96.5 Mt	2.05%	0.64%
Indicated Resources	28.4 Mt	1.52 %	0.77 %
Inferred Resources	166.6 Mt	1.00 %	0.47 %
Total	291.50 Mt	1.4%	0.47 %

3.2. Current Operation

Based on a site visit in 2017, there are three open pits from which ore is extracted from the weathered part of the deposit. The copper grade is leading in extraction sequencing and the cobalt is seen as bonus. The amount of copper and cobalt are the only two parameters that are used in the resource model (Tijsseling [95]). According to Crundwell et al. [23] the weathered part of the deposit is easily mined, using a mix of surface scrapers, bulldozers and diggers. Mutanda uses a combination of blasting and diggers (Tijsseling [95]). The three pits coincide with the three mineralogical zones in section 3.1.2. It is expected that the three different pits merge into one large pit by 2018. At this moment the pits have the following characteristics:

- Central open pit - mined to a depth of 60 meters below surface. Currently no ore is extracted.

- East open pit - mined to a depth of 85 meters below surface. Extracting a mix of sulphide and weathered ore, in 2017 the mixed ore led to issues with acid consumption in the leaching plant.

- Central North West open pit - mined to a depth of 75 meters below surface. This is the primary ore feed for the plant as the weathered ore from this pit is consistent and leads to fewer issues with the subsequent processing.

A schematic view of the transition of a pit from weathered zone (1), to mixed zone (2 - both weathered and sulphide ores) to a sulphide zone (3) is shown in Figure 3.5. At this moment the East pit is extracting ore from zone 2 and the Central North West pit from zone 1.
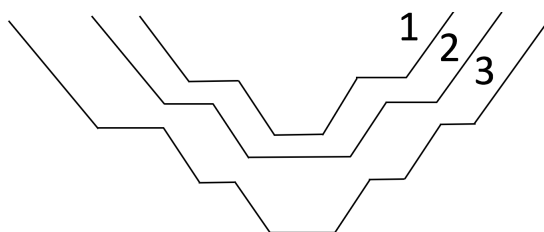
Figure 3.5: Schematic View of Three Different Mineralogical Zones Within One Pit

3.2.1. Metal Extraction Process

After the ore has been extracted from the pit the next step is processing the ore, removing the gangue material and extracting the metal from the valuable minerals. Mutanda Mining has provided simplified flowsheets of the current process. A schematic version of the flowsheet is shown in Figure 3.6. No details were provided about the equipment or chemical reactions taking place. Copper production is the main focus at Mutanda Mining, cobalt is only produced as a by-product. The following steps are taken in the copper and cobalt production plant to produce the two different products (Tijsseling [95]):

1. Run of mine ore comes into the processing plant and is initially reduced in size through crushing and grinding. The goal of this is to liberate the valuable ore from gangue ore and to create a larger surface reaction for the leaching. There are four different jaw crushers operating, followed by a SAG mill, ball mill or a combination of those two. A hydrocyclone is used to circulate the oversize ore back into the mill. Over the years additional comminution phases have been constructed in line with an increase in mine production.

2. In the leaching phase polluting elements are removed from the valuable minerals. The product from the comminution phase is leached using sulphuric acid and sodium-metabisulfite. The residence time is optimised for the copper to be leached, leading to a significant amount of cobalt ending up in the tailings.

3. The Pregnant Leach Solution (PLS) is concentrated using a CCD. Two sets of six concentrators are used. The benefit of this is that the leaching solvent can be re-used and that a smaller product volume goes to the solvent extraction phase. The tailings are re-fed into the final concentrator, leading to an increase of the silicate concentration in the concentrated PLS.

4. In the Solvent Extraction (SX) phase the copper and cobalt containing phases are separated from each other. The copper is extracted from the PLS and loaded on an organic phase, which is fed into the electrowinning plant. The remaining valuable elements in the SX raffinate are taken to the cobalt plant. The raffinate is also fed into the milling operation.

5. The precipitated copper is turned into copper cathode using electro winning.

If the cobalt percentage is above a certain threshold, it will enter the cobalt plant. If not, it will re-enter the copper production plant. At this moment also a significant amount of copper is entering the cobalt plant. An additional phase is constructed in order to precipitate the copper.

1. Iron and manganese are removed from the stream received from the copper production plant. Both are precipitated by increasing the pH. The pH is altered using lime. The precipitated material is referred to as iron manganese cake, that is stored for potential future use. The copper entering the cobalt plant is also removed at this stage.

2. Cobalt is precipitated as cobalt hydroxide, using magnesium.

3. The cobalt hydroxide is filtered and dried, after which it is ready for transport.

The cobalt recovery is not optimal, as it was mentioned that a longer leaching time would improve the cobalt production. That is not considered to be an option, as that will have a negative effect on the copper production.

Copper Production
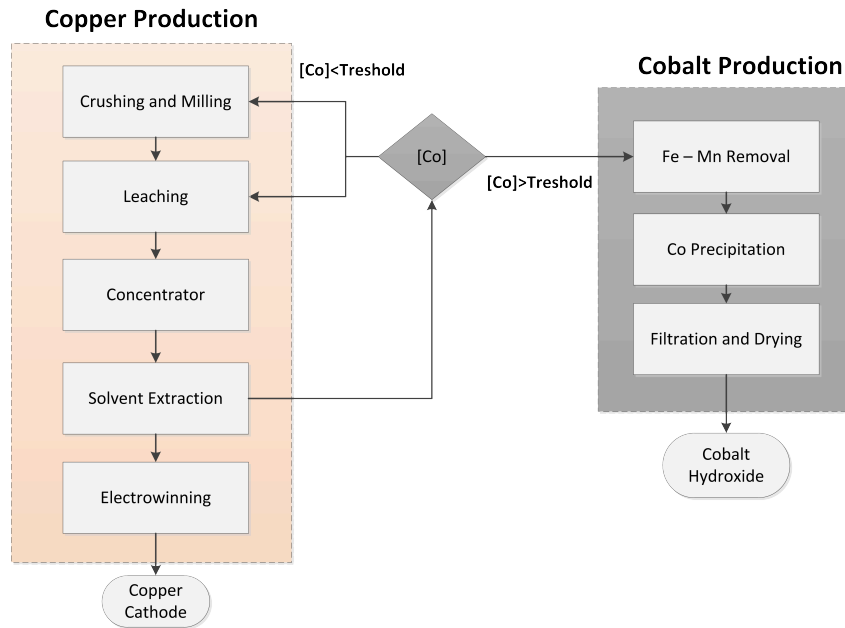
Figure 3.6: Schematic View of Processing and Metallurgical Operations at Mutanda Mining

3.3. Future Prospects

The future of the operation is extraction of the sulphide zone, as other companies have obtained licenses to explore the area outside of the current lease. This implies that Mutanda Mining will have to focus on extracting the copper and cobalt out of the current deposit. These sulphide minerals are found deeper in the deposit, are more expensive to mine and have higher processing costs. A study has been done confirming that the East pit will transfer into an underground mine when the sulphide minerals are going to be extracted.

Extraction of cobalt from sulphide ore is a different process than extracting the metal from the weathered zone. The plan is to construct a new plant for processing of the sulphide ore, using flotation to produce concentrate. The future plant is designed such that only copper will be produced. In the current project the calculated Net Present Value is purely based on copper production and no cobalt revenue is included (Tijsseling [95]).

3.4. Supplied Ore Samples

The mining operation has provided 35 different drill core pieces from 18 different drill holes and has classified these only as weathered or sulphide type. The samples are one quarter of the original drill core. No mixed zone ore has been provided, at least not with that description. An overview of the different samples is shown in Table 3.4. In this thesis samples will be referred to as B-*number*, W-*Number* or S-*Number*. The following definitions are used:

- B-*number*: complete piece of drill core, as provided by Mutanda Mining. The pieces of core have been sent in bags instead of boxes, thus no information can be derived about geological features, such as faults.

- W-*number*: piece of a drill core and classified as a *Weathered* sample. The W samples are part of a B sample.

- S-*number*: piece of a drill core and classified as a *Sulphide* sample. The S samples are part of a B sample.

- B-*number* will contain samples with either a W-*number* or a S-*number*, but not both.

As the sulphide ore is the future of the deposit, those will be the main point of focus in the characterisation and comminution stages. Weathered samples will be characterised, but shall not be considered for comminution.

Table 3.4: Depth and Classification of Samples as Supplied by Mutanda Mining

Drillhole ID	Sample ID	Depth From	Depth To	Length	Class
DD_01	B1	68.7	69.7	1	WEA
	B2	70.7	71.7	1	WEA
	B3	71.7	72.7	1	WEA
	B4	84.39	85	0.6	WEA
DD_02	B5	67.8	69.7	1.9	WEA
	B6	77.2	80	2.8	WEA
DD_03	B7	38.2	39.2	1	WEA
	B8	38.7	41.2	1.5	WEA
DD_04	B9	27.7	32.5	4.8	WEA
	B10	9.6	12.3	2.7	WEA
DD_05	B11	257	26	3	SUL
	B12	55.6	56.4	0.8	WEA
DD_06	B13	62.4	63.4	1	WEA
	B14	71.8	72.3	0.5	WEA
	B15	91.0	92.8	1.8	WEA
	B16	92.6	101	8.4	WEA
DD_07	B17	488.1	489.1	1	SUL
	B18	501.1	502.1	1	SUL
DD_08	B19	213.3	214.3	1	SUL
	B35	216	217	1	SUL
DD_09	B20	2	3.5	1.5	WEA
	B21	14.5	15.5	1	WEA
DD_10	B22	314.5	315.5	1	SUL
DD_11	B23	426.5	428.5	2	SUL
	B24	440.5	441.5	1	SUL
DD_12	B25	410.6	411.6	1	SUL
DD_13	B26	426.2	427.2	1	SUL
DD_14	B27	483	484	1	SUL
	B28	523	524	1	SUL
DD_15	B29	439.8	440.8	1	SUL
DD_16	B30	583.2	584.2	1	SUL
	B31	721	722	1	SUL
DD_17	B32	497	499	2	SUL
	B33	500	502	2	SUL
DD_18	B34	340	344	4	SUL

4

Literature Review

This chapter will describe the principles behind the different characterisation, comminution and simulations techniques used. Also, the potential issues or shortcomings will be highlighted and some recent applications will be discussed per technique.

4.1. Portable X-Ray Fluorescence

Portable X-Ray Fluorescence (pXRF) is a method that can be used to determine the chemical constituents of rocks and sediments. In general, this method is used as a semi quantitative tool that allows fast acquisition of consistency or variations within a dataset, but always should be combined with other independently acquired data. Quantitative calibration has been considered an issue for XRF core scanners and portable devices, which has been studied on numerous occasions (Bloemsma [10]).

When a sample is irradiated or excited with X-rays, an inner energy shell electron can be ejected if subjected to the appropriate absorption frequency. This causes the atom to be unstable and will lead to an electron from a higher energy shell to drop down and fill the created void in the inner cell. The excess energy associated with this transition is released using an X-ray photon (fluorescence), with the wavelength of that photon being dependent on the type of atom (Hou et al. [41]). This means that X-ray excitation can be used for chemical analysis of the material in question. The measurement is dependent on inner shell electrons, meaning that valence shell electrons are not considered (Hou et al. [41]). This means that the molecular state of the atom is not considered, making XRF a useful semi quantitative or qualitative tool, but not quantitative. Quantitative measurements will be matrix dependent, as different samples may allow for a different penetration depth of the excitation photons (Bloemsma [10]).

Modern XRF spectrometers are moderately sensitive, as the limits of detection are as low as Parts Per Million (PPM), both for lab based and portable XRF systems ([42]). Portable XRF analysers have the advantage of being able to analyse in-situ samples and having a high sample throughput, but a major disadvantage is the uncertainty associated with the devices. This has been investigated in several studies over the past years. An example is the inter-device variability, studied by Brand and Brand [13]. Six different 'off the shelf' Delta Premium devices were tested to quantify the chemical composition of a sample, with the measured Fe values differing from -19.56% to -13.02%. Tests were done for a range of elements and concentrates and eventually it was concluded that this low accuracy is a function of the instrument and manufacturer calibration. However, the precision of the measurements was reported to be excellent for Fe, but varying for elements such as Ca and Zr.

A similar study was done by Hall et al. [36], focussing on the application of portable XRFs in exploration and mining. Three handheld and two portable bench top XRF devices were used to analyse controlled reference materials. Again, the performance both across the instruments and elements varied. Major elements were well detected, but the sensitivity was reported to be too low for proper detection of Cl and P. Relevant for this thesis is that Co was studied as well. Hall et al. [36] stated that due to the position of Co in the Periodic Table (right of Fe), considerable interference with Fe is taking place. Below levels of 20 PPM Co, measurement precision is considered to be poor. This means that the detection limit associated with cobalt is in reality

higher than the theoretical limit given by the manufacturer.

Ross et al. [84] evaluated the performance of three pXRF devices on unaltered and unprepared drill cores, which is related to the samples used in this thesis. It was stated that the application is very useful, but that understanding the limitations of the data is essential. The volume of the rock is very small, meaning that the measured concentrations will be influenced by the mineralogical heterogeneity, especially for coarse grained samples. It is stated that the effect of mineralogical heterogeneity is a cause for data scatter, rather than the precision of the instrument. The lack of measurement accuracy and consistency between models still needs to be taken into account, but can be overcome by using empirical correlation factors.

Fisher et al. [28] developed calibration and workflow procedures, in order to allow for industry standardisation of geochemical data obtained using a pXRF. Parameters considered are sample preparation, selection of instrument, setting of beam count-times, standardisation and accuracy, influence of matrix effects and archiving the data. It is stressed that is important to understand the limitations of the data. One of the key findings that is relevant for this thesis, is the positive review on applicability of portable XRF to measure cut drill core. It is advised that pulverised samples are preferred to increase overall precision.

Gazley and Fisher [29] discussed the limitations associated with pXRF data and proposed a method for reporting obtained data in JORC compliant documents. Three different types of analytical drift were identified and are important to consider when analysing data: a random step change due to sample change or calibration of the device, gradual drift due to warming up of the unit and random fluctuations in between correct readings. Furthermore, it is stated that when using pXRF data as leading in resource estimation, one needs to publish the mean value, standard deviation, drift associated with the device and homogeneity, to name a few.

4.2. QEMSCAN

Quantitative Evaluation of Minerals by Scanning Electron Microscopy (QEMSCAN) is a method has been developed by CSIRO in Australia for the mining industry to quantitatively analyse ore and to provide reliable mineralogical and mineral analyses (Gottlieb et al. [34]). It has been be considered as automated image analysis, but provides much more information, such as quantitative chemical, mineralogical and textural data, accompanied by compositional maps on micron-scale (Goodall et al. [33]).

A specimen is scanned using a narrow beam of electrons, that are used to excite a small area of the sample surface. This leads to three phenomena taking place: the reflection of high-energy electrons by elastic scattering, emission of secondary electrons by inelastic scattering and the emission of electromagnetic radiation in the form of X-ray photons. This energy is released when electrons fall from higher energy orbitals to fill up the gaps created by the ejection of excited electrons (Haberlah et al. [35]).

Two types of raw data are measured: X-ray detectors measure the photons released at each measurement point and plot energy dispersive X-ray (EDX) spectra and the back scattered electron (BSE) signals. Data is measured along a pre-defined grid across the surface of the sample, producing a raster map. The QEMSCAN workflow uses the BSE signal as a control for EDX spectra acquisition to differentiate between the sample and the material containing the sample (Haberlah et al. [35]).

The EDX spectra are used for elemental identification. Usually, the spectra of 1000 X-ray photons are measured (this is user defined) and compared with a built-in library of elemental spectra. The elemental composition is quantified by taking the matrix interferences into account, correcting for X-ray absorption, secondary fluorescence and elemental overlap (Haberlah et al. [35]). After the elemental composition is determined, this data is compared to an a-priori known database of minerals to determine the present minerals, this is known as the Species Identification Protocol (SIP). Specimens with similar spectra are identified using the BSE signals. If both the spectra and BSE are similar, the minerals are identified using elemental ratios (Gottlieb et al. [34]). This is the basis for an accurate and complete mineral identification process.

According to Gottlieb et al. [34] there are four different analytical methods that can be used:

1. Bulk Mineralogical Analysis (BMA) - a rapid line scan analysis used to identify the number and length of intercepts of different mineral species. This data can be used to determine mineral abundance, mineral surface areas, mineral associations and mineral grain and particle sizes.

2. Particle Mineralogical Analysis (PMA) - mainly used for detailed characterisation of particles, up to 1 *mm* in size. The data that can be obtained is more particle related, such as diameter, perimeter and whether it is in contact with other particles.

3. Specific Mineral Search (SMS) - this method operates in a similar way as PMA, except that images are taken of particles containing a specific BSE. A pre-defined maximum concentration is set as threshold, greatly reducing the number of measurements.

4. Trace Mineral Search (TMS) - works following the same method as SMS, but only when trace amounts of an element are present. This is accelerated using specialised hardware that continuously compares the measured BSE value with a threshold value and rejects it when it is non compliant (Butcher et al. [15]).

Analysis of the mineralogical sample depends on both chemical and spatial resolution. Chemical resolution is the ability to separate phases based on the chemical constitution. Andersen et al. [1] found out that there is a typical 3% lower limit of mineral detection for the intensity of individual X-ray energies. A factor of influence on this is the number of X-ray spectra that is counted, which is a trade off between the level of detail and time efficiency. Rollinson et al. [83] state that issues may arise when identifying between minerals that mainly differ in the concentration of light elements, such as elements that are not directly detected (H) or that have limited detection in the X-ray signals(C and O). A method to overcome this is by focussing on different concentrations of hydroxide (OH) and carbonate (CO_2).

Spatial resolution is the minimum distance above which two distinct phases can be separately recognised. Spatial resolution depends again on chemical resolution and the volume of the sample of which X-rays are generated. In general, the volume of which X-rays are generated is between 1 and 2 μm in diameter. According to Gottlieb et al. [34] particle sizes below 5 μm put a limitation on the spatial resolution. The described QEMSCAN method has been used to obtain quantitative mineralogical and chemical data for a range of commodities. Examples are gold (Goodall and Scales [32]), bauxite (Boni et al. [11]), nickel (Andersen et al. [1]) and zinc (Rollinson et al. [83], followed by Santoro et al. [88]).

Also iron ore was studied, by Anderson et al. [2], where QEMSCAN was used to obtain the modal mineralogy, mineral associations and liberation degree. Those outcomes were used to understand the impact of different ore mineralogy on the iron extraction process. This study is comparable to the approach used in the second part this thesis, as the samples were crushed and milled before QEMSCAN analysis. A major challenge in this study was the complex mineralogy, due to the presence of goethite, hematite and magnetite. That problem was tackled using the BSE signal. It was concluded that four different ore types are present, all with unique implications to be considered when designing a processing facility.

When it comes to processed minerals and concentrates, very useful observations can be made regarding the liberation degree of the samples. This was used by Pascoe et al. [77], studying the feed and products of a gravity concentrator processing chromite ore. Observations were that the QEMSCAN method allowed for accurate classification when differentiating between the particles, but that the particle size distribution is underestimated, compared to distribution found using a laser sizer. It is not mentioned whether exactly the same samples are studied by the two different techniques.

Benedictus et al. [6] also used the QEMSCAN for analysing processed concentrate, using a hydrosizer and flotation operation. In this study the main focus was identification of the impurities present on the refined phlogopite, but also the sizes of the impurities were assessed. The main focus is the difference between the results from analysing the hydrosizer and flotation concentrate, meaning that the quality of the QEMSCAN data is not evaluated or questioned.

Conclusively QEMSCAN is a very useful quantitative method which can be used to obtain the modal mineralogy, the mineral associations, grain size distributions, liberation degree and visualise the mineralogy (using false colours),

4.3. Surface Hardness

Surface hardness is a parameter that has the potential to be used to predict response of the ore to comminution processes, such as crushing and grinding. There are several non-destructive methods that can be used to get an indication of the rock strength. One method is to assume that the rebound height of a ball onto a rock surface is related to the mechanical strength of that rock. Using that principle, the Equotip hardness tester has been developed (Proceq [80]).

The Equotip is a spring loaded, electronically driven device, shown in Figure 4.1. A tungsten carbide ball (diameter = 3 *mm*) is released from a spring-driven piston and plunges towards the surface of interest, rebounding against the sample.
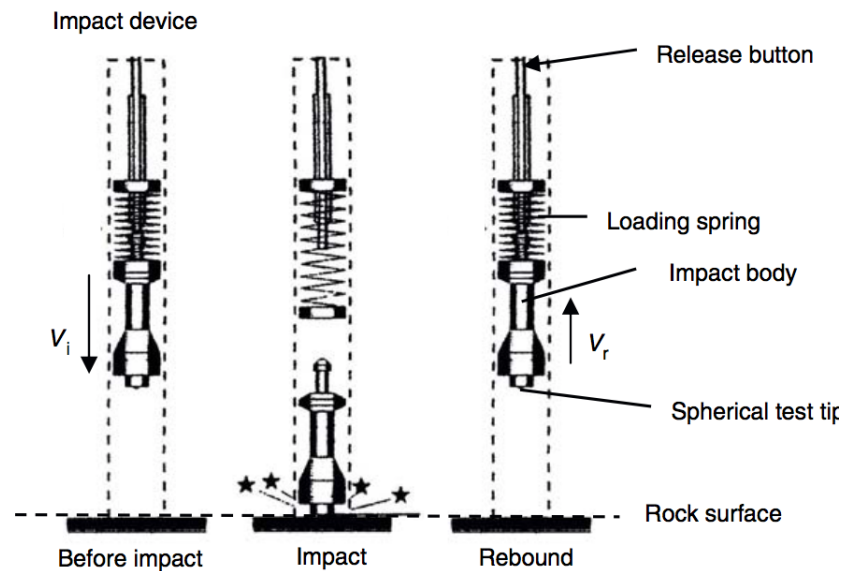
Figure 4.1: Schematic View of the Equotip (Aoki and Matsukura [3])

Inside the impacting body a permanent magnet is placed. The body passes through a coil before and after the impact, and a current is induced due to the interaction of the moving magnetic field and the coil. The relationship of the induced current to the impact and rebound velocity is proportional. The ratio of the velocities is multiplied with a 1000 to obtain the Leeb Hardness value (*LH*) (Proceq [80]):

$$LH = \frac{v_r}{v_i} \cdot 1000 \tag{4.1}$$

v_r is the rebound velocity and v_i the impact velocity of the impacting device.

Initially the Equotip was designed and used to determine and compare the surface hardness of metals (Proceq [80]), but the equipment has been used in geotechnical and rock mechanical studies since the early 1990s. Verwaal and Mulder [97] studied the possibility to predict Unconfined Compressive Strength (UCS) from the Equotip rebound values, no direct conclusions could be drawn. Aoki and Matsukura [3] were the last study that focussed on finding a relationship between the Leeb Hardness value and UCS. A large range of rocks and minerals were studied, leading to an empirical relationship that is porosity and Leeb Hardness dependent. More recently, the Equotip was used to determine variability in the hardness of weathered materials by Coombes et al. [22]. The conclusion was that the Equotip is sensitive enough to detect subtle changes in hardness induced by chemical and biological weathering.

A study was done focussing on the influence of measurement conditions on the Equotip rebound values by Okawa et al. [75] and led to the following observations:

1. Roughness and curvature of the surface of interest has no clear influence on the rebound value.

2. That same rebound value depends partially on the way the test specimen is supported.

3. Continuous impact by hitting on the same point leads to an increase in the rebound value.

The instruction manual for the Equotip (Proceq [80]) comes with a clear methodology that needs to be followed in order to determine the sample hardness. This includes placing the Equotip perpendicular onto the test surface and the need of coupled support for small samples. According to Aoki and Matsukura [3] there are two main methods to measure the hardness of a sample.

- Single Impacts Method - a single impact is applied onto a certain limited area at ten different points of the rock surface. After this the determined *LH*- value is averaged out.

- Repeated Impacts Method - the data is collected from a specific point by applying twenty impacts consecutively on the same point. Both the average value and the variation in *LH*- value is recorded.

Keeney [45] performed an extensive study in using the Equotip for domaining drill core based on surface hardness. An important statement is that even though the device is simple to use, the measurement depends on a number of complex factors: grain size, immediate grain support and mineral hardness at the point of impact.

The majority of the work performed by Keeney [45] focussed on understanding the impact of sample spacing, sample size and filtering of the data. Using a standard error diagram, the minimum sample spacing was set at about 2.5 *cm*. An extensive study was done on the sample sizes. A relationship was established that allows to relate readings performed using different drill core sizes and sample lengths. Through e-mail contact Keeney explained that the main factor influencing the measured value is the sample mass. Data filtering included removing the largest outliers, both above and below average. Keeney [45] recommends keeping all the data that falls within 95%. Misfires may lead to extremely low readings, which are removed using this approach.

Parbhakar-Fox et al. [76] used the data gathered by Keeney [45] to identify zones of most likely weathering and associated acid formation. This was done by logging the lithology conditions versus the measured surface hardness and assuming that zones of lower hardness are more likely to weather more severely. No clear conclusions are drawn about the applicability of the Equotip by Parbhakar-Fox et al. [76].

Based on the contact with Keeney, the first goal will be to determine a minimum sample mass required for correct Equotip readings. Using the Second and Third Law of Newton the influence of mass can be assessed:

$$\vec{F}_1 = -\vec{F}_2 \tag{4.2}$$

Stating that $\vec{F}_1$ (Force 1), the impacting force, will get countered by $\vec{F}_2$ (Force 2), with an equal but opposite value. It is known that a force can be defined as:

$$\vec{F} = m\frac{d\vec{v}}{dt} \tag{4.3}$$

With m being mass and $\frac{d\vec{v}}{dt}$ the change of velocity with respect to time. Inserting this gives:

$$m_1\frac{d\vec{v}_1}{dt} = -m_2\frac{d\vec{v}_2}{dt} \tag{4.4}$$

Where m_1 is the mass of the impacting body and m_2 the mass of the stationary body, with v_1 and v_2 the associated velocities. But if $m_1 << m_2$, than $\frac{d\vec{v}_2}{dt} = 0$ and thus:

$$\frac{d\vec{v}_1}{dt} = -\frac{d\vec{v}_1}{dt} \tag{4.5}$$

This means that there must be a minimum mass that is required for $m_1 << m_2$ to be valid. If that condition is not fulfilled the measured rebound velocity is not an accurate description of the surface hardness. Finding this limit on the Equotip will be the first step.

4.4. Mid InfraRed Spectroscopy

Using InfraRed (IR) spectroscopy, intense fundamental molecular vibration features can be detected in the wavelength range 2500 to 25000 nm (Rossel et al. [85]). The wavelength range from 2500 to 25000 nm is known as the Mid IR (MIR) range.

One method to detect these features is by measuring the reflectance of IR light onto a medium of interest. Depending on the material, certain frequencies are refracted into the medium and some are reflected (Clark [20]). The exact details are beyond the scope of this thesis, but a high reflectance is induced by a combination of an extinction coefficient (K) and index of refraction (n). The points of maximum reflectance are known as the reststrahlen band, indicating the location of fundamental vibration and stretching modes. Within those regions specific minerals will appear to have metallic properties when exposed to electromagnetic radiation of the IR signal, meaning that a high reflectance can be measured (Thomson and Salisbury [94]).

Povnnennykh [79] discussed the main factors influencing the position of absorption bands in the IR spectra of minerals and state that the main factor of influence is the relative strength of chemical bonds between adjacent atoms. This bond strength depends on the number of valency cations, which directly influences the frequency of vibration. The higher the number of valency cations, the higher the frequency of the absorption band. It is recommended to visually compare experimental IR curves to standard IR spectra of minerals.

The location of mineral spectral features in the MIR region is discussed by Salisbury et al. [86]. The most intense fundamental features are due to fundamental stretching and bending vibrational motions of the component atoms. For silicates, the Si-O stretching region is found at 8500 and 12000 nm. This primarily involves displacement of the oxygen atoms. Silicate combinations with metal cations may contribute to additional or different stretching and bending modes.

Carbonate ions have main features of C-O stretching at 7000 nm and weaker features at 11400 and 14300 nm due to bending modes. Other common fundamental features are due to water and hydroxyl (OH). If water is not fixed in the lattice, but is hydrogen-bonded to other water molecules features can be found around 2900 nm (O-H stretching and vibrations) and 6100 nm (H-O-H bending vibrations). Minerals containing hydroxyl without water mainly show O-H stretching features around 2800 nm (Salisbury et al. [86]).

When measuring the reflectance of several minerals at the same time, mixed spectral features can be found. Thomson and Salisbury [94] studied mixed spectra between 7000 and 14000 nm, determining whether mixed spectra of different minerals can be added linearly. It was observed that there is correspondence between the calculated and measured spectra, but in the area of strong reststrahlen bands (8000 - 12000 nm) discrepancies are found as non-calculated peaks or troughs appeared in the measured spectra. It is concluded that for mineral mixes containing smaller particle sizes, non-linear mixing effects occur.

Ramsey and Christensen [81] went beyond linear addition of spectra and used a spectral deconvolution algorithm. An important aspect studied is the mineral grain size limit from which linear mixing can be assumed. For mineral mixtures with grain sizes over 60 μm the spectral mixing is considered to be linear. Between 60 and 20 μm the linearity continues and for grain sizes below 20 μm non-linear mixing effects are observed.

The IR measured signal has also shown to provide information about the crystallinity of the minerals. Examples are studies by Hewson and Cudahy [40] and Plyusnina [78]. That type of detail is beyond the scope of this study.

In this thesis, Fourier Transform InfraRed Spectroscopy (FTIR) is used for the analysis of the MIR range. FTIR depends on certain mathematical manipulations, including using a Fourier transformation (Herres and Gronholz [39]). FTIR measurements use the interferometer concept to determine what wavelengths are absorbed by the studied medium. IR emitted light is split using a beam splitter, after which half the signal reflects and the other half passes through and leaves the interferometer. Using a moveable mirror within the interferometer it is ensured that both signals travel a different distance, leading to wave interference and causing maxima and minima. This mirror displacement is defined as x. A schematic overview of the whole process is shown in Figure 4.2.

After the signal that leaves the device has returned, a detector is used to measure the intensity of the combined beams as a function of the mirror displacement: $I(x)$. That function is defined as the interferogram. The interferogram is converted into a continuous waveform using a Fourier transformation, that is defined as the Sample spectrum. A second interferogram is created, without a sample in the optical path. This is defined as the Reference spectrum. By dividing the Sample spectrum by the Reference spectrum wavelengths

at which absorption has taken place can be identified (Herres and Gronholz [39]).
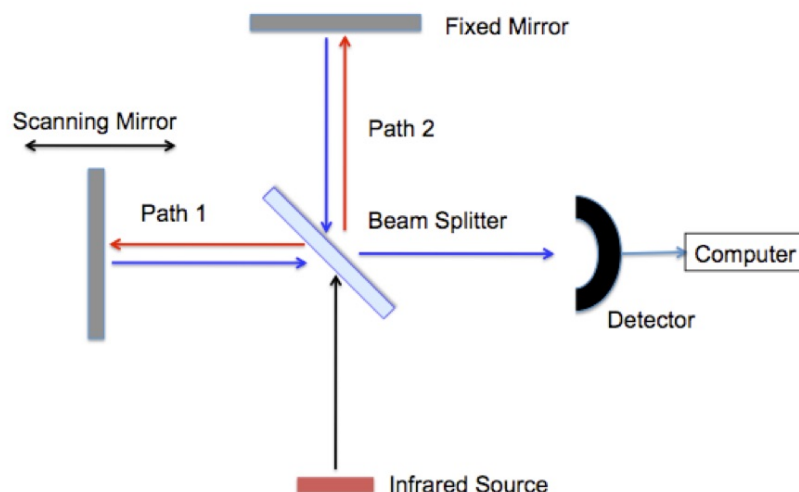
Figure 4.2: Schematic View of FTIR Data Acquisition (Stockwell [92])

Compared to regular IR spectroscopy, FTIR has the following advantages (Herres and Gronholz [39]):

- Connes advantage: the accuracy is determined by the laser wavelength, giving high precision in the wavenumber or wavelength calibration.

- Jacquinot advantage: the optical apertures used in FTIR often have a larger surface area, allowing for more radiation to pass through.

- Fellget advantage: instead of recording the intensity one after another, all frequencies are recorded immediately.

Ballard et al. [4] used FTIR to quantitatively describe the mineralogy of reservoir rocks and were able to detect mineral concentrations with an error 1.1 wt% and a standard deviation of 2.1 wt%. The information of the spectrum was quantified using an inversion scheme. The minerals studied included quartz, dolomite and chlorite. Previous to Ballard et al. [4], quantitative mineralogical studies were done successfully by and Bertaux et al. [9] and Matteson and Herron [60].

The latter focussed on defining mineralogy by using the Beer's law, stating that absorbance bands of the components are proportional to the pure mineral spectrum:

$$A = \sum_{i=1}^{n} \epsilon_i \cdot l \cdot c_i \tag{4.6}$$

Where ϵ_i is the absorptivity of component i, l the absorption path length and c_i the concentration of component i. The absorptivity is a factor that will be kept in mind when attempting to interpret the mineral proportions.

MIR is often used in the remote sensing industry. An example is a study by studied Kruse [51], that use MIR to map the mineralogy of thermal hot springs. One of the observations was that zones containing quartz could clearly be identified. A topic in that study was to evaluate the accuracy of the sensor in both the NIR and MIR region. Kruse [51] concluded that sensor was accurate in both regions and could be used to determine the mineralogy of the thermal hot springs.

Notesco et al. [73] used the same technique to classify the surface of an open pit lignite mine. Again, zones containing quartz could be identified and this was also the case for kaolinite. The data was used to quantify the amount of quartz and kaolinite, as these affect properties that are needed to monitor the stability of the surface (Notesco et al. [73] used).

No studies could be found that have assessed drill core mineralogy using the MIR wavelength range or FTIR technique.

4.5. CT Scan

X-ray computed tomography, also known as CT (Mees et al. [63]), is a non-destructive technique that visualises the internal structure of objects based on the variations in density. X-ray radiographs are gathered from varying positions, following a step wise rotation around a central axis. This gives the possibility to make a three dimensional (3D) reconstruction of the object at the centre. The future potential of using CT instruments for scanning drill core at a moderate resolution is mentioned.

In 2013 Cnudde and Boone [21] reviewed the use of X-ray tomography in geosciences and discussed the applications. One of the first statements is that the use of CT scans is great for qualitative results, but that quantitative data requires specific software for a specific desired result. CT technology is at this moment mainly used for 3D pore characterisation, grain analysis, fracture analysis and ore analysis (Cnudde and Boone [21]).

A practical example of CT technology has been published by Ghorbani et al. [30]. The spatial distribution of cracks and mineral dissemination in sphalerite ores are studied using X-ray tomography. The results are compared with more traditional results, such as QEMSCAN and SEM technology and showed to be in good agreement. Cracks can be recognised with relative ease, but distinguishing between different minerals will require a calibration procedure. The higher the difference in density, the easier it is to distinguish.

Becker et al. [5] used CT scan image analysis as a geometallurgical indicator, providing on-site data about mineralogy and mineral texture. The main advantages are that the scanned drill core is conserved and that little to no sample preparation is required. Three texture types could be obtained from the scanned drill cores. It is concluded that the CT scan has the potential as a geometallurgical tool on site.

4.6. Laboratory Comminution

Size reduction of rocks is usually carried out in the processing plant. The size reduction makes up for approximately 5-15% of the mine-to-metal processing costs (Chaigneau [17]). Size reduction is usually done through crushing and grinding. The main reasons for crushing and grinding are:

- Liberation of a valuable component from the matrix.

- Promotion of a rapid chemical reaction by increasing the surface reaction.

- Production of a material with certain desired treatment and storage properties.

Liberation of the valuable component is the eventual goal in these comminution experiments. According to Chaigneau [17], within ore the grains of the valuable component are chemically bound to surrounding gangue material. Reduction of size aids to rupturing these bonds, through mechanically fracturing particles. The ore is broken into small enough fractions to liberate the valuable components from the gangue (Napier-Munn et al. [71]). It is tougher to liberate fine grained rocks than coarse grained rocks, due to the influence of grain boundaries on crack propagation. In reality, the preferred rupture along the mineral grain boundaries does not occur. This means that full liberation of the mineral is not possible and that the actual size of the liberated mineral is smaller than the original grain size (Chaigneau [17]).

After crushing and grinding mainly free gangue grains, some free valuable grains and mainly combined grains can be found. The larger the reduction in size is, the more the liberation of a mineral improves. The rate of improvement depends on mineral properties, volume concentration, mineral texture and shape. Measuring liberation of ore is often done using microscopy. Napier-Munn et al. [71] name QEMSCAN as an excellent method for this.

In the 1990s comminution was a popular topic in minerals engineering (King [47]). Predicting liberation from microscopical data was seen as one of the most important accomplishments (King [47]). This is done through the use of breakage functions and understanding of breakage mechanisms in a certain impact process. Breakage processes are understood through using laboratory tests, such as a dual pendulum or ultrafast load cell and this fracture data is used for liberation modelling of the mineral liberation. King [47] considers mineral liberation as an essential factor to be evaluated when studying comminution.

The SMC test developed by Morrell [67] allows for calculation of mill energy consumption with only a small amount of sample being available. Core diameters with a diameter in between 27-85 *mm* can be used and are crushed using a drop weight test. Two parameters are derived from the amount of sample that is

crushed per mass unit that is dropped onto the drill core samples. These parameters can again be linked to energy consumption, but not necessarily liberation of the ore.

The effect of different breakage mechanisms on mineral liberation of sulphide ore was studied by Vizcarra et al. [99]. This was done using two different types of ores, one being low grade iron-oxide hosted copper gold ore and the other from a high grade statiform zinc deposit. Two different non-conventional breaking mechanisms were used: a hammer mill and a piston-die compression unit. After comminution the concentrate was analysed using automated scanning electron microscopy. For both ores the size-by size liberation properties showed to be independent of the breaking mechanism. Also the gangue mineral breaking appeared to be identical when using different breaking mechanisms. Compared to the conventional comminution techniques, the hammer mill and piston die did not appear to enhance the liberation properties of metalliferous ores.

Process mineralogy and the associated impact on process performance was studied by Bradshaw [12], mainly focussing on complex sulphides. The most important processes considered are characterising the material and how to optimise size reduction and the associated liberation. Misinterpreting the mineral texture may lead to poor liberation and thus poor performance of the rest of the circuit. The optimal size will depend on the complete process, as both too fine and too coarse material can negatively affect the process. Automated mineralogy is stated to be an essential part in process mineralogy. Bradshaw [12] mention QEM-SCAN as a very useful tool in understanding the effect of mineral texture on liberation.

Singh and Venugopal [90] went a step further and also considered the morphology of ore on the breakage and liberation of minerals. Crystallography and the influence of mineral interfaces were analysed. Singh and Venugopal [90] claim that these mineral interfaces play a prominent role in the initiation of fractures and thus heavily influence the breakage and liberation properties. However, these are only a few factors that play a role. The presence of volatile materials and moisture also influence the breaking and liberation mechanisms. Overall, considering the crystallography of the minerals of interest and the mineral interfaces could be very promising, but is considered to be beyond the scope of this thesis.

In section 2.3 it was discussed how different comminution zones were established based on differences in the Bond Mill Index by Montoya et al. [65]. A Bond Mill Index experiment requires approximately 5 kilograms of material and within this thesis such quantities are not available. In this section the SMC test developed by Morrell [67] was mentioned. This method does not provide information about the ore liberation and thus is also not considered. The method developed by Mwanga [69], also discussed in section 2.3, is considered to be suitable for this thesis. A small volume of sample is required, ore liberation and comminution parameters can be obtained and most importantly: this method has been developed by focussing on assessing comminution in a geometallurgical context. The details associated with this method will be outlined in section 5.6.

Two types of comminution equipment will be used in the experiments, a jaw crusher and a ball mill. A schematic version of both is shown in Figure 4.3. On the left a jaw crusher is seen, that uses impact to crush samples between two moving plates. The right side shows a cataracting ball mill (a) and cascading ball mill (b). Cataracting uses the impact of the balls for grinding, whereas cascading using shear stresses. The latter is mainly used for ultra fine grinding (Chaigneau [17]).
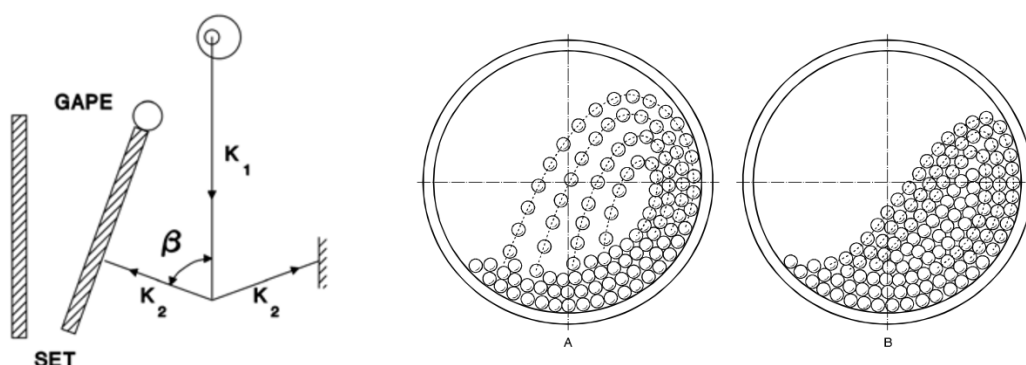
Figure 4.3: Jaw Crusher (left), Cascading Ball Mill (a) and Cataracting Ball Mill (b) (modified after Chaigneau [17])

4.7. Simulated Crushing

Simulation is an important part of modern minerals engineering, as it allows to evaluate the suitability of certain crushers and mills on industrial scale without requiring large investments or experiments. However, computational minerals engineering is a simplified version of what occurs when minerals are processed. This section focusses on the theories behind simulated mineral processing.

Simulation assumes a steady sate performance of a circuit in terms of stream properties and allows to evaluate the effect of changes on the performance without doing experimental work. The quality of the simulation results depend on the quality of the input data (Napier-Munn et al. [71]). In general, the comminution models can be divided into two types (King [48], Napier-Munn et al. [71]):

- Models that consider the comminution device as a transformation between feed and product size distribution (black box).

- Models that consider each element in the process (fundamental).

According to Napier-Munn et al. [71] the black box model mainly focusses on predicting product size distribution, based on the feed size distribution and by implementing breakage characterisation based on experience with similar devices. The black box approach considers the interaction of ore particles and elements within the machine, instead of understanding the fundamental principles. The population balance model is the most widely accepted black box model.

The fundamental model uses ore particles interaction, machine elements and Newtonian mechanics to calculate the product size distribution from the input. This type of model will require a thorough analysis of the whole process and significant computational power. Working with fundamental models is considered to be outside of this thesis scope, meaning that the black box model will be the main focus point in comminution simulation.

According to Napier-Munn et al. [71] the black box model can be described as:

$$p = F(f, b, m, s, C) \tag{4.7}$$

Where:

p and f = product and feed size distribution

   b = a normalised breakage matrix or vector

  m = key mill factors

   s = operation conditions, including mill feed rate

  C = set of parameters derived empirically from this or similar devices.

The population balance model was introduced by Epstein (1947) and assumes that the production of ground material per unit time depends only on the mass of that size fraction which is present in the mill. The rate of breakage is found by multiplying a constant breakage rate with the mass of that size fraction in the process. This assumption is not valid when there are too many or few particles are available (Napier-Munn et al. [71]).

The mass balance describing this process is defined as:

$$Feed\,in + Breakage\,in = Product\,out + Breakage\,out \tag{4.8}$$

By including a breakage function that describes the full range of input sizes, the following balance can be defined:

$$f_i + \sum_{j=1}^{i-1} b_{ij} k_j s_j = p_i + k_i s_i \tag{4.9}$$

Where f_i is the feed function, b_{ij} is the breakage function, k_{ij} the breakage rates, s_i the mass of the ith size fraction and p_i the product function. This is usually re-arranged in terms of the product function:

$$p_i = f_i - k_i s_i + \sum_{j=1}^{i-1} b_{ij} k_j s_j \tag{4.10}$$

And modified to include the solids residence time:

$$p_i = f_i - k_i s_i + \lambda \sum_{j=1}^{i-1} b_{ij} k_j s_j \tag{4.11}$$

Where λ is the mean solids residence time.

Discrete modelling functions are often replaced using continuous integrals. King [48] describes a general population balance equation for comminution machines, including particle size, coordinates and wear of the machinery. More detailed integrals on this approach can be found in the associated literature.

The published works on crushing simulation usually involve dynamic models. An example of such a model has been developed by Itävuo et al. [43], emphasising on the effect of fluctuating ore on the performance of the comminution circuit. It is stated that there is a large gap between reality and simulation, as simulation does not take account for the ore variability that occurs in reality. This can again be linked to geometallurgy, and that is the goal of these simulations: study the effect of ore changes on the simulation results.

Koch and Rosenkranz [49] used mineral texture as the basis for modelling the liberation behaviour of the ore in a comminution process. This texture approach can be considered to be a fundamental model and is based on combining and improving previously defined models. In the near future Koch and Rosenkranz [49] will focus on validating the model and applying it to test cases.

5

Experimental and Analytical Set Up

The experimental or analytical set up for the different techniques discussed in Chapter 4 will be outlined in this chapter, following the same order.

5.1. Portable X-Ray Fluorescence

To get an idea about the chemical composition of the core samples, all the samples were analysed using pXRF. This provides an estimate of the chemical composition of the samples, but is also an indicator for the minerals present in the samples. All elements on the periodic table occurring before magnesium will be classified as Lighter Elements (Bloemsma [10]). This means that oxygen, carbon and hydrogen, (three main components of the minerals present in the Mutanda deposit), cannot be quantitatively studied.

The pXRF device used in this study is the *Delta Premium (Olympus UK) Handheld XRF Analyser.* No minimum sample mass or size was required for a piece of ore to be analysed. Fragments of drill core or dust were not considered as samples.

1. The portable XRF was set in Geochemistry Mode.

2. The device was calibrated using a calibration sample containing SiO_2.

3. The XRF scanner was set to measure for 45 seconds per beam. The first beam measures the heavier atoms, the second beam measures the lighter atoms. This measurement time was set based on advice of experienced operators in the laboratory.

4. The flattest, most continuous and homogeneous side of the drill core sample in question was positioned on top of the XRF scanner.

5. The chemical assay of the sample was measured.

6. Based on the length of the drill core (>8 *cm*) or recorded values (Co >10%) a repeating measurement was done on the same sample.

7. The sample was removed and the pXRF scanner was cleaned to minimise the chance of false chemical components being detected. Following that the next sample was placed.

8. The gathered data for all measured elements is exported in a spreadsheet.

It is known that redoing a measurement on samples improves the overall accuracy, but this was not doable due to time constraints and a large number of samples being available.

It is possible that for the ore samples the elemental grade was below the limit of detection of the pXRF device. The detection limits supplied were manually inserted (Innov-X [42]). This was done by replacing the *<LOD]* value in the exported data with a minimum level of detection, that varies per element. The reason for

this, is the assumption that for previously measured elements at all times a residue value of the element will be present in the deposit. The inserted values per element are given in Table 5.1.

Table 5.1: Overview of the Eight Elements with Values Inserted at <LOD] Measurements (Innov-X [42])

Element	Co	S	Ca	Al	P	K	Ni	Mn	Zn	Ti	V
Replaced Value	0.002	0.006	0.004	0.1	0.008	0.005	0.001	0.001	0.001	0.0015	0.0015

5.2. QEMSCAN

The quantitative mineralogical analysis was carried out using a QEMSCAN® 4300 at Camborne School of Mines, University of Exeter. This set up contains the Zeiss EVO 50 Scanning Electron Microscope (SEM) platform and four light element Bruker silicon drift droplet (SDD) X-ray detectors. The EDX spectrum was acquired and combined with computer-based spectral classification allowed for rapid determination of the spatial distribution of the minerals present.

The selected samples were turned into thin sections with a volume of 100 μm (thickness) x 25 mm (width) x 40 mm (height). Pictures of the sulphide thin sections can be found in Appendix A. The field scan mode was used to determine the mineral abundance of these samples, using 1000 X-ray counts per spectrum. The field scan mode is a combination of the BMA and PMA mode. Per sample approximately 6 million data points were collected at a resolution of 10 μm. The points were identified using the obtained X-ray signals and by following a customised SIP.

Carrollite was not part of a previously developed SIP and thus needed to be set included. This was done by analysing the EDX and BSE spectrum of the sample that contained the highest amount of both cobalt and sulphur, found during the pXRF measurements. This data was used as a reference values for future identification of carrollite in the other selected samples. Analysing the samples and customisation of the SIP were done by an experienced QEMSCAN operator.

5.3. Surface Hardness

The Equotip used is the *Equotip Leeb 550D*. There are several rules that were followed both during the calibration of the machine and whilst estimating the surface hardness of the samples. These rules are based on the experience of Keeney [45] and Aoki and Matsukura [3]:

1. Twenty measurements on the test block were done before starting measurements on samples, allowing to identify whether the Equotip accuracy had started to drift.

2. The single impact method was used at each measurement, as the variation of the surface hardness was of interest.

3. A maximum sample spacing of of 2.5 cm was used, as this spacing has the best trade off between accuracy and data gathering (Keeney [45]).

4. All data outside two standard deviations was removed, to account for mishits.

Calibration   The first step was to understand the impact of sample mass on the Leeb Hardness value. Proceq [80] states that a sample requires a mass of over 2 kg. In total eight different blocks of limestone were used with varying mass. Limestone was considered to be appropriate due to the homogeneity of the blocks. To determine the influence of sample mass on the Leeb Hardness value the subsequent protocol was followed:

1. Eight different masses were studied, varying from 25 to 520 grams and all equal block height (25 mm)

2. Both the sample and the Equotip were hold firmly during the moment of measurement.

3. Twenty measurements were done per block of limestone.

Sample Surface Hardness   The surface hardness of the quarter core pieces was measured following a similar procedure. A schematic view of the experimental set up is shown in Figure 5.1. The surface hardness of all core pieces was measured using the following protocol:

1. The Equotip was placed on the sample and hold firmly.

2. A measurement was made.

3. The Equotip was moved to a new position following a straight line for the subsequent measurements.

4. Following the straight line, the number of measurements was maximised, depending on the sample size and condition.

5. Measurements were only performed on the side of the sample for which the diameter was the largest.
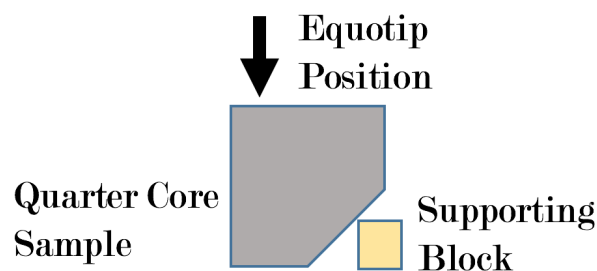
Figure 5.1: Schematic View of Quarter Core Surface Hardness Measurement Set Up

Mineral Texture   The ore samples that were not used in QEMSCAN section preparation are used to study the influence of mineral texture on the surface hardness. The samples are mirrored rectangles of the QEMSCAN sections with a maximum area of 46 by 25 *mm*. It is not possible to state at what exact position a measurement was taken. This is due to the surrounding base of the Equotip. For each sample four positions along the x-axis were chosen and the subsequent protocol was followed:

1. The Equotip was placed on the sample and hold firmly.

2. A measurement was made.

3. The Equotip was moved to a new position following a straight line for the subsequent measurements.

4. Following the straight line, the number of measurements was maximised, depending on the sample size and condition.

5. If the maximum height was reached, the Equotip was placed on the next horizontal position.

After performing a set of measurements, the data was exported using the *Equotip Link* software provided by Proceq.

5.4. Mid InfraRed Spectroscopy

The device used for MIR spectroscopy was the *Agilent FTIR 4300*, using Fourier Transformed InfraRed spectroscopy. This tool allowed to perform a point specific measurement and automatically processes the measured data into a reflectance spectrum. The measured wavelength ranges from 2500 to 15500 *nm*. The samples that were analysed using QEMSCAN were also analysed using FTIR, as those samples had the advantage that the mineralogy is known.

1. The FTIR 4300 was calibrated using a silver/gold standard.

2. The background noise was measured 126 times.

3. A sample was placed below the detector of the FTIR 4300 and contact was made between the device and the sample.

4. 64 measurements were taken by the FTIR 4300.

5. The reflectance was automatically calculated and averaged out.

6. The sample was repositioned so that another point measurement is performed on a different area, following a rectangular grid.

7. On each sample between 10 and 15 measurements were performed.

8. The data of interest could be exported as a .spc file.

The .spc file was imported into Origin 9. No additional noise filtering of the signal was done. For each measurement a plot was made which was visually compared to reference spectra of known minerals (Clark et al. [19]). Based on the spectra, a division was made between pure spectra and mixed spectra. For these spectra the position and cause of the features were analysed.

To analyse mixed spectra, a linear combination of the reference spectra was made. This was done by digitising the relevant spectra from Clark et al. [19] between 2500 and 16000 *nm*. That data is loaded into Origin 9, where the software was used to extrapolate the reflectance data for a 1000 points between 2600 and 15500 *nm*. The extrapolated data was linearly added for the relevant mineral combinations in order to get an indication of what mixed spectra could be expected.

For each sample between 10 and 15 points were gathered with mineralogical information, such a point is defined as a pixel. The identified minerals per pixel were used to quantify the mineralogy. In section 4.4 the factors influencing reflectance and absorbance were discussed. The main factor for a correct quantitative mineralogy would be the absorptivity of a mineral. That data is not available for this thesis. In order to quantify the mineralogy, a mineral was given a count when it could be identified in a measured spectrum. By dividing the number of mineral counts by the number of pixels the mineralogy was made quantitative.

5.5. CT Scan

The scanner used was the *Phoenix Nanotom m-microCT & nanoCT Computed Tomography System.* A constant set of scan parameters was used for all three samples.

1. The sample was placed in the scanner.

2. A test was done to determine the energy required by the X-rays to pass through the sample.

3. The analysis was started.

4. A density frame was automatically constructed based on the residue energy of the X-rays passing through the sample.

5. Three density frames were made, which were automatically averaged out to create one density frame.

6. Automatic reconstruction of the sample was made using the provided software (VG Studio Max 2.2).

In this thesis the CT Scan was used to obtain a 3D visualisation of three samples that appeared visually very different. These samples were also studied using QEMSCAN (S-314, S-345 and S-426). The main goal was to visualise the propagation of the valuable minerals in 3D using density differences, not to gather quantitative data about the mineralogy. These experiments were carried out in collaboration with experienced operators of the Delft University of Technology.

5.6. Laboratory Comminution

The comminution experiment was a modified version of the Geometallurgical Comminution Test (GCT) developed by Mwanga et al. [70]. The goal was to assess differences in crush-ability and grind-ability of the different mineral textures. A schematic work flow of the experiment is shown in Figure 5.2. The main differences with the experiment performed by Mwanga et al. [70] are that no indication of the energy consumption was found and that a different mill was used. The comminution experiment is carried out as follows:

- The selected drill core samples were crushed using a jaw crusher (1).

- The jaw crusher output was sieved using a 3.35 *mm* sieve, oversize was fed back into the jaw crusher (1).

- When the whole sample had a size of ≤3.35 *mm*, a riffler was used to split the sample in half (2).

- For half the sample, the PSD and chemical assay per size fraction of the crusher product were analysed (3a).

- The other half of the sample was fed into a ball mill, for a total grinding time of 21 minutes with an evaluation of the grind-ability every 3 minutes (3b).

- The mill output was split in half using a riffler (4).

- The semi quantitative XRF analysis was not part of this thesis, but part of the future verification (5a).

- After 21 minutes of total milling, the final PSD and chemical assay per size fraction were analysed (5b).
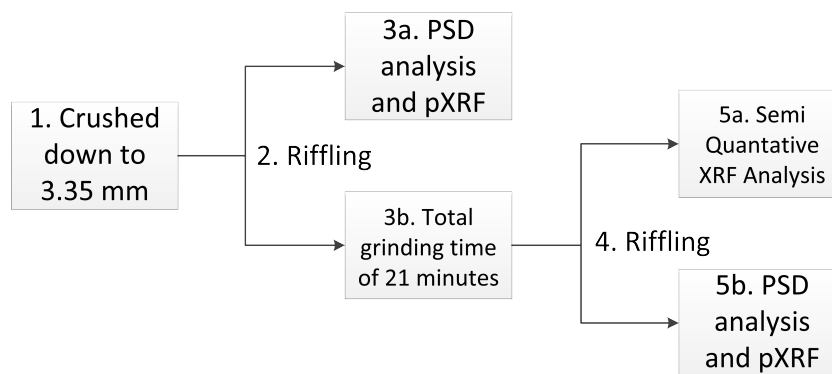
Figure 5.2: Schematic View of the Different Steps in the Comminution Experiments

In this experiment, also a jaw crusher was used for reducing the size of the drill core. The jaw crusher is shown in Figure 5.3. The jaw gap was set at the minimum size, in order to gain maximum size reduction in one crushing step. When changing the samples, the crusher was thoroughly cleaned using a vacuum cleaner and methanol.

Figure 5.3: The Jaw Crusher Used in the Experiments

The mill used is shown in Figure 5.4. A ball mill is set up by filling a metal jar with a ball load. There are three differences between the set up used in the GCT and this milling process:

- The jar was 155 *mm* in diameter instead of the 115 *mm* used in the GCT.

- The mill RPM was set at 94 instead of 114 RPM used in the GCT.

- The total milling time was 21 minutes instead of 25 minutes milling as used in the GCT.

The ball load was the same: 1.7 *kg*. Every time a new sample was milled, the used equipment was thoroughly cleaned using a vacuum cleaner and methanol.

Figure 5.4: The Balls (left) and the Mill (right) Used in the Experiments

The outcome should give an indication of the differences in comminution properties of the samples. That will aid in determining whether geometallurgical comminution classes can be set up based on the behaviour in a comminution process.

5.7. Simulated Crushing

5.7.1. Software Selection

The initial goal was to developed a lab scale simulation of the whole comminution process and compare the outcome with the results from the comminution experiments. Following that, different types of equipment could be tested and thus an ideal comminution process could be developed, which would be scaled up to industrial size. However, HSC Chemistry appeared to have some issues with that. In HSC Chemistry both crushers and grinders are modelled using the Rosin-Rammler parameters of the output of the unit process. Rosin-Rammler parameters define the PSD. In general, computational programs use calculated percentages in discrete size intervals to approach these parameters (Napier-Munn et al. [71]). The function is defined as:

$$F(d_p) = 1 - e^{-(\frac{d_p}{d_{63.2}})^n} \tag{5.1}$$

With d_p being the particle diameter variable, $d_{63.2}$ a constant that defines the mass percentage having a size inferior to 63.2% of the particle size and n a numerical constant. This means that if for different crushers or grinders the same Rosin-Rammler parameters are set, the particle size distribution of the output will be identical. HSC Chemistry could not be used to study the impact of different equipment on the comminution process.

Metso Bruno is a different simulation package, that specialises in equipment selection by simulated crushing and screening. The downsides of this software package are that the grinding process cannot be simulated and that the equipment in the software cannot be used for lab scale simulations. Bruno was used to determine the impact of different crushers on the crushing process, to evaluate what set up was beneficial from an energy perspective and to determine the energy requirements for the three geometallurgical zones.

According to Viilo [98] the Bruno simulation depends mainly on extensive field test data. The parameters of influence are the feed characteristics (rate, density, size distribution) and crusher characteristics (gap width, cavity, engine power). It is not stated by Viilo [98], but it appears Bruno uses a black box approach for simulation, assuming population balance modelling. The results allow to determine whether a designed process meets the required results.

5.7.2. Simulation Settings

The goal of these simulations was to determine the crusher type that is most suitable for the crushing process and to get an indication of the differences in energy requirements for different feed streams. To determine the impact of the different crushers, the subsequent work flow was followed using an identical feed stream that was pre-defined by Bruno:

- The feed stream was connected to a crusher and sieve. That sieve was connected to an oversize and undersize product pile.

- The crusher settings were set to the minimum allowed settings, such as gap width and engine power.

- Based on the amount of oversize an additional crusher and sieve were added, until the result was satisfactory (>95% undersize) or until a maximum of five crushers was reached.

- This process was repeated until all different crusher types within Bruno were evaluated.

After the impact of the different crushers was quantified and an optimal crushing tool had been selected, the energy consumption required by the different ore classes was evaluated by defining different input streams. Bruno required the following parameters:

- Density of the material

- Crush-ability of the material

- Abrasiveness of the material

- Moisture present

- Amount of gravel added.

The density was calculated by using the mineral volume given by the QEMSCAN and by multiplying that with the specific gravity of different mineral samples. The crush-ability and abrasiveness require an experimental procedure as set out by Metso (Viilo [98]), which unfortunately could not be carried out due to time constraints and lack of sample resources. Bruno contains the crush-ability and abrasiveness for quartz and dolomite. By multiplying the relative fraction of quartz and dolomite with the crush-ability and abrasiveness respectively, an indication of the crush-ability and abrasiveness was found.

6

Results and Discussion

6.1. Portable X-Ray Fluorescence

In total 483 XRF measurements were done on samples coming from 35 different drill core sample bags. The average chemical composition per bag is shown in Table 6.1. The samples are rich in copper and cobalt, with a large variation in the copper and cobalt grade. The highest average copper grade is 24.41%, with the minimum average copper grade being 0.07%. The standard deviation of the copper grade varies from 23.51 to 0.04. For cobalt, the maximum average grade is 3.98%, with the minimum being 0.00%. The variation in standard deviation of the cobalt grade is high as well, with a minimum of 0.00 and a maximum of 10.08. This indicates the presence of samples with extremely high cobalt content. The cobalt grade is high compared to the average grade of 0.5% that is found in literature (Crundwell et al. [23]). The contact on site also confirmed that the provided samples were selected on cobalt grade, suggesting that the measured cobalt grade in these samples is not representative for the deposit as a whole.

The presence of gangue elements varies as well, which is interesting from a geometallurgical perspective. Returning pollutants in high quantity are Ca, Si, Al, Mg, Fe, S and K. The proportions of these pollutants vary per sample. S is often present when high grades of Co and Cu are present as well. There are two samples that are classified as SUL, whilst the pXRF measurements indicate that no to very little S is present. These samples are B19 and B35 and will in the future be classified as weathered.

Even though that these results provide a lot of information about the samples, understanding the limitations of that information is essential. Previously the limitations of portable XRF data were discussed and the impact of analytical drift could be present here. No significant calibration was done and no reference samples with known composition were used. Calibration will one of the first steps that is required in the future work and can be done by plotting Co and Cu grade for measured pXRF versus measured quantitative laboratory XRF for identical samples.

Besides that, the area scanned by the portable XRF is 25 mm^2, whereas the samples that were measured are all much larger. The samples are clearly not homogeneous, as can be determined from the large variation in presence of cobalt, copper and other gangue elements. The penetration depth of the XRF beams are approximately 30 μm. The drill cores have a much larger diameter, meaning that large assumptions are made regarding the homogeneity of the sample geochemistry in all three dimensions. If samples are considered for future processing or for making assumptions, a more thorough geochemical analysis is required.

Table 6.1: Overview of the Average Chemical Assay and Standard Deviation per Sample

0.00 Sample	Class	Co (%)	σ	Cu (%)	σ	S (%)	σ	Si (%)	σ	Fe (%)	σ	Ca (%)	σ	Mg (%)	σ	Al (%)	σ	K (%)	σ
B1	WEA	1.70	0.15	1.40	0.12	0.04	0.01	1.21	0.14	13.05	1.51	0.44	0.02	1.46	0.28	1.03	0.11	0.11	0.01
B2	WEA	1.34	0.45	0.62	0.20	0.06	0.05	1.26	0.18	5.90	1.73	0.65	0.24	0.50	0.00	0.80	0.07	0.18	0.05
B3	WEA	1.43	0.57	0.85	0.31	0.03	0.02	1.18	0.28	7.65	2.03	0.33	0.03	0.64	0.25	0.95	0.21	0.14	0.03
B4	WEA	4.84	7.38	24.41	12.4	0.02	0.02	0.02	0.02	3.73	1.16	0.00	0.00	17.40	1.21	7.71	0.45	0.01	0.00
B5	WEA	0.20	0.03	6.34	0.93	0.01	0.00	0.99	0.05	4.78	0.18	0.14	0.02	0.65	0.27	0.69	0.04	0.08	0.02
B6	WEA	1.39	1.53	7.28	7.84	0.78	0.40	16.82	6.46	4.43	3.30	0.55	0.26	2.55	0.34	1.64	0.31	0.01	0.01
B7	WEA	5.21	5.06	16.51	17.05	0.20	0.15	16.06	5.54	2.95	2.23	0.22	0.20	5.41	1.36	2.54	0.76	0.01	0.00
B8	WEA	2.80	3.38	1.98	1.89	0.11	0.09	30.58	5.66	1.22	0.32	0.03	0.07	1.42	0.40	0.75	0.23	0.01	0.00
B9	WEA	1.19	0.11	3.45	0.89	0.02	0.01	1.29	0.15	4.95	0.25	0.13	0.01	1.18	0.34	0.94	0.10	0.09	0.02
B10	WEA	9.38	10.08	19.41	23.51	0.37	0.58	13.24	6.85	6.02	4.91	0.27	0.45	2.74	0.77	3.69	1.35	0.06	0.06
B11	SUL	0.00	0.00	0.07	0.04	0.60	0.55	19.46	3.16	3.83	0.79	5.81	3.22	4.64	0.76	5.02	0.92	1.88	0.55
B12	WEA	4.84	5.87	16.77	7.79	0.12	0.16	13.28	3.96	3.99	1.90	0.01	0.01	3.17	0.56	2.06	0.38	0.01	0.00
B13	WEA	0.83	0.34	0.25	0.05	0.22	0.25	18.91	4.17	4.20	0.87	0.03	0.05	0.98	0.43	2.20	0.33	0.01	0.00
B14	WEA	2.41	0.28	0.59	0.06	0.01	0.00	0.98	0.13	5.99	0.56	0.13	0.03	0.59	0.16	0.62	0.06	0.07	0.01
B15	WEA	1.08	0.05	3.51	0.65	0.09	0.13	1.48	0.59	6.76	0.37	0.13	0.04	1.30	0.79	0.87	0.12	0.06	0.01
B16	WEA	1.03	0.08	3.26	0.72	0.01	0.00	0.91	0.16	6.90	1.35	0.10	0.01	0.87	0.09	0.74	0.07	0.07	0.00
B17	SUL	1.12	1.92	1.08	2.62	2.68	2.97	26.34	4.43	1.58	2.67	0.16	0.23	2.37	0.49	6.18	1.96	2.75	1.35
B18	SUL	1.76	3.62	2.63	2.44	4.25	2.89	20.18	4.95	3.24	2.12	2.11	3.26	2.50	0.88	5.30	1.74	2.37	1.31
B19	SUL	0.32	0.23	5.14	2.52	0.03	0.02	11.96	4.11	12.34	5.31	0.17	0.07	2.36	0.43	1.20	0.16	0.01	0.00
B20	WEA	2.88	3.37	9.19	4.45	0.01	0.00	2.07	0.31	6.90	2.79	0.12	0.06	1.83	1.16	1.21	0.12	0.07	0.02
B21	WEA	0.68	0.58	4.76	3.39	0.06	0.03	9.67	2.42	7.29	2.53	0.23	0.02	1.19	0.37	0.72	0.11	0.01	0.00
B22	SUL	2.07	3.55	7.37	9.81	3.94	4.55	10.05	5.28	2.61	1.99	11.37	6.80	9.58	1.33	3.04	1.01	0.01	0.00
B23	SUL	1.77	2.83	13.23	11.55	5.93	3.7	17.76	5.65	4.14	2.17	5.06	3.97	7.25	1.67	2.43	1.02	0.01	0.00
B24	SUL	2.20	3.14	7.78	6.87	4.95	3.76	22.51	8.14	2.42	1.49	6.86	3.72	6.69	1.79	1.77	0.57	0.01	0.00
B25	SUL	1.34	3.16	6.65	11.07	2.46	3.03	6.32	4.82	3.24	1.71	13.79	6.80	6.96	1.83	1.68	1.26	0.03	0.06
B26	SUL	2.51	4.24	1.98	2.80	5.01	4.73	22.73	9.50	2.12	2.13	5.30	6.26	6.11	2.79	1.83	1.51	0.01	0.00
B27	SUL	3.46	3.13	11.30	7.44	6.82	3.14	14.29	8.16	1.97	1.31	5.41	3.89	4.96	1.03	1.41	0.46	0.01	0.01
B28	SUL	1.09	3.06	14.29	9.14	6.36	3.97	23.19	6.12	4.01	2.04	0.79	1.47	5.91	2.53	2.24	0.95	0.01	0.00
B29	SUL	3.93	5.04	4.72	3.08	5.90	4.43	23.16	6.56	2.38	1.01	3.43	3.73	5.91	2.34	2.05	1.11	0.01	0.00
B30	SUL	0.71	0.88	8.71	10.16	4.39	3.56	19.93	6.94	3.35	1.97	5.74	6.51	8.06	2.39	2.58	1.43	0.01	0.00
B31	SUL	0.40	0.51	1.35	2.03	2.32	1.75	20.05	7.00	3.01	2.47	4.01	5.95	4.62	1.28	5.09	1.66	1.78	0.91
B32	SUL	2.95	3.65	3.91	4.04	5.20	3.75	16.85	6.85	1.94	0.88	7.31	5.33	7.33	2.46	1.41	0.72	0.01	0.00
B33	SUL	1.91	3.54	2.67	2.71	2.35	2.64	6.39	7.83	1.99	0.53	13.25	6.64	9.89	2.57	0.36	0.18	0.01	0.00
B34	SUL	2.88	1.96	1.17	1.10	3.28	1.74	23.06	1.86	0.94	1.00	0.51	0.96	2.53	0.29	7.29	0.75	3.08	0.55
B35	SUL	3.16	3.66	3.52	2.86	0.01	0.01	17.00	4.00	6.27	2.21	0.13	0.10	2.40	0.46	1.10	0.44	0.01	0.00

A histogram of the cobalt content for both the weathered samples and sulphide samples is shown in Figure 6.1. The sample set is not normally distributed, again confirming that the samples have been selected based on high cobalt grade. It is interesting to see that for the Co grades below 15%, the weathered and sulphide distribution follow a similar trend.
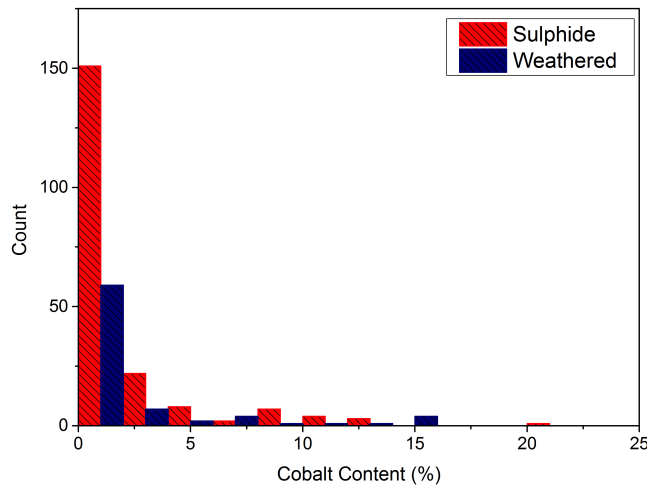
Figure 6.1: Histogram of Cobalt Content (%) for Weathered and Sulphide Samples

6.1.1. Sample Selection for Further Characterisation

A number of samples need to be selected in order to be analysed for mineralogical data. Samples are selected based on the Co grade obtained using portable XRF. For calibration of QEMSCAN used in the next section, the sample with the highest Co content is selected.

Using a normal distribution based selection procedure is not appropriate, as the Co grade data did not follow a normal distributed trend (Figure 6.1). A step function is used based on the average, minimum and the maximum Co grade. Two histograms of the selected sulphide and weathered samples are shown in Figure 6.2, with the same bin size as the histogram in Figure 6.1. The Co trend of the selected sulphide samples is similar to the dataset, with the highest number of counts for the lowest bin sizes. The trend is different for the weathered samples, showing that higher cobalt grade bins have more counts than the lower grade bins. This needs to be kept in mind when using the weathered samples as the basis for a geometallurgical model, as for the weathered zone the selected samples are not representative for the full sample set.
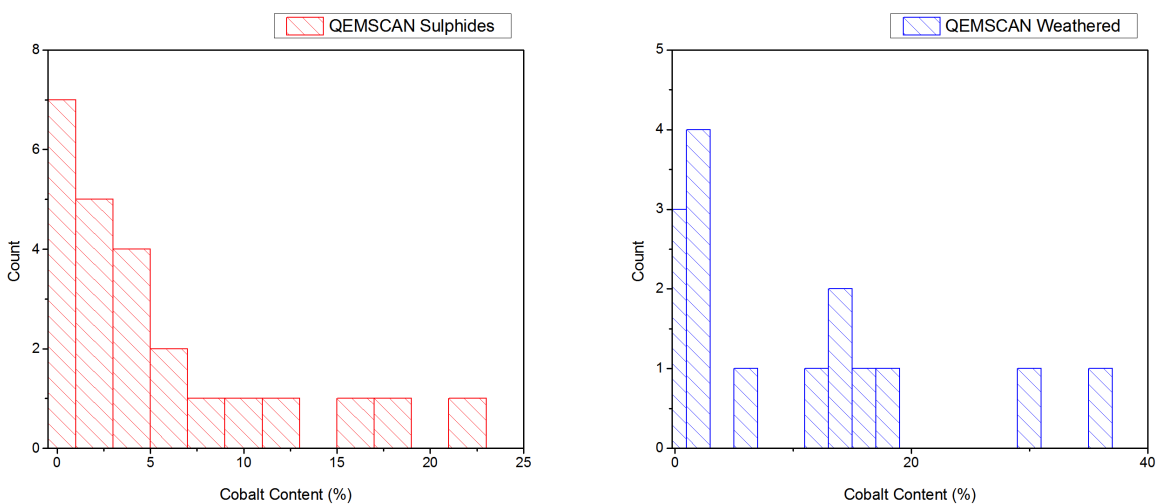
Figure 6.2: Histogram of Cobalt Content (%) Selected for QEMSCAN

6.2. QEMSCAN

The results obtained using the QEMSCAN shall be discussed here. Firstly, the differences in mineral texture and modal mineralogy for both the weathered and sulphide zone will be set out. Secondly, the mineral associations and average grain sizes of the sulphide samples will be discussed.

6.2.1. Mineral Texture

The first step to understanding the influence of mineralogy on the comminution process is by determining the different mineral texture types. Five and six different textures can be distinguished for the weathered and sulphide samples respectively. It must be noted that all the following images are falsely coloured. The elements per mineral and associated colour coding can be found in Appendix B.

Weathered Massive   The first weathered texture is shown in Figure 6.3. This type is classified as *Weathered Massive*, due to the presence of a massive and continuous malachite zone. The cobalt mineral here is kolwezite, together with cupro-asbolane and malachite the three dominant minerals.
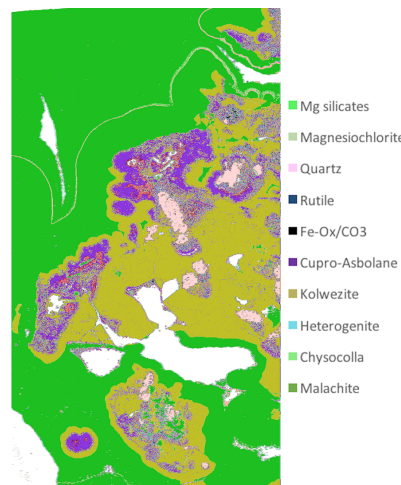
Figure 6.3: Weathered Massive Mineral Texture: W-10

Weathered Kolwezite   Figure 6.4 shows the texture *Weathered Kolwezite*. It is classified as such due to large areas of kolwezite being present. The sample on the left, W-25, could also be classified as *Kolwezite Massive*. The kolwezite occurs in patches accompanied by zones of malachite, disseminated heterogenite, cupro-asbolane and quartz.
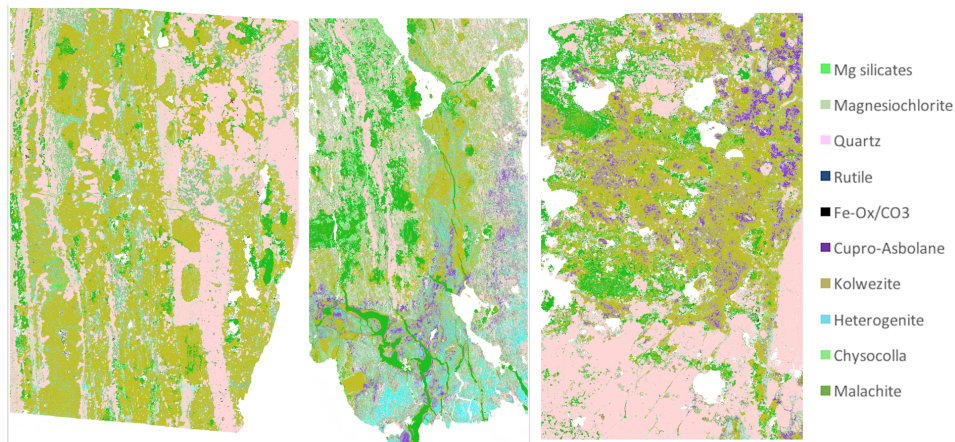
Figure 6.4: Weathered Kolwezite Mineral Texture: W-25, W-83 and W-88

Weathered Disseminated   The texture *Weathered Disseminated* is displayed in Figure 6.5. Both heterogenite and kolwezite occur spread out through the quartz hosted sample. W-33 also occurs with patches of Fe-Oxide. The grain sizes of the valuable minerals are considered to be fine in all the samples.
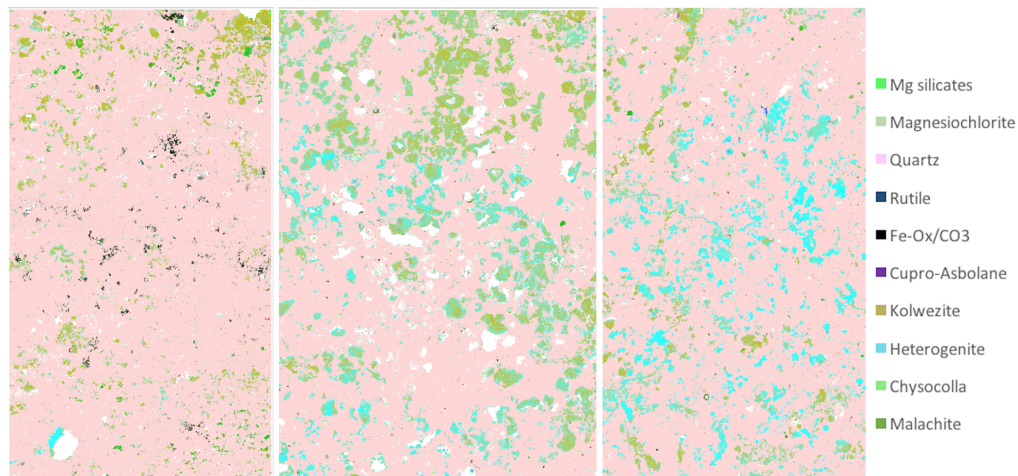
Figure 6.5: Weathered Disseminated Mineral Texture: W-33, W-44 and W-58

Weathered Vein   Figure 6.6 shows the *Weathered Vein* texture. W-12 contains veins of both malachite and kolwezite that have penetrated the host rock, possibly due to a hydrothermal event. W-31 mainly contains a malachite vein, with patches of disseminated kolwezite around the malachite vein.
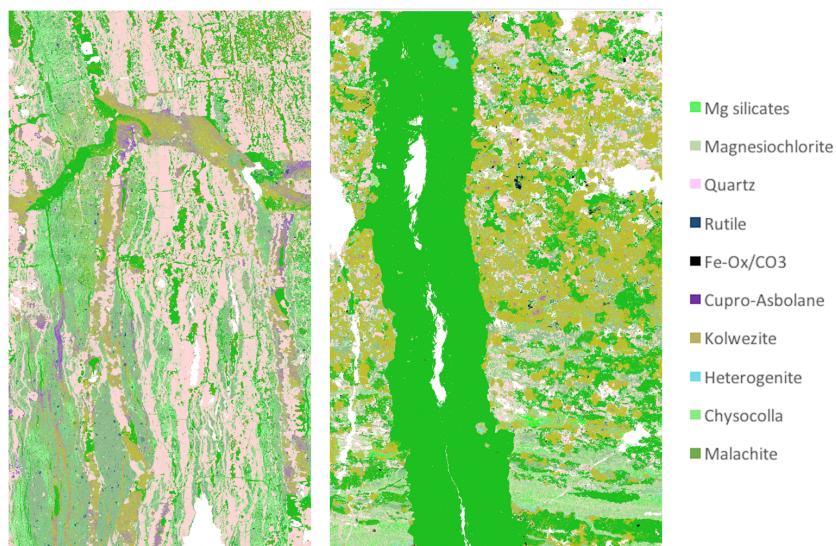
Figure 6.6: Weathered Vein Mineral Texture: W-12 and W-31

Weathered Gangue   The final weathered texture type is defined as *Weathered Gangue*, shown in Figure 6.7. No valuable minerals are present within this texture type.
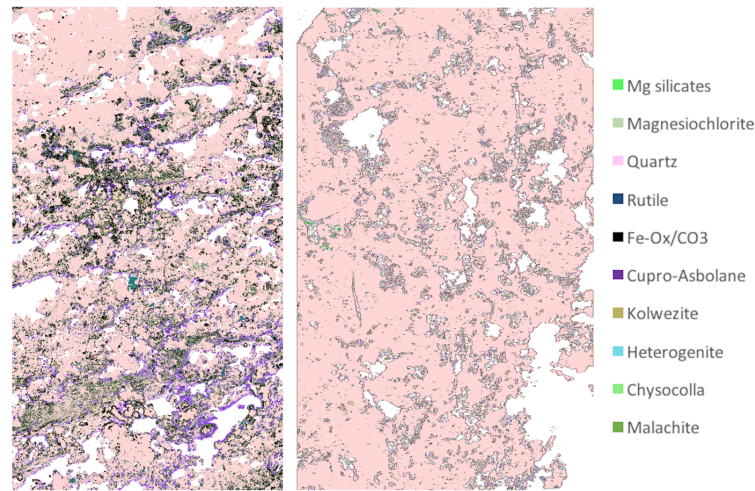
Figure 6.7: Weathered Gangue Mineral Texture: W-160 and W-170

All the weathered samples showed to have been influenced by the weathering process, indicated by the white patches in the images (background) and the observation that most valuable minerals are fine grained. The number of samples per texture type is shown in Table 6.2. The kolwezite, disseminated and gangue texture type are the most common ones. In reality the gangue mineralisation will be the most common texture type.

Table 6.2: Number of Samples per Weathered Texture Type

	Massive	Kolwezite	Disseminated	Vein	Gangue
Number of Samples	1	3	4	2	3

Sulphide Massive   The first sulphide texture type is shown in Figure 6.8. This texture is classified as *Massive Carrollite*. One QEMSCAN sample can be classified as this texture. This is also the sample that has been used for carrollite calibration in the Sample Identification Protocol. There are some flakes of other minerals present, both gangue (quartz, chlorite and dolomite) and valuable (chalcopyrite).
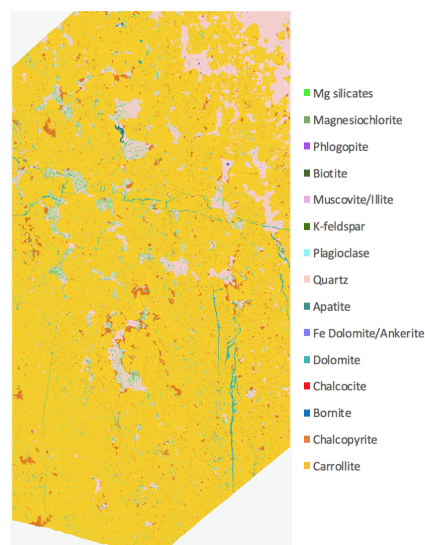
Figure 6.8: Sulphide Massive Mineral Texture: S-279

Sulphide Coarse Disseminated   Figure 6.9 shows a different type of mineral texture: *Coarse Disseminated Carrollite*. The carrollite is present in very coarse grains. S-200 contains a small number of grains, whereas S-314 is mainly carrollite and S-421 contains both coarse and finer grains of carrollite. It is also possible to classify S-421 as a *Banded* texture type. The amount of carrollite varies per sample. The gangue minerals are quite similar, as all samples contain quartz, dolomite and Mg silicates. No other valuable minerals are present.
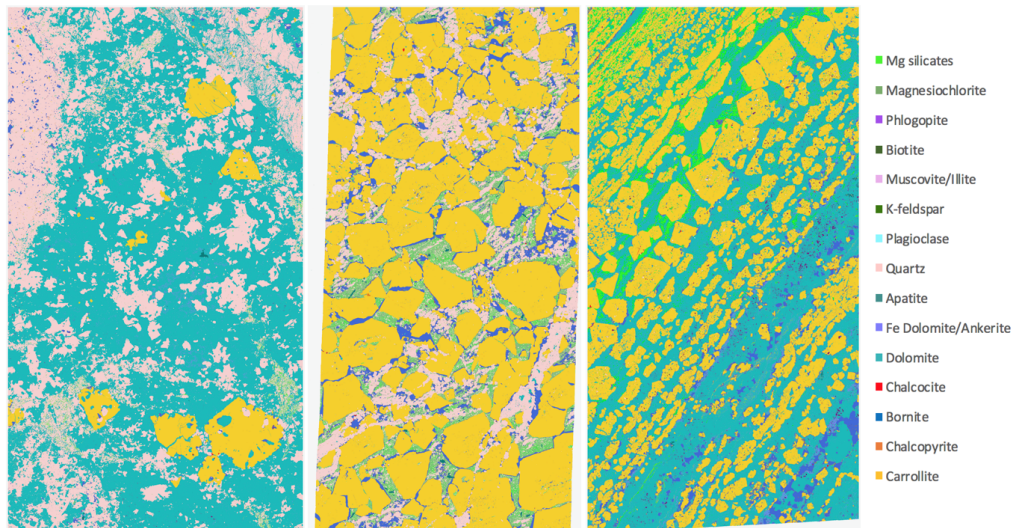
Figure 6.9: Sulphide Coarse Mineral Texture: S-237, S-314 & S-421

Sulphide Fine Disseminated   The texture classified as *Fine Disseminated Carrollite* is shown in Figure 6.10. In all three images the carrollite is spread out throughout the whole sample. The host mineralisation mainly consists of quartz and dolomite (S-273 and S-308), whilst also containing some bornite, chalcopyrite and chalcocite. S-403 contains also a significant amount of chlorite and Mg silicates, with an area of massive carrollite in the middle. The large carrollite area would allow for S-403 to be classified as a *Massive* texture.
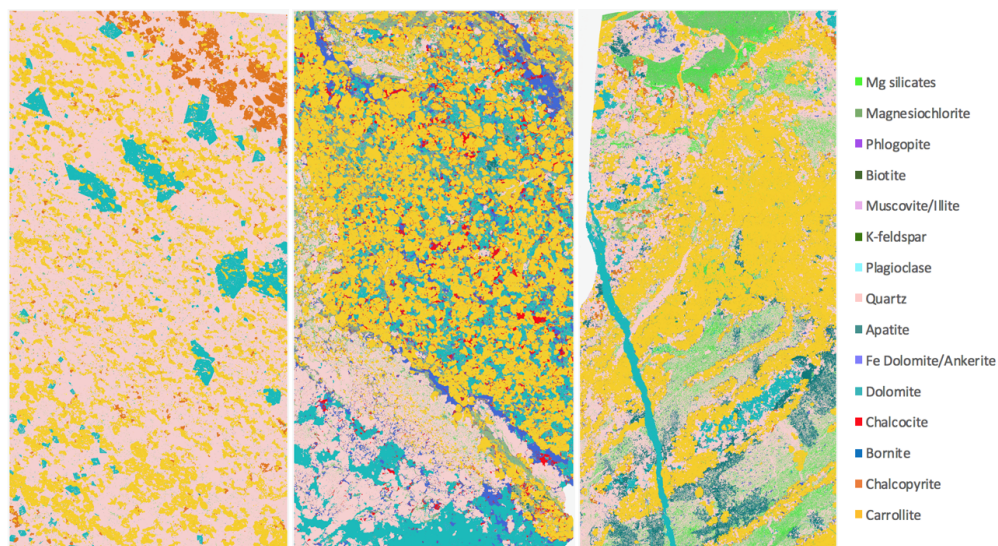
Figure 6.10: Sulphide Disseminated Mineral Texture - S-273, S-308 & S-403

Sulphide Vein   Figure 6.11 shows the *Carrollite in Veins* texture type. Clear lines of precipitated carrollite mineralisation occur regularly and ordered in the sample. The veins also contain quartz and chalcopyrite for

S-135 and S-426. The veins of S-263 contain mainly dolomite. The host rock mainly contains chlorite (S-263) and K-feldspar (S-135 and S-426).
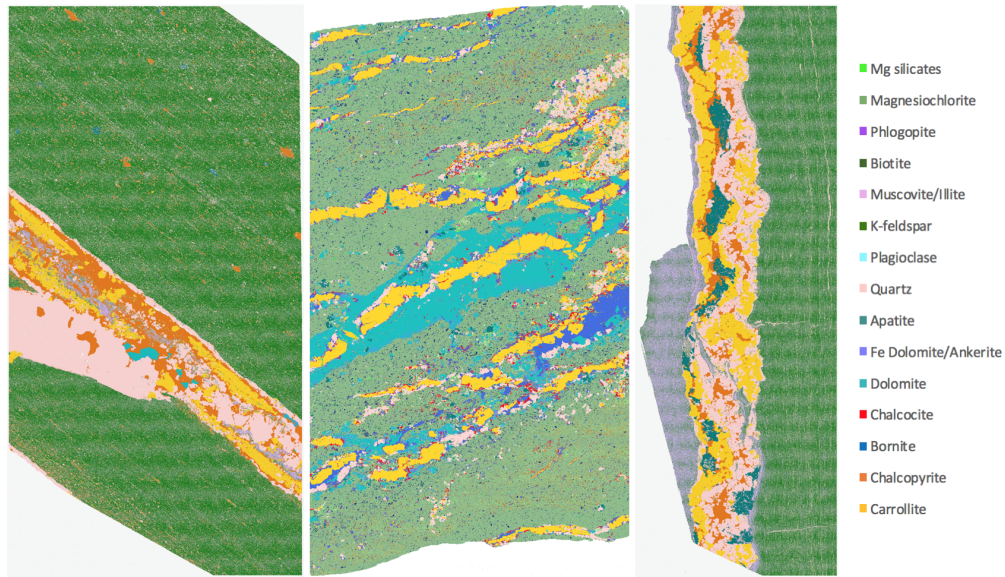
Figure 6.11: Sulphide Vein Mineral Texture: S-135, S-263 & S-426

Sulphide Banded   In Figure 6.12 the *Banded Carrollite* texture type is shown. The samples are ordered in a stratiform manner. Carrollite is mainly associated with Mg silicates and dolomite. The impact of tectonic movement can clearly be seen in S-278, due to the bend of the mineralisation. In all three samples again Mg silicates, dolomite and quartz can be found. Occasionally bornite is present as well (S-188 and S-200), whereas S-278 contains chalcopyrite.
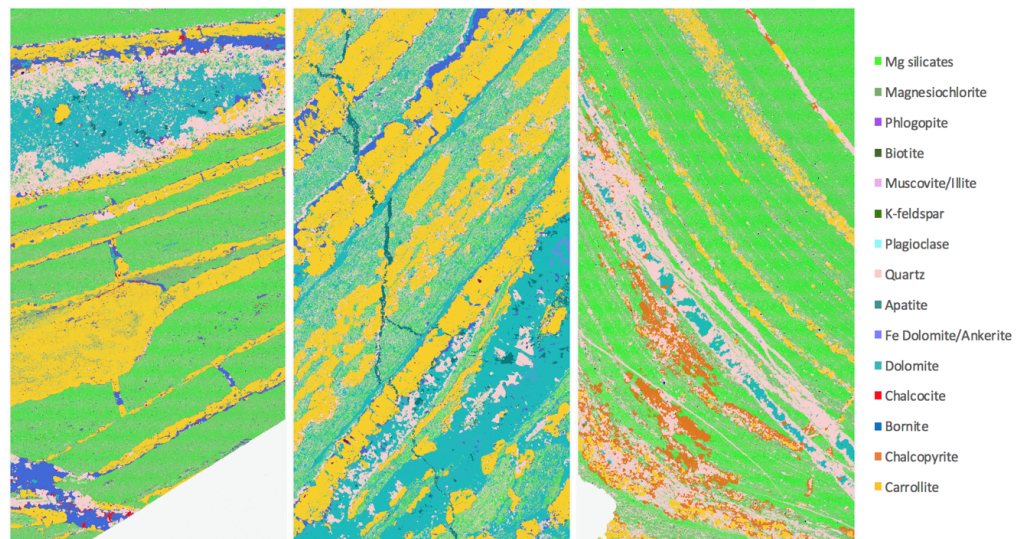
Figure 6.12: Sulphide Banded Mineral Texture: S-188, S-200 & S-278

Sulphide Gangue   The final mineral texture contains no carrollite and is classified as *Gangue*. The gangue texture is useful in understanding the different types of host rocks and thus the difference in gangue minerals that can enter the processing plant and in stope design.
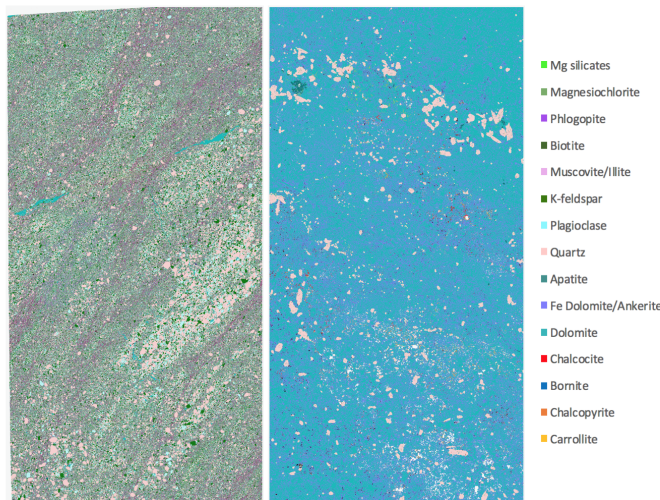
Figure 6.13: Sulphide Gangue Mineral Texture: S-80, S-258 & S-442

The number of samples per texture classification are shown in Table 6.3. The majority of the sulphide samples are either coarse or fine disseminated. In reality, the gangue mineralisation is probably the most dominant texture type. As the samples have been selected based on cobalt content, the majority of the textures represent carrollite textures. It was also shown on two occasions that texture is not always a clear property, it can be mixed. This makes the classification process a subjective one and thus not always accurate. It is expected that these different textures have a unique response in the comminution process. The sulphide textures have no zones of background (white) within the sample, showing that these samples have not been affected by a weathering process.

Table 6.3: Number of Samples per Sulphide Texture Type

	Massive	Coarse Disseminated	Banded	Fine Disseminated	Vein	Gangue
Number of Samples	1	6	3	7	4	2

6.2.2. Modal Mineralogy

The modal mineralogy of the weathered samples is shown in Figure 6.14. For these texture types a declining trend in malachite is observed. This declining trend is accompanied by an increase of heterogenite. In general, the main gangue mineral is quartz, as significant proportions are present in all samples. Magnesiochlorite and Fe-Ox are also present in the all of the texture types.
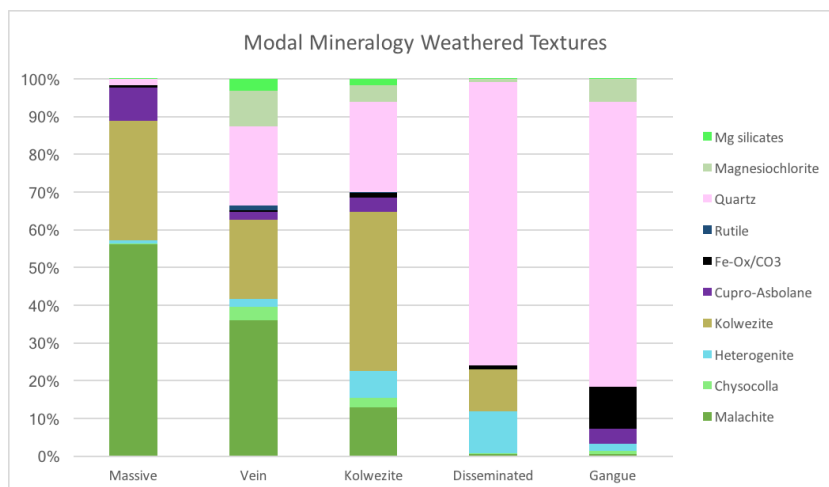
Figure 6.14: Modal Mineralogy for the Five Distinguished Weathered Texture Types

The modal mineralogy of the distinguished sulphide mineral textures is shown in Figure 6.15. There are two minerals that are present in large quantities in all the samples: carrollite and quartz. There is a decreasing carrollite trend, going down from massive to vein type textures. The amount of Mg silicates is significantly lower for the coarse and fine disseminated texture types. Chlorite is mainly found in the banded and vein texture type. Another interesting observation is the presence of both chalcocite and K-feldspar in the fine disseminated and vein type texture. There is a significantly larger amount of K-feldspar present in the vein type. In general, carrollite and chalcopyrite are the main valuable components. Carrollite is present in significant quantities, this implies that it should be easy to detect carrollite after comminution has taken place.
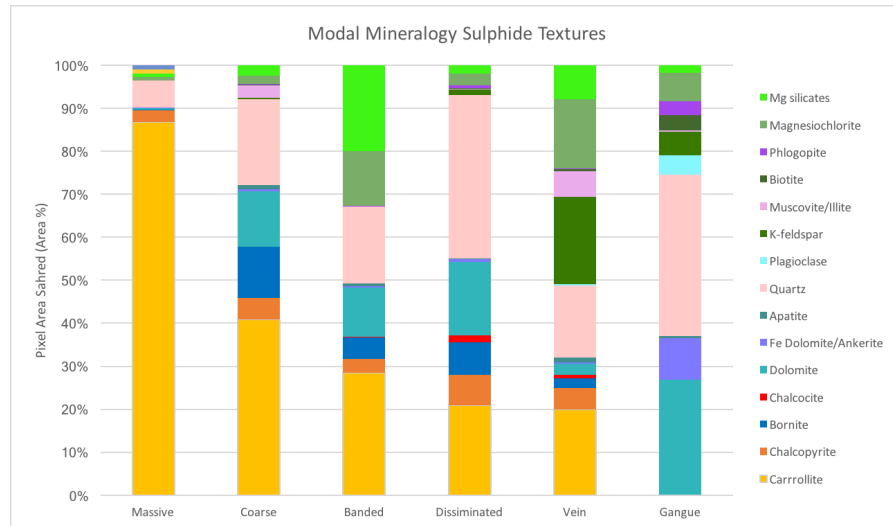
Figure 6.15: Modal Mineralogy for the Six Distinguished Sulphide Texture Types

The significant proportions of carrollite imply that a substantial amount of cobalt is present. A box chart for the cobalt grade per sulphide mineral texture is shown in Figure 6.16. The cobalt trend follows a nearly identical trend as to the carrollite volume, which is expected.
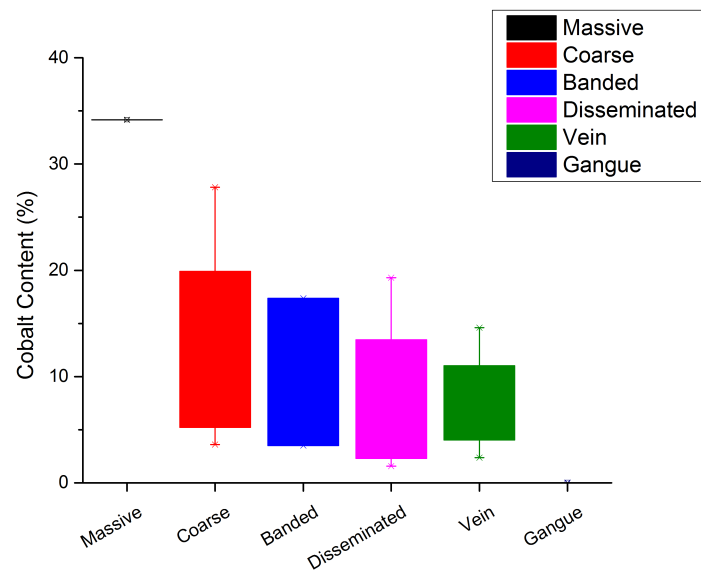
Figure 6.16: Box Plot of Co Content (%) for the Six Distinguished Sulphide Texture Types

6.2.3. Mineral Associations

Mineral associations have a large impact on the processing parameters of carrollite. If carrollite is heavily associated with difficult gangue minerals, the comminution and metallurgy steps will become more difficult. To interpret the QEMSCAN results, it has to be kept in mind that the mineral associations are only given along the horizontal axis and not both horizontal and vertical.

The average mineral associations for carrollite per texture type are shown seen in Figure 6.17. In all cases carrollite is associated with other valuable mineralisations, such chalcopyrite, chrysocolla and bornite. The main gangue minerals are dolomite and quartz. The banded and finely disseminated texture have a smaller mineral association with dolomite compared to the coarse and vein type textures.

It is interesting to see that even though the fine and coarse disseminated texture type have a smaller proportion of chlorite present, carrollite is still clearly associated with it. The opposite is true for the vein texture. The disseminated texture types both have a distinct association with biotite, with it being the largest for the fine disseminated type. It appears that in, if a mineral is present in a sample than carrollite is associated with it.
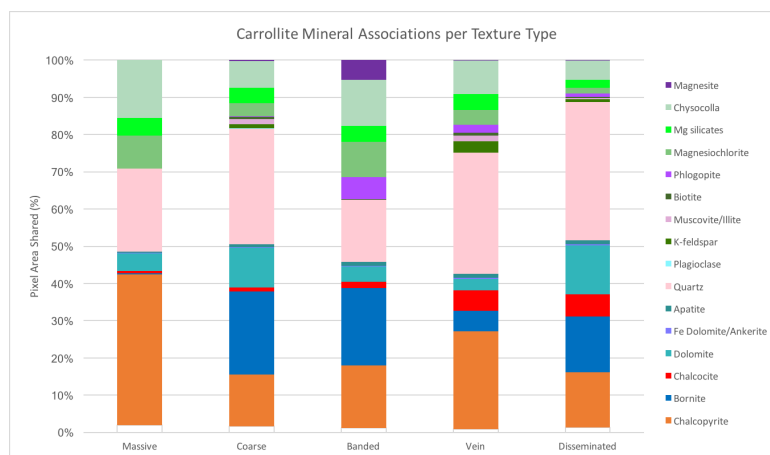
Figure 6.17: Minerals Associated with Carrollite for the Five Valuable Sulphide Textures Types

6.2.4. Mineral Grain Sizes

Grain sizes can also be determined using QEMSCAN. The average values for the mineral textures are shown in Table 6.4. Carrollite has the largest average grain size, ranging from 222 μm to 389 μm. The other minerals present in the samples have a significant smaller average grain size. Quartz and dolomite also have relatively large average grain size values. Biotite has the smallest average grain size, but the other gangue and valuable minerals have small average grain sizes as well for all mineral textures.

Table 6.4: Average Mineral Grain Size per Texture Type (μm)

	Massive	Coarse	Banded	Disseminated	Vein	Gangue
Carrollite	389	385	263	222	275	16
Chalcopyrite	37	54	53	69	75	17
Bornite	25	62	66	52	30	22
Chalcocite	15	19	24	22	20	24
Dolomite	44	157	111	151	90	37
Fe Dolomite/Ankerite	18	17	17	18	21	23
Apatite	45	58	79	50	113	95
Quartz	100	138	50	208	47	113
Plagioclase	≤15	18	18	16	≤15	20
K-feldspar	≤15	17	≤15	18	31	20
Illite	≤15	32	≤15	17	23	17
Biotite	≤15	16	≤15	16	16	16
Phlogopite	≤15	17	18	20	19	18
Magnesiochlorite	25	28	26	29	47	21
Mg silicates	20	25	32	23	22	17

The grain size distribution for the carrollite grain sizes per texture is shown in Figure 6.18. The massive type only has one sample, explaining the single line. The coarse samples have a higher average and maximum grain size. The vein, banded and disseminated texture type all have a similar grain size. The gangue texture shows very small carrollite grain sizes, as carrollite is not present in significant proportions.
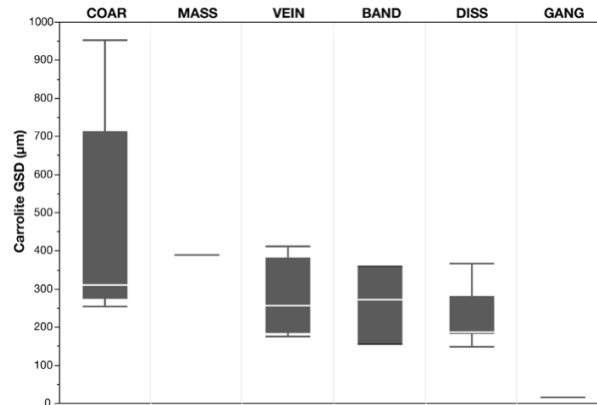
Figure 6.18: Box Plot of Average Carrollite Grain Sizes for Different Texture Types

It is interesting to see the variation in carrollite grain size, as this strengthens the expectation of the different mineral textures having different responses in the comminution process. What is worrying, is the small grain sizes of several gangue minerals. Even gangue minerals that are present in significant proportions (magnesiochlorite, illite and Mg silicates), have a small grain size. This will have consequences for the liberation of the valuable materials, such as carrollite, bornite and chalcopyrite. It will be difficult to completely liberate the carrollite, as it will require grinding of the material to a very small diameter. A positive side is that the ground fraction of the large carrollite grains will most likely break down in completely liberated parts.

6.3. Surface Hardness

6.3.1. Calibration

The influence of decreasing mass on the Leeb Hardness and the associated standard deviation are shown in Figure 6.19. Using Origin Pro 9 an exponential decay fit could be assigned to the data.
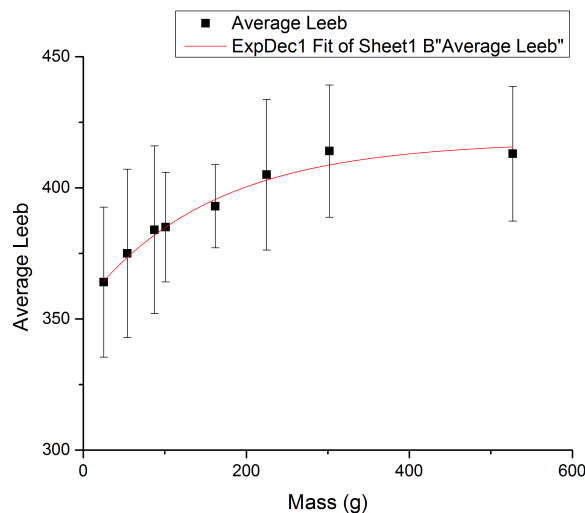
Figure 6.19: Impact of Sample Mass *(g)* on Measured Surface Hardness *(LH)*

A downwards trend in measured Leeb Hardness is observed for a mass below 300 grams. Based on the exponential fit an empirical adjustment factor can be deduced that will allow for a more realistic comparison

of samples having a different mass. The Adjustment Factor (AF) is calculated as follows:

$$AF = -0.38 + 17.1e^{-\frac{m}{132}} \tag{6.1}$$

Where m is the mass of the drill core sample in grams. This factor is a percentage and will need to be multiplied with the measured surface hardness for core samples with a mass below 300 grams.

6.3.2. Drill Core Surface Hardness

The Equotip was also tested for usefulness in measuring the surface hardness of quarter core samples. Measurements were performed on all the suitable pieces of drill core. The results for a random selection of samples are shown in Table 6.5. For each sample the mass, the number of Equotip measurements (hits), the average, maximum, minimum and standard deviation of the unadjusted Leeb Hardness is given. On the right side of the table the mass dependent adjustment factor and adjusted surface hardness are given. Each sample represents one piece of drill core from a sample bag.

Table 6.5: Information of Randomly Selected Surface Hardness Measurements and Adjustment Factor Example

Sample Bag	Number	Mass (g)	Hits	Average Leeb(LH)	Max Leeb(LH)	Min Leeb(LH)	StDev	Adjustment Factor	Adjusted Leeb(LH)	Adjusted Average(LH)
B18	1	62.8	6	543	611	414	68	10.06	597	614
	2	78.3	5	520	756	419	136	8.91	566	
	3	78.8	7	610	625	566	20	8.87	665	
	4	75,9	6	561	586	501	36	9.09	612	
	5	74.3	9	577	686	453	90	9.21	630	
B24	1	186.9	8	619	856	511	112	4.47	647	750
	2	152.5	7	841	871	812	24	6.1	893	
	3	117.2	5	603	673	541	47	7.3	647	
	4	129.5	6	761	828	651	64	6.94	814	
B27	1	64.5	4	593	662	423	114	8.16	641	636
	2	116.3	5	604	620	578	19	7.42	649	
	3	151.0	10	656	787	470	114	6.16	697	
	4	172.6	10	528	793	352	123	5.20	555	

This adjustment factor has been applied to all pieces of drill core. The impact of the adjustment factor on the overall distribution of the Leeb Hardness is shown in Figure 6.20. The adjusted distribution follows a trend that is more similar to a normal distribution, showing the positive impact of the adjustment factor.
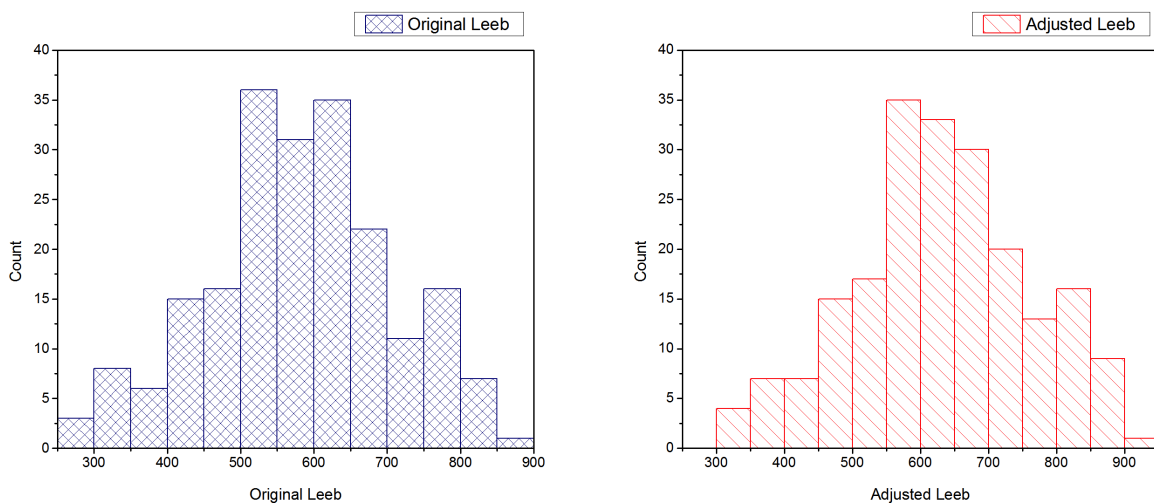
Figure 6.20: Histogram of the Unadjusted Leeb Hardness Distribution (left) and Adjusted Leeb Hardness (right)

Figure 6.21 shows a scatter plot of the adjusted surface hardness versus the cobalt content per sample. No clear correlation can be found. This is emphasised by the scattered cloud on the right hand side and a large range of surface hardness values for samples with very little cobalt on the left.
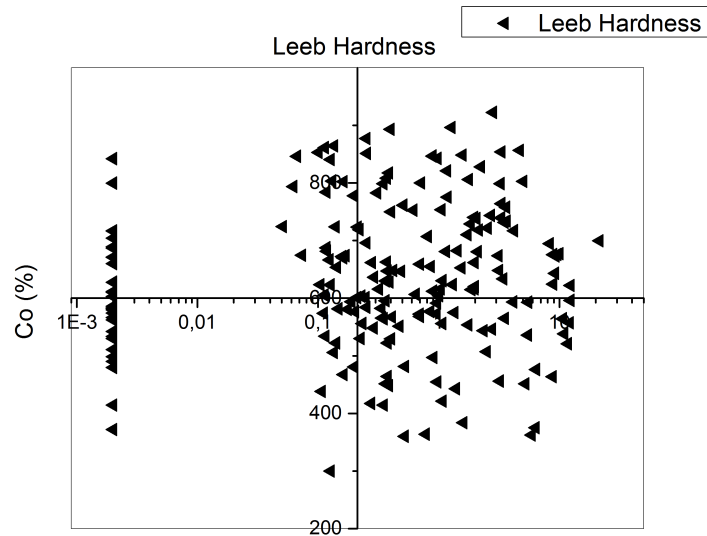
Figure 6.21: Scatter Diagram of Co Content (%) vs. Leeb Hardness

The distribution of adjusted Leeb Hardness per mineral texture is shown in Figure 6.22. The fine disseminated type has the largest range in surface hardness and there appears to be a decreasing trend along the banded - fine/coarse disseminated - vein texture types.
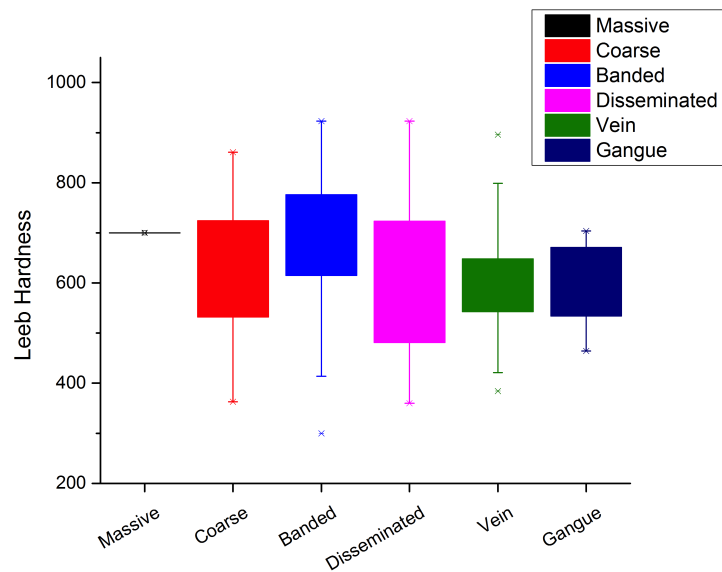
Figure 6.22: Box Plot of Leeb Hardness for Distinguished Mineral Textures

6.3.3. Mineral Texture

The influence of mineral texture on the measured surface hardness is visualised by creating contour-plots and by comparing the contour-plot results to the QEMSCAN 2D images. Using this method, it is possible to identify till what detail the Equotip can provide information. The QEMSCAN images have been modified, so that in the report the area of the contour-plot and the QEMSCAN image are the same. The white regions surrounding the contour-plot are due to the resolution of the Equotip: due to the large diameter of the tip it is required to avoid measurements to close to the edge of a sample.

There are two important limitations that need to be considered when interpreting these results:

- QEMSCAN gives mineralogical information in 2D, whereas the Equotip is also a reflection of the subsurface and neighbouring mineralisation. Differences are expected.

- The Equotip has a diameter of 3 *mm* and a surrounding base of 25 *mm*. Both these factors are limiting the resolution of the measurements and the accuracy of the position. This means that there is a large chance that the contour plot shown is not 100% representative for the indicated QEMSCAN area.

As a reference of mineral hardness, Mohs hardness is used. A summary of Mohs hardness for the main minerals is given in Table 6.6. Based on this information it is probable that areas with quartz or carrollite will have a higher surface hardness compared to areas with Mg silicates. In the contour-plots blue indicates an area of low surface hardness and red an area of high surface hardness.

Table 6.6: Mohs Hardness of the Main Minerals (Mindat.org [64])

Mineral	Carrollite	Chalcopyrite	Dolomite	Quartz	Magnesiochlorite	Mg silicates
Hardness (Mohs scale)	4.5 - 5.5	3.5-4	3.5-4	7	2-2.5	1.0-2.0

Figure 6.23 shows the surface hardness contour-plot of S-278. The QEMSCAN image shows a banded texture, with both carrollite, quartz, dolomite and chalcopyrite veins hosted by Mg silicates. The contour-plot indicates two zones of high hardness, the pure quartz vein in the top left and the chalcopyrite-quartz mixture in the bottom right (3). The surface hardness of the carrollite veins is not very consistent, indicated by (1) and (2). This shows that similar looking areas can have a significant difference in surface hardness.
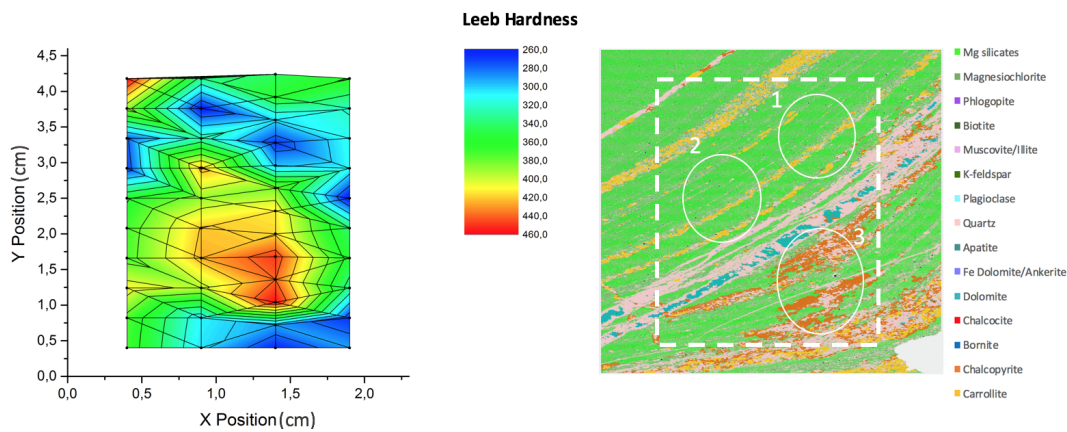
Figure 6.23: Contour-plot of Leeb Hardness vs. Modified QEMSCAN Image of S-278

Sample S-314 has a different texture, as is shown in Figure 6.24. This sample consists mainly out of coarse carrollite grains with varying grain sizes, surrounded by quartz and Mg silicates. From the contour-plot it can be seen that carrollite mixed with Mg silicates has a lower surface hardness, as is indicated by the large blue patch (2). The area with a mixture of quartz and carrollite has a higher surface hardness, indicated by (1).
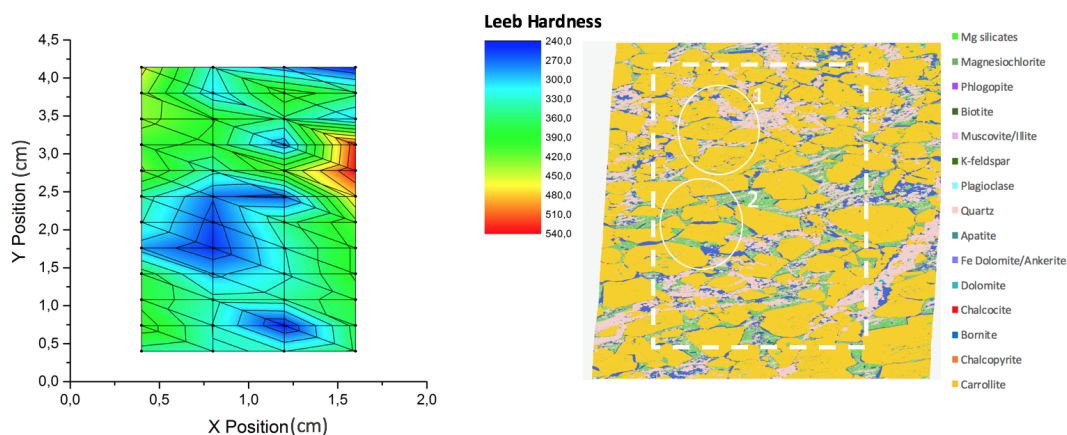
Figure 6.24: Contour-plot of Leeb Hardness vs. Modified QEMSCAN Image of S-314

Figure 6.25 shows the contour-plot and modified QEMSCAN image of S-403. After the three horizontal measurements, the sample had broken meaning that a smaller contour plot was obtained. The large homogeneous patch of carrollite has the lowest surface hardness (2). An area containing quartz, carrollite and Mg silicates has the highest surface hardness (3). A mixture of carrollite, dolomite and quartz has a higher surface hardness than the homogeneous carrollite zone (1). This contains information about brittleness of carrollite when it is present as a single mineral.
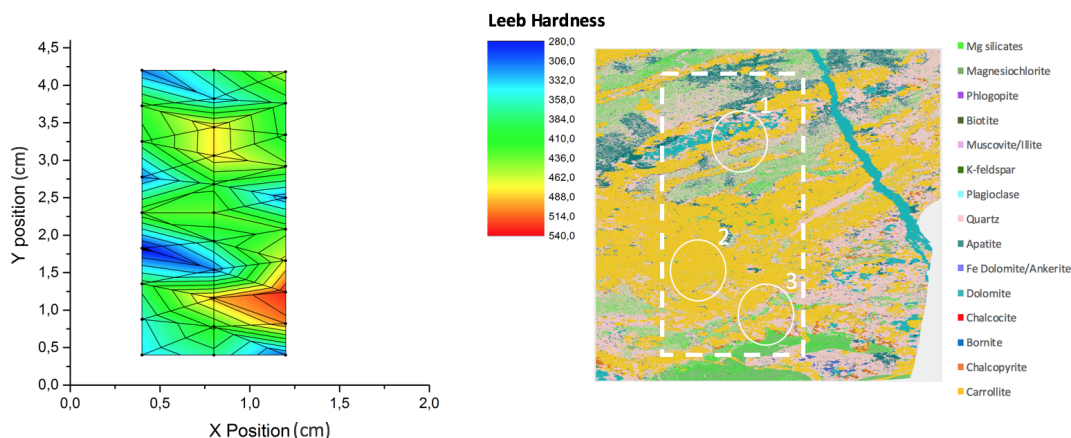
Figure 6.25: Contour-plot of Leeb Hardness vs. Modified QEMSCAN Image of S-403

The contour-plots have given an interesting insight about the level of detail to which surface hardness can be assessed using the Equotip. Areas of Mg silicates were identified to have a lower surface hardness and areas of quartz a high surface hardness. This shows the effect of the 'glue minerals' on the surface hardness. It was interesting to see that an area of nearly pure carrollite with no grain like texture had a very low Leeb hardness.

The Equotip has proven to be a useful tool in studying differences in the surface hardness, of both samples with different mineral textures and on quarter core samples. At this moment it is not clear what a surface hardness value implies for mineral processing, as there are no studied correlations between measured surface hardness and processing parameters. This correlation will be considered in section 6.6 .

6.4. Mid InfraRed Spectroscopy

In total 325 spectra within the 2500 and 15500 *nm* wavelength range were obtained from 21 samples. The influence of background noise is considered to be minimal, as it is automatically removed by the FTIR 4300. The measured spectra will be divided into two sections: spectra that are considered to be pure and mixed spectra. In order to aid with interpretation, reference spectra are used (Clark et al. [19]).

6.4.1. Pure Mineral Spectra

The reference spectrum (relevant zone indicated by the marked area) and measured spectra of pure dolomite are shown in Figure 6.26. The measured spectra are visually very similar to the reference spectrum. The feature at 6450 *nm* (B) is due to bending of the C-O bond and the feature at 11200 *nm* (C) due to the stretching of the C-O bond as reported by Salisbury et al. [86]. In the reference spectrum an additional feature can be found around 13000 *nm*, it is not clear why that is missing in the measured spectra. An additional feature is found at 4300 *nm* (A), that is in agreement with the reference spectrum. It is not clear what causes this feature. The presence of dolomite has been confirmed using QEMSCAN data.
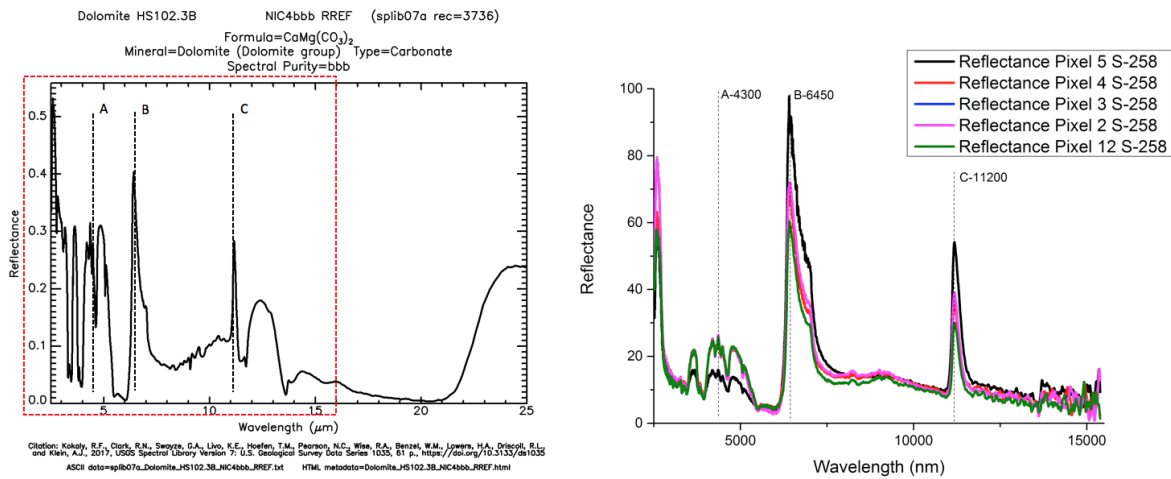
Figure 6.26: Reference Spectrum of Dolomite (Clark et al. [19]) and Measured Dolomite

Figure 6.27 shows a reference spectrum on the left (relevant zone identified by red marking) and the measured spectra of quartz. The features at 8500 *nm* (B) and 12500 *nm* (C) are in agreement with the Si-O stretching reported by Salisbury et al. [86]. An additional feature is found around 3900 *nm* (A), which is in agreement with the reference spectrum. It is not known what causes this feature. The presence of quartz has been confirmed using QEMSCAN data.
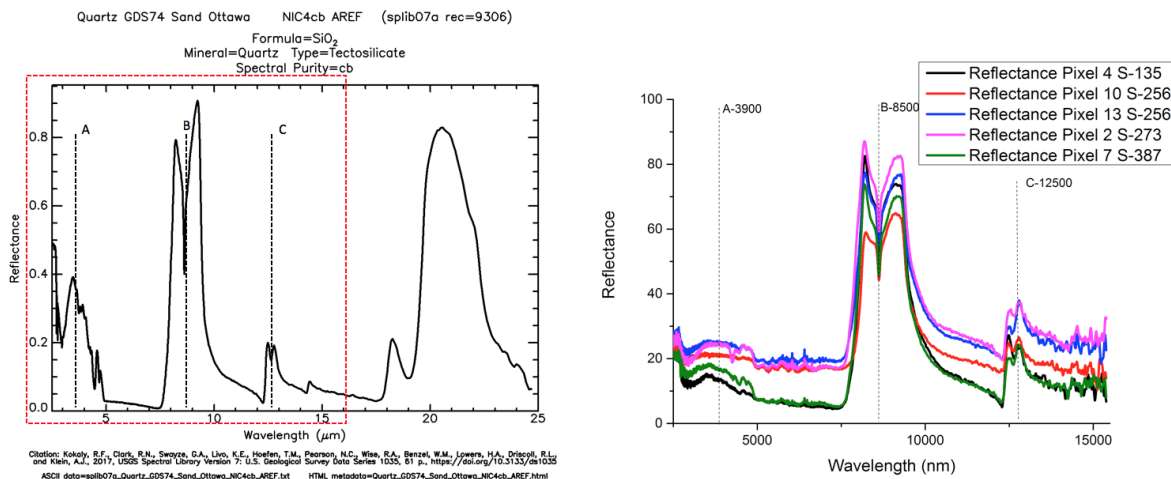
Figure 6.27: Reference Spectrum of Quartz (Clark et al. [19]) and Measured Quartz

The reference spectrum of chlorite (relevant zone identified by red marking) and measured chlorite spectra are shown in Figure 6.28. The features at 3900 *nm* (A) and 6500 *nm* (B) are due to the stretching of Mg-OH. The feature at 9600 *nm* (C) is due to the stretching of the Si-O bond. The measured spectrum shows to be in good agreement with the reference spectrum. The presence of chlorite has been confirmed using QEMSCAN data.
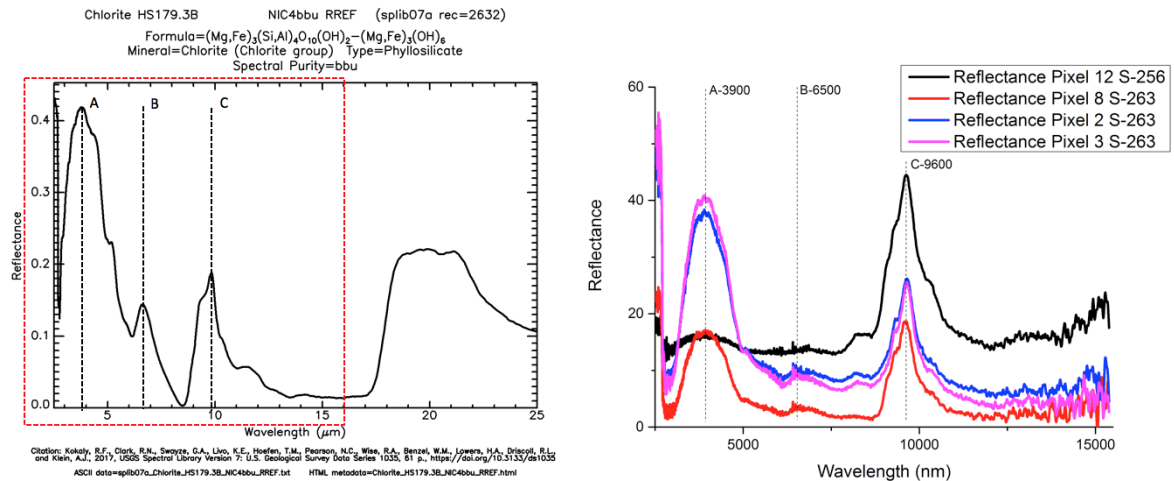
Figure 6.28: Reference Spectrum of Chlorite (Clark et al. [19]) and Measured Chlorite

A reference spectrum of chalcopyrite (no reference spectrum of carrollite can be found, relevant zone identified by red marking) and measured spectra of pure carrollite are shown in Figure 6.29. The reason for showing the chalcopyrite reference spectrum is to get an indication of the behaviour of sulphide minerals in this region. What both spectra have in common is a noise feature around 6500 *nm* (A). The carrollite spectrum shows a flat feature in the spectrum around 8300 *nm* (B) and 9500 *nm* (C), where it is different from chalcopyrite. Even though carrollite appears to have a unique spectrum, it does not contain any significant minima or maxima that would allow carrollite to be distinguished in mixed spectra. The presence of carrollite has been confirmed using QEMSCAN data.
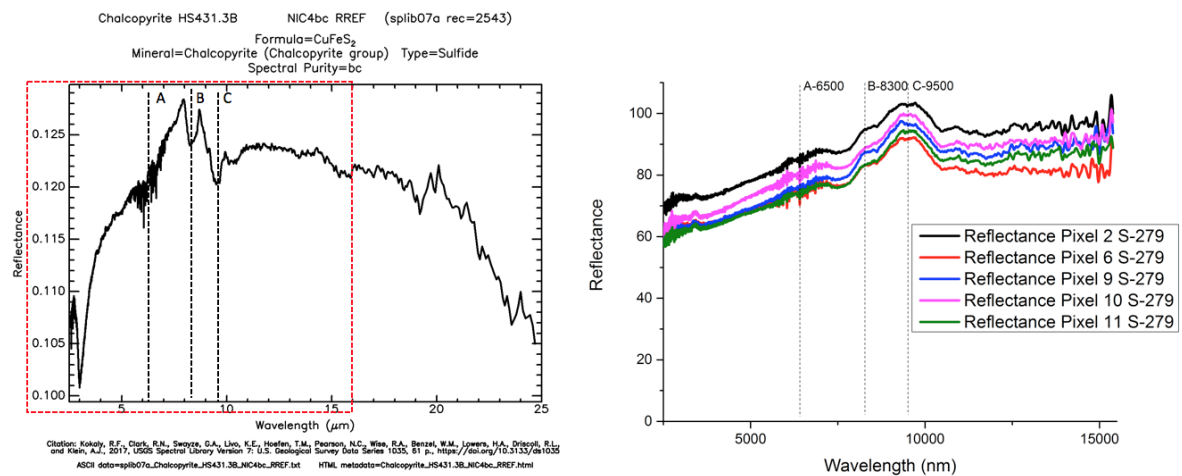
Figure 6.29: Reference Spectrum of Chalcopyrite (Clark et al. [19]) and Measured Carrollite

6.4.2. Mixed Mineral Spectra

The majority of the measured spectra are a mixture of IR active minerals. According to Thomson and Salisbury [94] these signals can be added linearly if the grain size is larger than 60 *µm*. When considering the average grain sizes of the measured using QEMSCAN in Table 6.4, only quartz and dolomite have an average grain size greater than 60 *µm*. This means that when interpreting the majority of the mixed spectra, additional maxima and minima can be expected for mixed spectra (Thomson and Salisbury [94] and Ramsey and Christensen [81]). An attempt was made to create a mixed reference spectrum using linear addition of reference spectra. In some cases important features disappeared when adding the spectra. For those spectra original reference spectra are given, instead of the created mixed spectra.

Figure 6.30 shows the created reference spectrum and measured spectra of samples containing dolomite and quartz. The C-O (A and C) and S-O (B and D) features defined in the pure minerals can be clearly identified. The created reference spectrum shows to be visually in agreement with the measured spectrum. The presence of dolomite and quartz has been confirmed using QEMSCAN data.
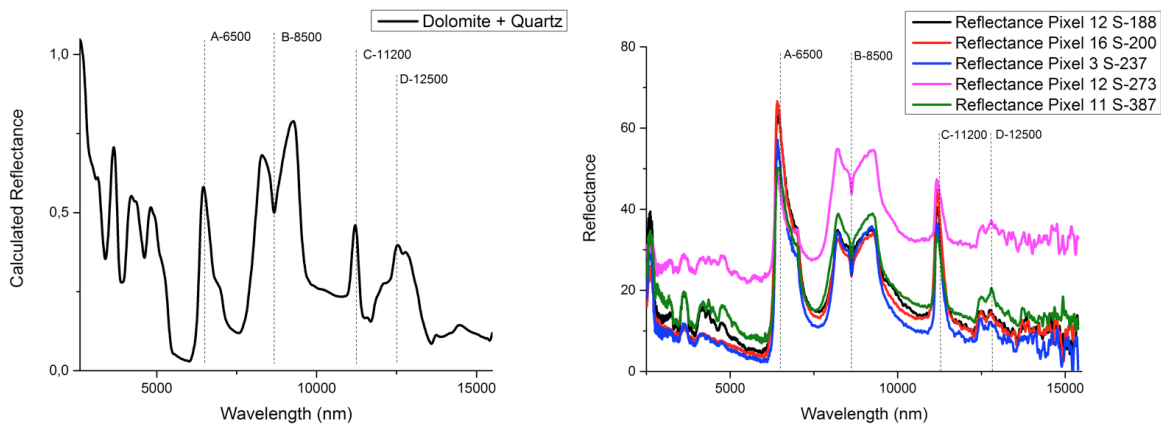
Figure 6.30: Reference Spectrum Through Linear Addition of Mixed Quartz and Dolomite (Clark et al. [19]) and Measured Spectra

A created reference spectrum and measured mixed spectra of dolomite and serpentine is shown in Figure 6.31. The dolomite C-O features can be identified (B and E), whereas serpentine causes features at 3300 *nm* (A) and 9300 *nm* (D). The created spectrum shows to be in good agreement with the measured spectra, with a sharp serpentine feature around 9500 *nm* instead of 9300 *nm* (D). An additional feature is measured at 8200 *nm* (C). QEMSCAN results showed that carrollite was present in these samples as well, potentially causing this feature. It is also possible that the feature forms due to the small grain size of serpentine (between 22 and 32 μm). The grain size can also be an explanation for the shifting of the serpentine feature from 9500 to 9300 *nm*. The presence of dolomite and Mg silicates has been confirmed using QEMSCAN data.
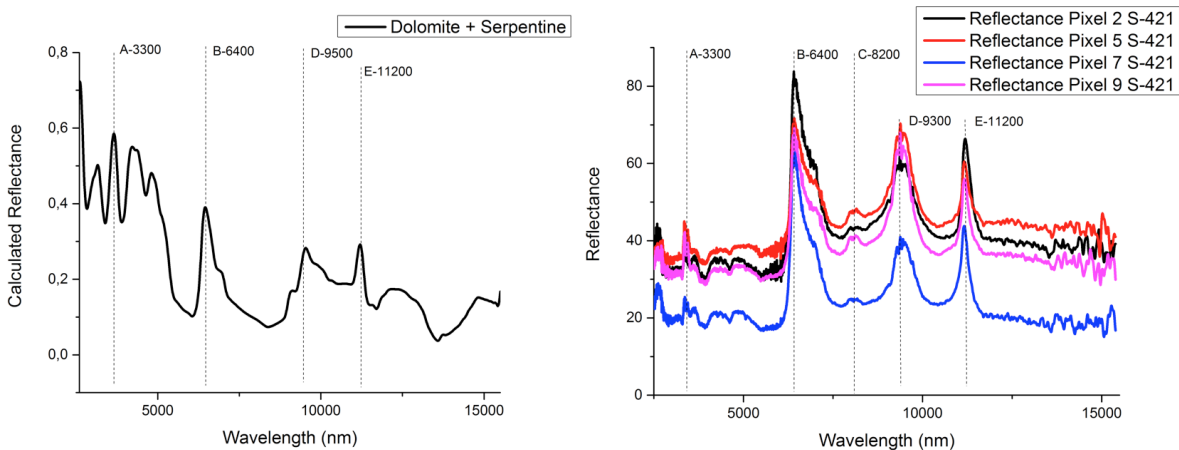
Figure 6.31: Reference Spectrum Created by Linear Addition of Dolomite and Serpentine (Clark et al. [19]) and Measured Spectra

Figure 6.32 shows a created mixed spectrum and measured spectra of quartz, dolomite and serpentine. Serpentine is the most dominant feature, with features at 3300 *nm* (A) and 9400 *nm* (D). The second serpentine feature now is measured at 9400 *nm* instead of 9300 *nm* (Figure 6.31), is it possible that that is due to interaction of the serpentine feature with the quartz feature at 8500 *nm* (C). The position of the first dolomite feature also appears to have shifted to 7100 *nm* (B) instead of 6200 *nm*. The second feature can still be identified at 11200 *nm* (E). Both quartz features can be identified at 8500 *nm* (C) and 12500 *nm* (F). The created reference spectrum shows to be in moderate agreement with the measured spectrum, mainly showing the linear addition of the quartz and serpentine feature. The serpentine peak is stronger in the measured spec-

trum, which could be due to the IR activity of serpentine or differences in mineral proportions. The presence of dolomite, quartz and Mg silicates has been confirmed using QEMSCAN data.
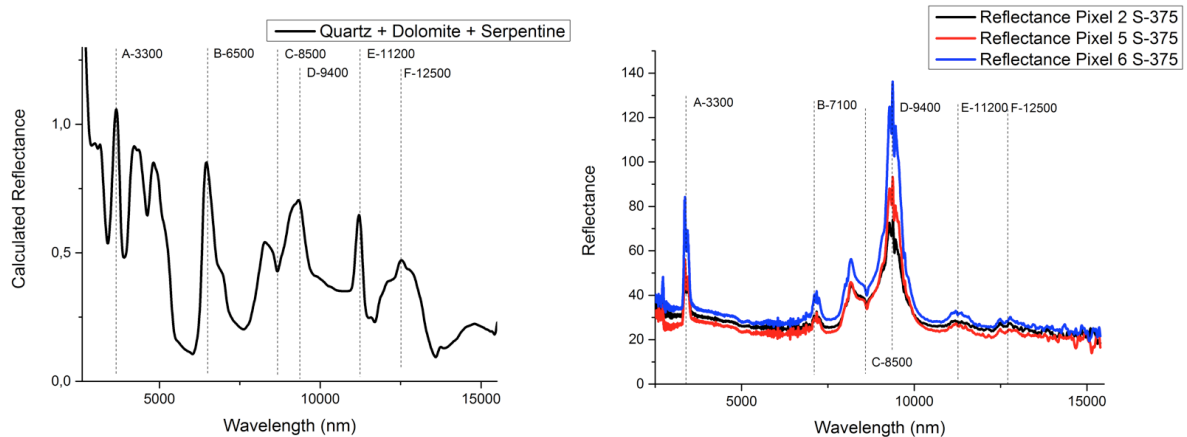
Figure 6.32: Reference Spectrum Created by Linear Addition of Dolomite, Quartz and Serpentine (Clark et al. [19]) and Measured Spectra

A mixture of quartz, dolomite and muscovite is shown in Figure 6.33. Muscovite can be identified by the double feature around 9350 *nm* (C). This feature was not clear when adding the spectra together and thus the reference spectra of quartz and muscovite are shown. The reference spectra indicate that the combination of the quartz and muscovite features around 9300 *nm* could cause the measured feature. The dolomite feature can again be found around 7100 (B) and 11200 *nm* (D) for pixel 4 and 9. The presence of dolomite, quartz and muscovite or illite has been confirmed using QEMSCAN data.
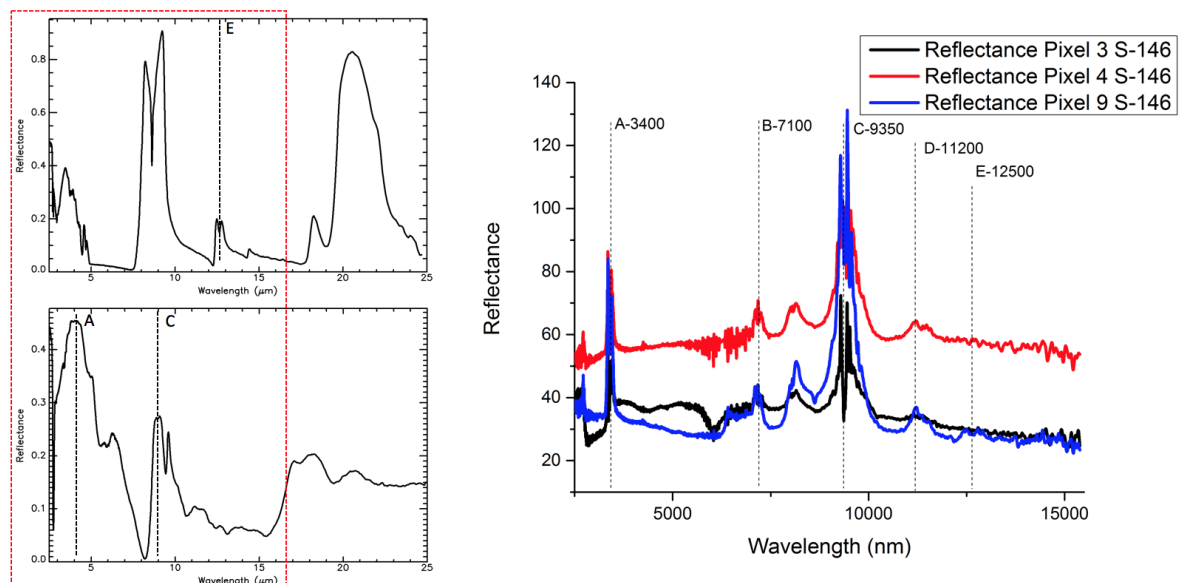
Figure 6.33: Reference Spectrum of Quartz (Top) and Muscovite (Bottom) (Clark et al. [19]) and Measured Mixed Spectra of Quartz, Dolomite and Muscovite

Figure 6.34 shows the measured spectra of a mixture of dolomite, quartz and chlorite. Linear addition of these spectra did not clearly show the influence of the chlorite feature and thus reference spectra of quartz and chlorite are shown. The dolomite features at 6500 *nm* (A) and 11200 *nm* (D) can be clearly identified. The quartz features are found at 8500 *nm* (B) and 12500 *nm* (E). The presence of chlorite appears to cause an additional feature at 9700 *nm* (C), which is likely when considering the reference spectra of chlorite and quartz. The presence of dolomite, quartz and chlorite has been confirmed using QEMSCAN data.
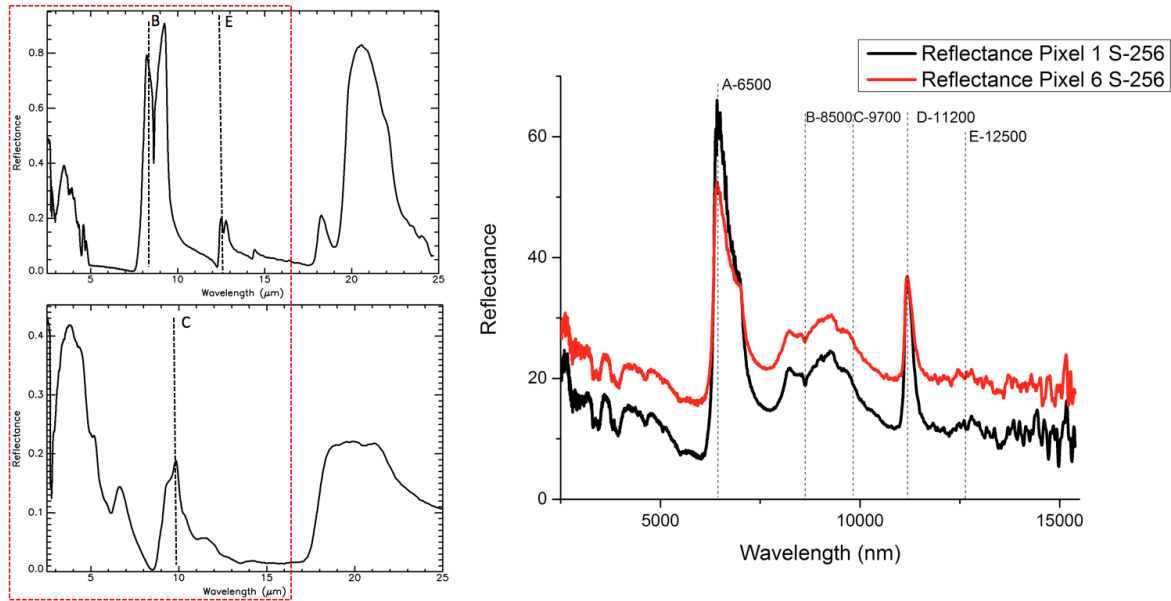
Figure 6.34: Reference Spectrum of Quartz (Top) and Chlorite (Bottom) (Clark et al. [19]) and Measured Spectra

A created mixed spectrum and measured spectra of quartz, illite and K-feldspar are shown in Figure 6.35. All three minerals showed to have features around 8500 *nm* (B). The quartz feature can mainly be identified around 12500 *nm* (D). The features at 8400 *nm* (A) and 9100 (C) are mainly due to a combination of illite and K-feldspar. This can also be seen in the created mixed spectrum, which is in good agreement with the measured spectra. The presence of quartz, K-feldspar and muscovite or illite has been confirmed using QEMSCAN data.
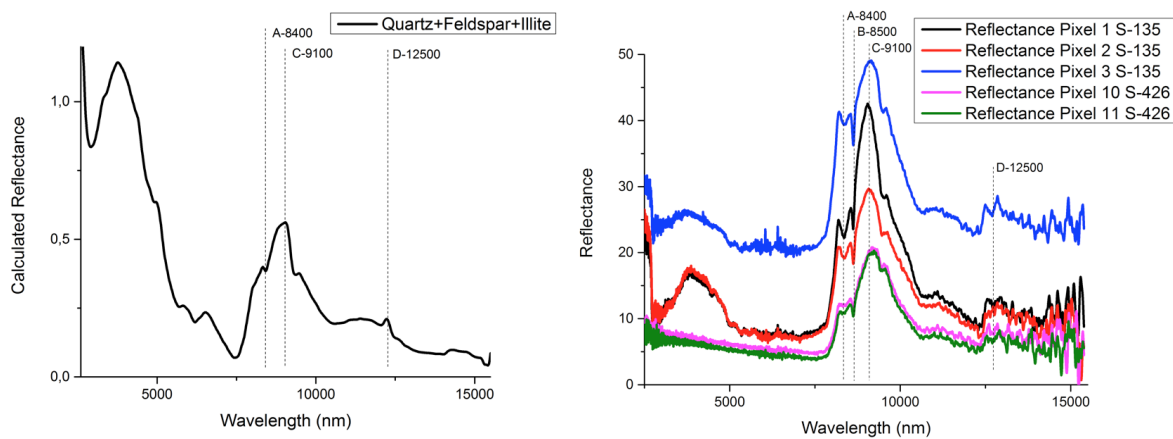
Figure 6.35: Reference Spectrum Created by Linear Addition of Quartz, Illite and Feldspar (Clark et al. [19]) and Measured Spectra

In Figure 6.36 measured spectra containing quartz, talc and chlorite are shown. When adding these spectra, no clear features could be identified and thus the reference spectra of talc and chlorite are shown. The quartz feature can be identified around 8500 *nm* (B) and 12500 *nm* (E). The chlorite features can be identified around 6500 *nm* (A) and 9700 *nm* (D). Compared to the mixture of quartz, dolomite and chlorite (Figure 6.34) an additional feature is found around 9100 *nm* (C). When considering the talc reference spectrum and QEMSCAN data, it is suggested that these measured spectra could be a combination of talc, chlorite and quartz. The presence of quartz, chlorite and Mg silicates has been confirmed using QEMSCAN data.
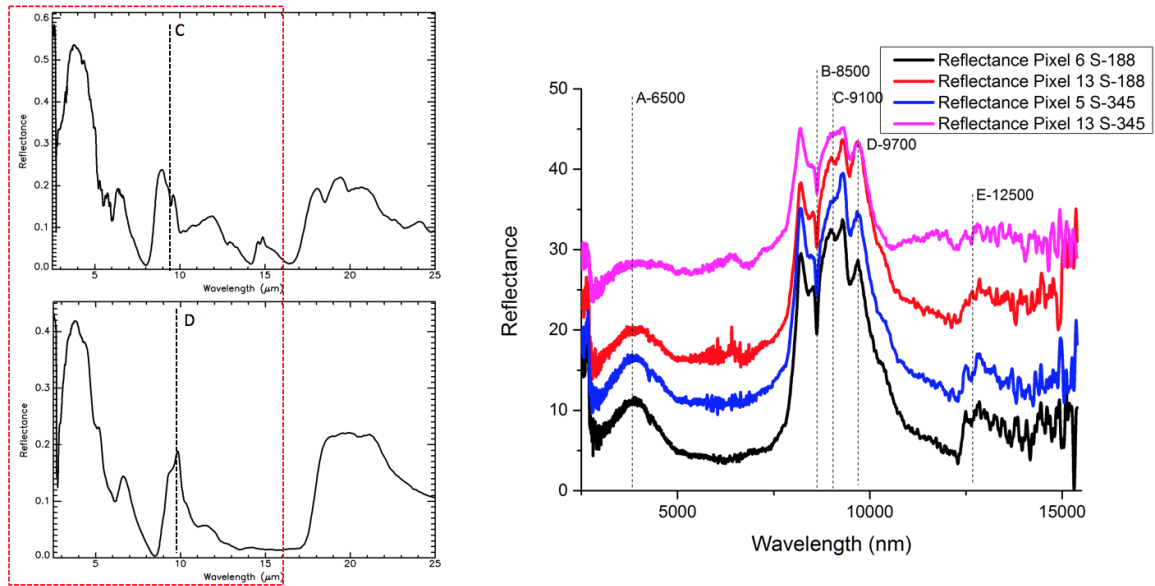
Figure 6.36: Reference Spectrum of Talc (Top) and Chlorite (Bottom) (Clark et al. [19]) and Measured Spectra of Quartz, Talc and Chlorite

Figure 6.37 shows similar features as seen in Figure 6.36, but in addition also dolomite features at 6500 *nm* (A) and 11200 *nm* (E) can be identified. Again, the features of talc and chlorite can be identified at 9100 *nm* (C) and 9700 *nm* (D). Also the quartz features are clear at 8500 and 12500 *nm* (B and F). The presence of dolomite, quartz, chlorite and Mg silicates has been confirmed using QEMSCAN data.
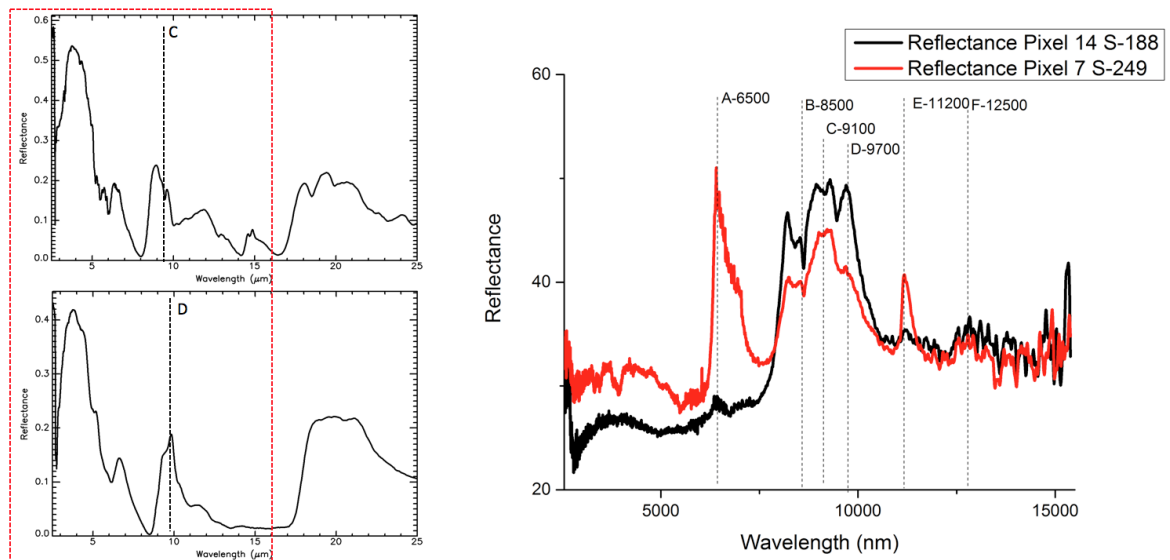
Figure 6.37: Reference Spectrum of Talc and Chlorite (Clark et al. [19]) and Measured Spectra of Quartz, Talc, Chlorite and Dolomite

Figure 6.38 shows the features of the mixed spectra. All these spectra include the dolomite features, but are excluded as the influence of mixing features is found between 7500 and 11000 *nm*. Quartz is added in both plots, as it is present in all the spectra except the serpentine spectrum. The differences between the mixture spectra are clear for the majority of the spectra. It is possible that the quartz/K-feldspar/illite mixture is mistaken for a quartz/chlorite mixture, as the only difference is that the mixture containing illite has a more curved feature.
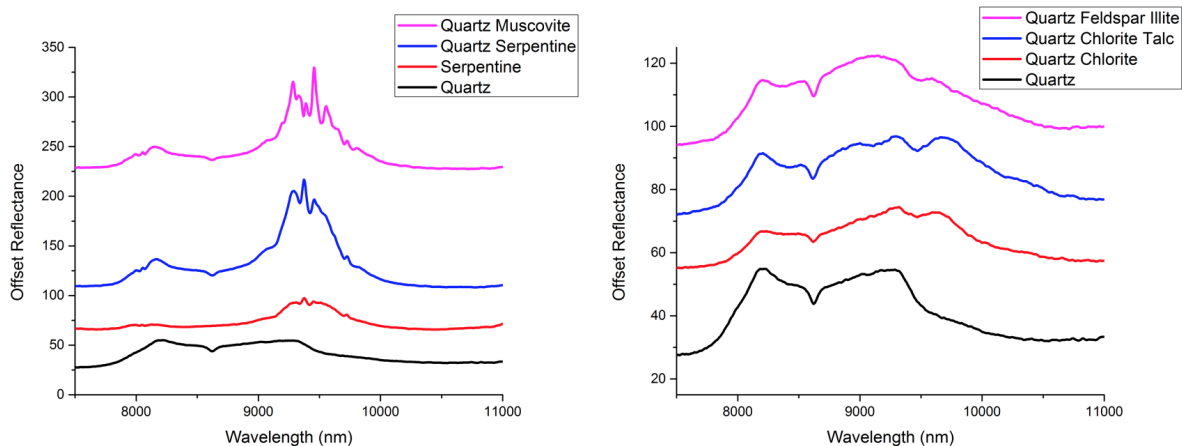
Figure 6.38: Features of Mixed Spectra between 7500 and 11000 *nm*

It has been shown that dolomite, quartz, chlorite, muscovite, illite, talc, serpentine and carrollite can be identified using the FTIR data, either present in a nearly pure form or mixed with other minerals. According to the QEMSCAN data carrollite is present in nearly all the samples, but it could only be identified when no other IR active minerals were present. From a mineralogy perspective, FTIR has been very useful in defining the gangue mineralisation.

6.4.3. Quantitative Mineralogy Through FTIR

The 325 spectra all contain information regarding the mineralogy of the studied samples. As these samples are also analysed using QEMSCAN, it will be possible to compare the differences in the modal mineralogy found using the two different techniques. For each sample between 10 and 16 FTIR spectra are available. The potential pure spectra or mixes have been discussed in the previous section. All 325 spectra were analysed in that way. An example of the workflow shall be given here, analysing the features of six spectra of sample S-256. That is followed by the modal mineralogy of all the samples, which will be compared to the QEMSCAN results.

The spectra measured in pixel 1 and 3 are shown in Figure 6.39. When comparing these spectra to the pure and mixed spectra identified previously, it is possible to identify dolomite, chlorite and quartz features in pixel 1. These three features can also be seen in pixel 3, with the dolomite features being less intense compared to the features seen in pixel 1.
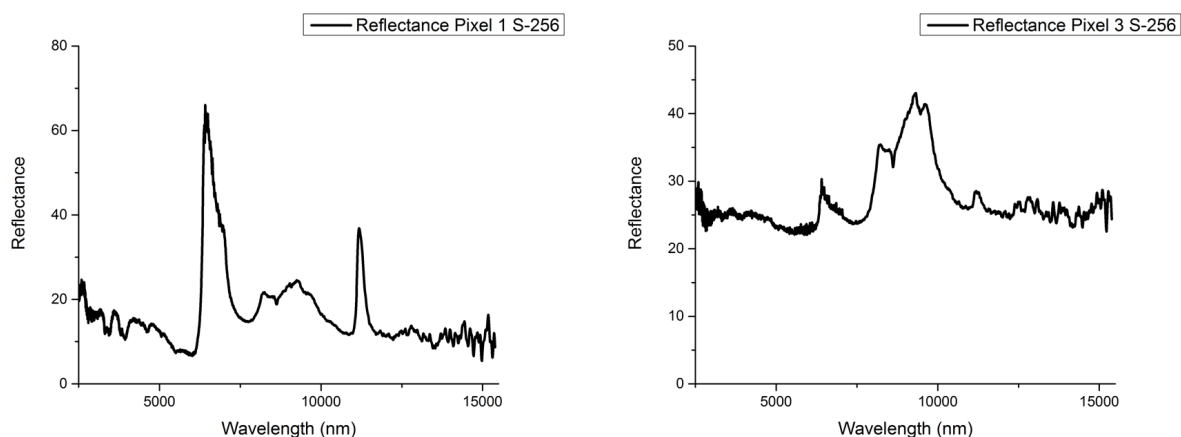
Figure 6.39: Measured FTIR Spectra of Pixel 1 and 3 of S-256

Figure 6.40 shows the measured spectra of pixel 6 and 8. Pixel 6 is similar to pixel 1, containing dolomite, chlorite and quartz. Pixel 8 appears to contain quartz and chlorite features, but no dolomite.
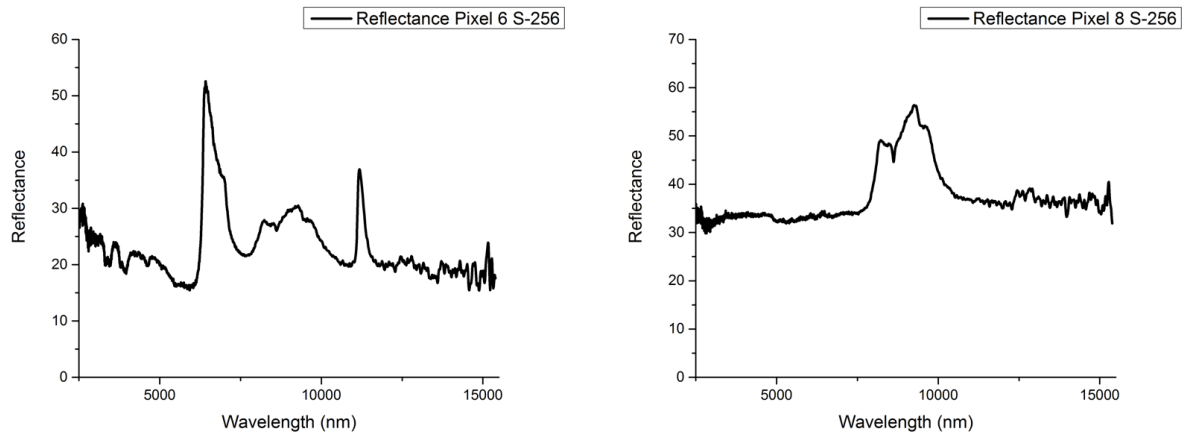
Figure 6.40: Measured FTIR Spectra of Pixel 6 and 8 of S-256

The spectra of pixel 12 and 13 are shown Figure 6.41. Pixel 12 only contains chlorite features and pixel 13 only contains quartz features.
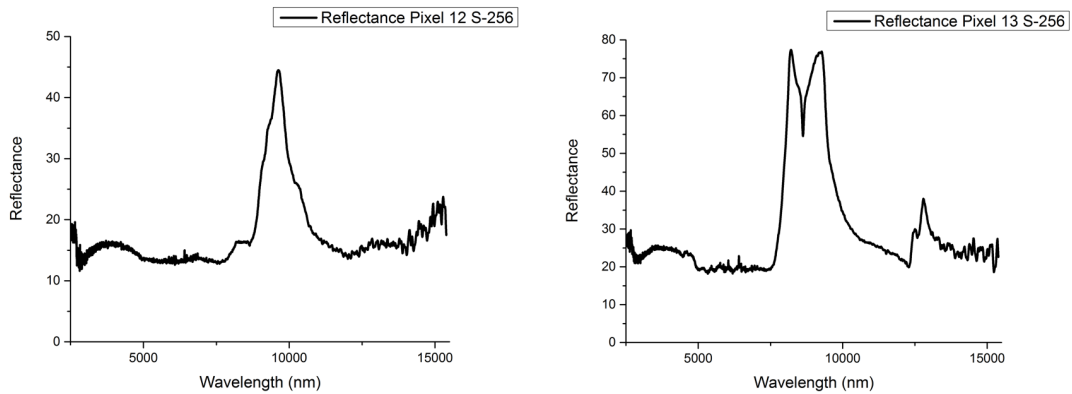
Figure 6.41: Measured FTIR Spectra of Pixel 12 and 13 of S-256

To make it quantitative, the number of times that a spectra has been identified will be divided by the total number of pixels. The result is a relative proportion of each mineral. A more intense feature means that more of that mineral is present (for example dolomite in pixel 1 and 3 (Figure 6.39). At this moment there is no clear method to quantify the differences in contribution and thus shall both pixel 1 and 3 have an equal dolomite contribution according to this method. For the six spectra discussed the modal mineralogy is given in Table 6.7. This has been done for all the samples. These results can be found in Appendix C.

Table 6.7: Minerals Present in the Six FTIR Spectra of S-256

	Quartz	Dolomite	Chlorite
Pixel 1	Yes	Yes	Yes
Pixel 3	Yes	Yes	Yes
Pixel 6	Yes	Yes	Yes
Pixel 8	Yes	No	Yes
Pixel 12	No	No	Yes
Pixel 13	Yes	No	No
Modal Mineralogy	38%	23%	38%

The modal mineralogy found using this pixel approach is shown in Figure 6.42, using the QEMSCAN tex-

ture division. In total eight minerals could be distinguished, whereas the QEMSCAN found fifteen different minerals. The minerals that have not been identified in the IR spectra are chalcopyrite, bornite, chalcocite, Fe-dolomite, apatite, magnesite, biotite and phlogopite. A difference is that through FTIR it has been possible to differentiate between illite or muscovite and talc or serpentine. The differences in modal mineralogy of the mineral textures were discussed in section 6.2.2.
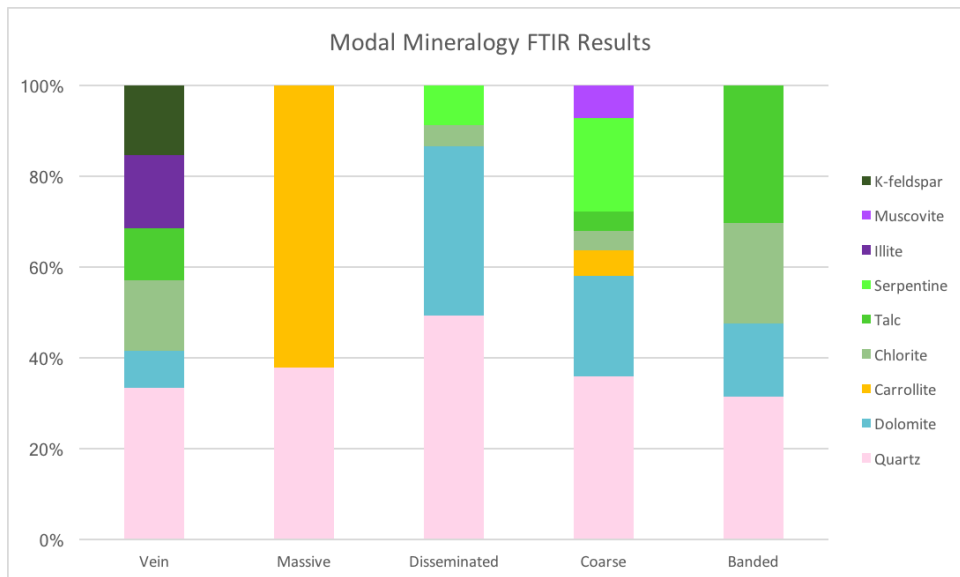
Figure 6.42: Modal Mineralogy of the Distinguished Mineral Textures as Determined using FTIR

Figure 6.43 shows a comparison of the modal mineralogy found through FTIR and QEMSCAN for three texture types. This QEMSCAN data only includes the mineralogy measured using FTIR, as additional minerals would dilute the comparison. Appendix D contains the complete QEMSCAN mineralogy and FTIR mineralogy per sample. As stated before, carrollite could only be measured when no IR active minerals were present, as is the case for the massive texture type. Besides that, the mineral proportions are in good agreement. The FTIR measurement overestimated the illite and quartz volume in all cases. Also, K-feldspar was not measured in the FTIR measurements for the disseminated texture type.
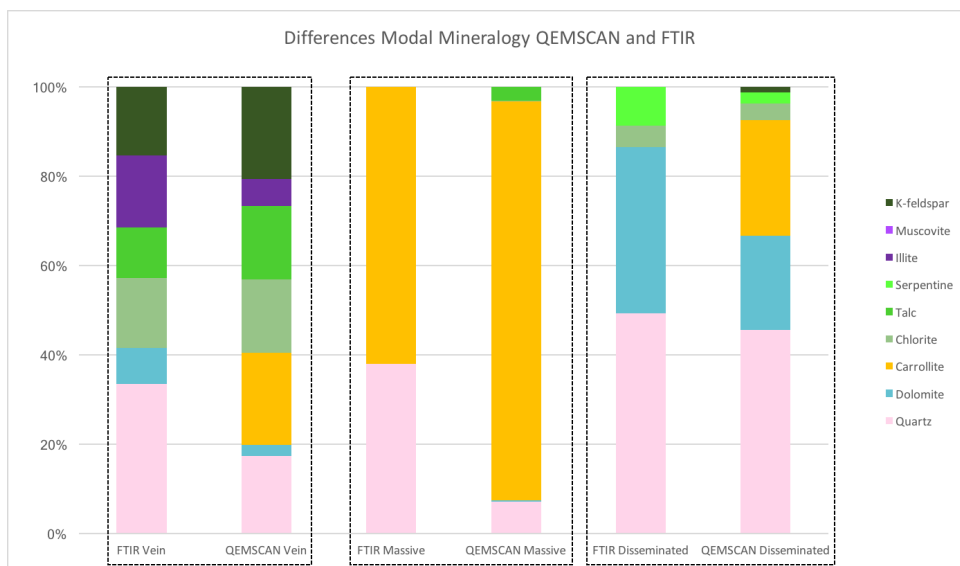
Figure 6.43: Differences in Modal Mineralogy Found Through FTIR and QEMSCAN

The modal mineralogy of FTIR and QEMSCAN data for the remaining two texture types is shown in Fig-

ure 6.44. Carrollite is again not measured or underestimated. One interesting observation is that the FTIR data overestimates serpentine for the coarse texture type, this implies a strong IR activity of serpentine. The banded texture appears to be in good agreement regarding the measured mineral proportions.
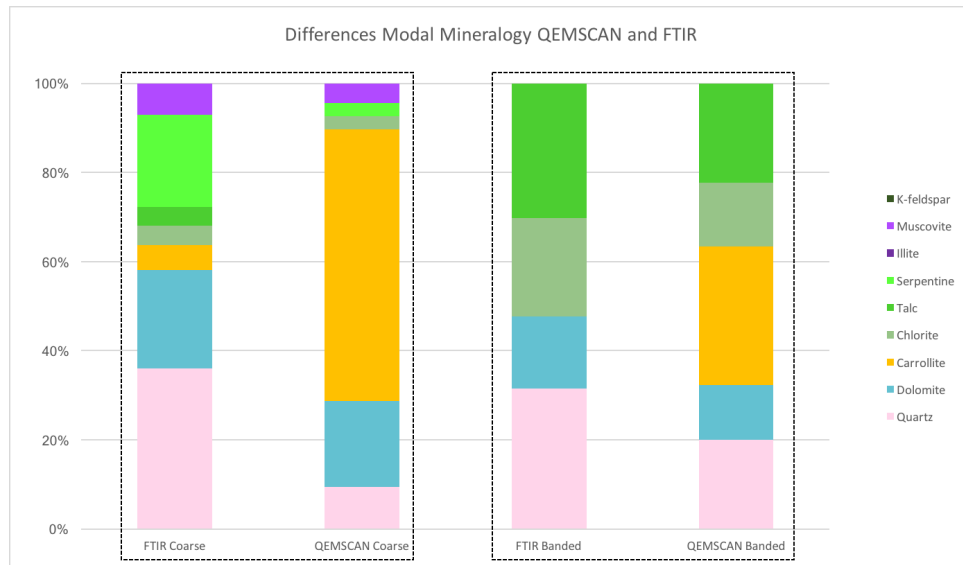
Figure 6.44: Differences in Modal Mineralogy Found Through FTIR and QEMSCAN 2

FTIR has shown to be a good characterisation tool for gangue mineralogy and to be able to detect carrollite if present in large proportions. As it allowed to characterise certain gangue mineralogy in more detail, it also added value to the QEMSCAN work. FTIR cannot be used as a standalone characterisation tool, but will be able to provide relevant mineralogical information. It has to be noted that no mixed reference spectra are available considering the mixing of present minerals and that it is possible that spectra have been misinterpreted.

6.5. CT Scan

In CT scan images a zone with a light-grey colour has a higher density than the zones with a darker colour. The density of the main minerals is shown in Table 6.8, showing that lighter areas will most likely imply the presence of valuable minerals.

Table 6.8: Density of the Main Minerals (Mindat.org [64])

Mineral	Carrollite	Chalcopyrite	Dolomite	Quartz	Magnesiochlorite	Illite
Density (g/cm^3)	4.83	4.20	2.88	2.65	2.60-3.30	2.61

The 3D density visualisation of S-314 is shown in Figure 6.45. The 2D QEMSCAN analysis indicated that at the surface of the core sample a coarse carrollite texture was present, with very little gangue mineralisation. Also in 3D the coarse texture can be identified and only a few pores of lower density gangue mineralisation are present. This sample appears to be one of the pure carrollite nodules that was discussed in section 3.1.3. S-314 is the only sample with these mineralisation characteristics. Even in the same sample bag no other core pieces with comparable mineralisation could be found.
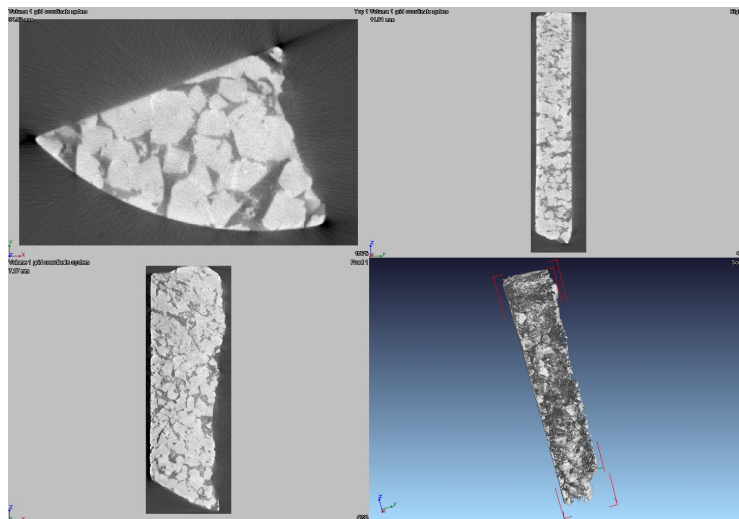
Figure 6.45: 3D View of Density Differences as Measured Using CT Scan of S-314

Variations in density of S-345 in 3D is shown in Figure 6.46. This sample was analysed for the vein like mineralisation that was found using QEMSCAN, as there are several samples with this vein like texture. The combination of thicker and thinner continuous veins are present through the whole host rock. It is difficult to assign one texture type, as both single veins and larger zones of higher density mineralisation are found. The host rock appears to be rather homogeneous. That is from a density perspective, meaning that that statement is incorrect if the host rock and other gangue mineralisation have a similar density.
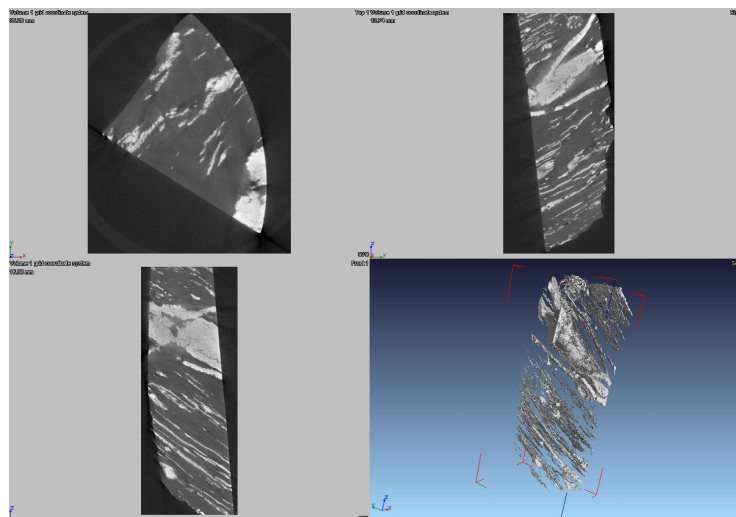
Figure 6.46: 3D View of Density Differences as Measured Using CT Scan of S-345

Figure 6.47 shows the 3D density visualisation of S-426. The QEMSCAN results showed that within this mineralisation veins of carrollite, chalcopyrite and quartz can be found. This vein texture type can clearly be distinguished. As the CT scan shows, within the remainder of the core homogeneous mineralisation can be found. The S-426 was very similar to all the other samples within sample bag B34. The information from this CT scan can thus be used for analysing and interpreting those samples.
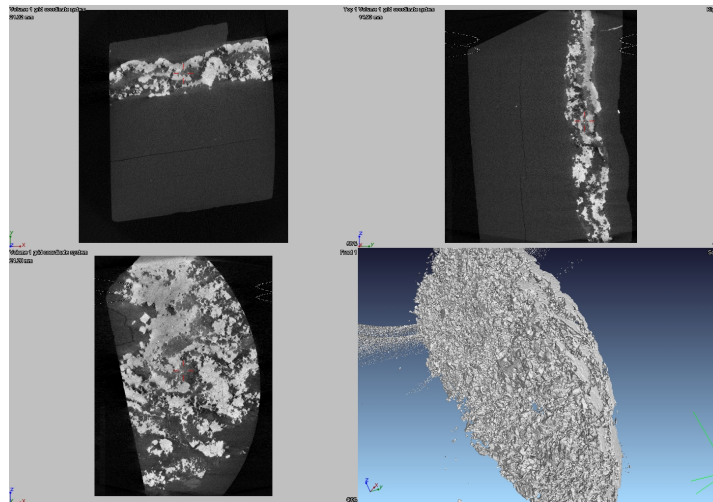
Figure 6.47: 3D View of Density Differences as Measured Using CT Scan of S-426

Overall, the CT scan has proven to be very useful in characterising the samples in three dimensions, in separating gangue from valuable material and by distinguishing two texture types. The set up used at Delft University of Technology studies the sample at maximum resolution, making this a time consuming approach. A resolution-time trade off is required to develop the CT scan into a high throughput geometallurgical tool that allows to identify differences in mineral texture.

6.6. Laboratory Comminution

6.6.1. Sample Selection

Based on the results presented in section 6.2, six different samples are selected for the comminution tests. The samples are selected based on differences in modal mineralogy and mineral texture. That data is known for the core pieces studied using QEMSCAN. It is assumed that different core pieces from the same sample bag have a similar modal mineralogy and mineral texture as the studied core pieces. The selected sample bags are B18, B23, B26, B29, B33 and B34. The assumed modal mineralogy and texture types for these sample bags are shown in Figure 6.48. B18 and B34 (vein) and B23 and B29 (banded) have the same texture type. The main difference is that B29 contains very little dolomite.
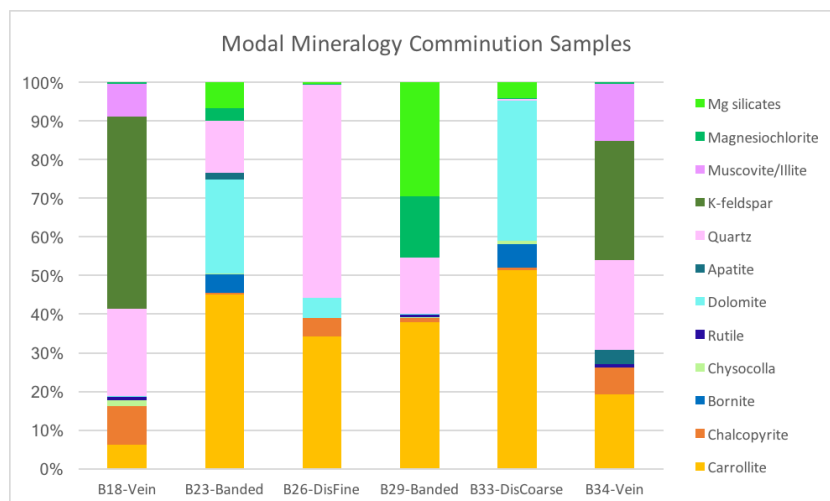
Figure 6.48: Modal Mineralogy of the Samples Selected for Comminution

In Table 6.9 the adjusted Leeb Hardness and average carrollite grain size of the samples that are selected

for the comminution tests are shown. This is the summarised surface hardness data, the complete table with sample mass and adjustment factor can be found in Appendix E. The surface hardness of B29 is greater than the surface hardness of B23, whilst having the same texture. B26 and B29 have a similar surface hardness, but are different texture types. The surface hardness of B34 is significantly lower than the surface hardness of B18. The differences allow for an analysis of the impact of the surface hardness on comminution properties.

Table 6.9: Overview of Texture Type, Surface Hardness and Average Carrollite Grain Size of Samples Selected for Comminution

Sample	Texture	Adjusted Leeb (*LH)*	Average Carrollite Grain Size (μm)
B18	Vein	614	175
B23	Banded	686	361
B26	Disseminated Fine	844	366
B29	Banded	830	300
B33	Disseminated Coarse	590	256
B34	Vein	523	412

6.6.2. Crushing Results

The results of a comminution test are visualised by a Particle Size Distribution (PSD). The PSD of the six different sample sets after the crushing process are shown in Figure 6.49. The more that a curve is shifted to the left, the finer the particles within the distribution are.
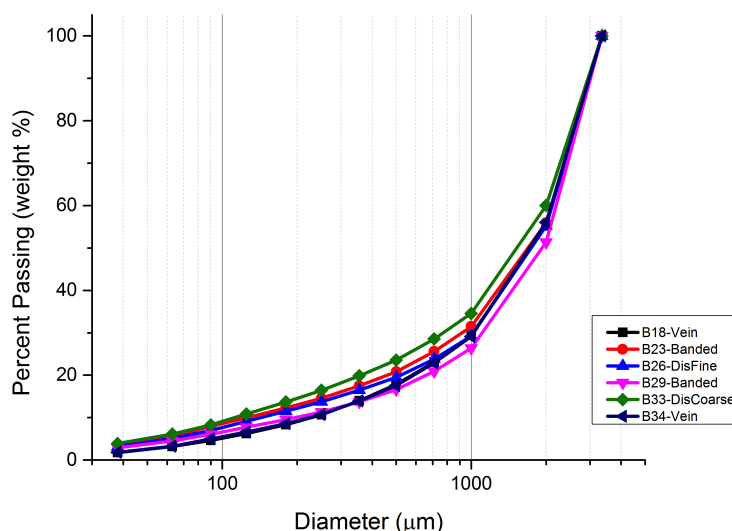
Figure 6.49: Particle Size Distribution of Samples Crushed ≤ 3.35 *mm*

There are differences in the PSDs of the crushed samples. An interesting observation it that the PSD of B18 and B34 is nearly equal whilst having the same texture. B23 and B26 appear to have a similar PSD, whilst both having a different texture. The coarse disseminated texture type (B33) appears to be the most affected by the crushing, as the PSD curve is shifted the furthest to the left.

There are several parameters that can be used to quantitatively assess the impact of the crushing operation. A parameter of interest is p_{80}, which is defined as the product particle diameter of which 80% of the particles have a smaller diameter. This is often combined with f_{80}, which represents the feed particle diameter of which 80% of the feed particles are smaller. The overall reduction (R) is found by dividing f_{80} by p_{80}:

$$R = \frac{f_{80}}{p_{80}} \tag{6.2}$$

These three parameters are shown in Table 6.10. For f_{80} the diameter of the drill core has been used.

Table 6.10: Comminution Parameters of Samples Crushed ≤ 3.35 *mm*

	MM18 Vein	**MM23** Banded	**MM26** Disseminated	**MM29** Banded	**MM33** Coarse	**MM34** Vein
F80(μm)	20750	31000	32000	18300	25500	246700
P80(μm)	2747	2737	2747	2795	2675	2736
R	7.55	11.33	11.65	6.55	9.53	9.02

It is interesting to see that the p_{80} is the same order of magnitude for all the samples, varying from a minimum of 2675 μm to a maximum of 2795 μm. Besides that, B18 and B26 have an identical p_{80} and also B23 and B34 have nearly identical values. The *R* varies, which can be explained by the differences in drill core diameters of the feed.

The cobalt recovery per size fraction can be calculated using the following equation:

$$R_{Co} = \frac{Co(\%)_{sample} \cdot (wt.\%)}{Co(\%)_{Feed}}$$ (6.3)

With R_{Co} being the cobalt recovery (between 0 and 1), $Co(\%)_{sample}$ the cobalt grade of the size fraction, wt.% the weight present of the size fraction and $Co(\%)_{Feed}$ the cobalt grade of the feed. The cumulative cobalt recovery for all samples is shown in Figure 6.50. For all the samples the majority of the cobalt is present in the coarse size fractions, from 1000 μm onwards.
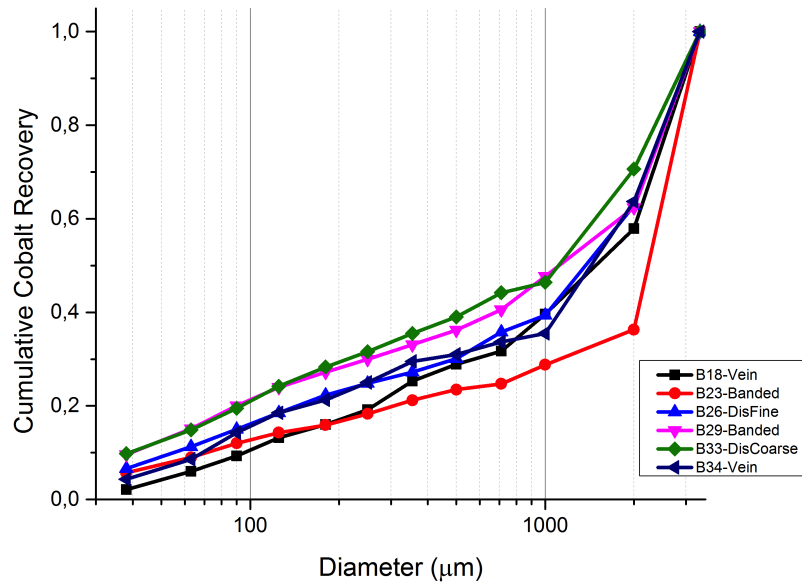
Figure 6.50: Cumulative Cobalt Recovery per Size Fraction for Crushed Samples

There is an important limitation that needs to be understood when considering the crusher results. The goal was to get the diameter of all fragments below 3.35 *mm* and the samples are crushed numerous times until that diameter is reached. This means that the samples have not necessarily been treated in the same manner, as some samples have been crushed more times than other samples. Even though the crushing results are interesting, the main conclusions need to be drawn from the grinding results.

6.6.3. Grinding Results

The PSDs of the samples after 21 minutes of grinding are shown in Figure 6.51 and is interpreted in the same way as the crushed PSD, with trends to the left having a finer particle size distribution. B23 and B29 have a very similar trend, whereas B23 has a larger number of fines and a smaller number of larger diameter particles. B18 and B34 also follow a similar trend, and so do B26 and B33. The disseminated textures are affected the most, followed by the vein texture type and the banded texture type the least.
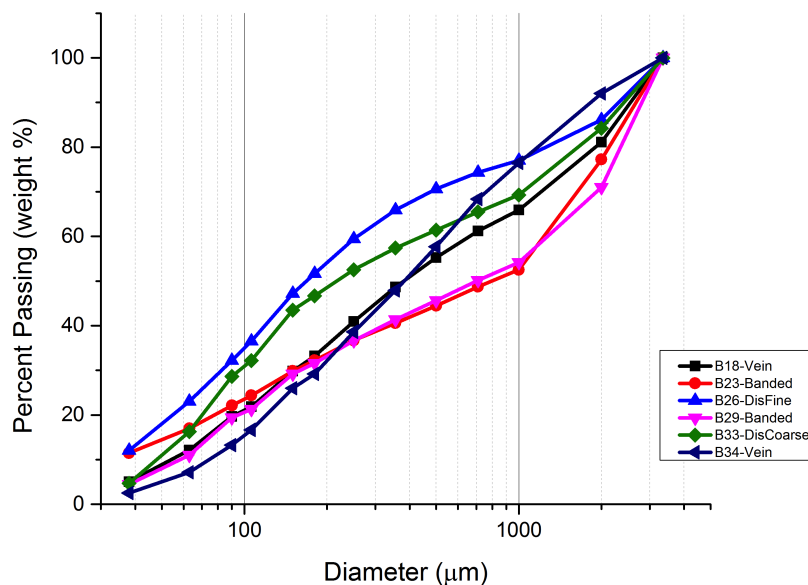
Figure 6.51: Particle Size Distribution of the Samples Ground for 21 Minutes

The f_{80}, p_{80} and R values for the grinding process are summarised in Table 6.11. There are large differences between the p_{80} of the samples, with B29 having the coarsest (2418 μm) and B34 having the finest (1226 μm) p_{80}. This influences the R value, that varies between 1.16 and 2.23 for the six samples. When linking the PSD to the modal mineralogy, it is interesting to see that the samples containing two large proportions of a mineral type (B26 has carrollite and quartz, B33 carrollite and dolomite) have a finer PSD. This could be an indication that samples with a more complex mineralogy (B23 and B29, both banded texture) are more resistant to a comminution process.

Table 6.11: Comminution Parameters of Samples Ground for 21 Minutes

	B18	**B23**	**B26**	**B29**	**B33**	**B34**
	Vein	Banded	Disseminated Fine	Banded	Disseminated Coarse	Vein
F80(μm)	2747	2737	2747	2795	2675	2736
P80(μm)	1927	2164	1327	2418	1716	1226
R	1.43	1.26	2.07	1.16	1.56	2.23

For the samples with the same mineral texture, the crushed p_{80} was quite similar whilst the p_{80} of the ground ore is very different. It appears that the Leeb Hardness can be related to the size reduction sensitivity to a grinding process for identical textures. For both the banded (B23 and B29) and the vein (B18 and B34) texture type, the samples with a higher surface hardness have a coarser PSD.

The Co grade per size fraction is shown in Figure 6.52. In the smaller size fraction a higher cobalt grade can be found. Carrollite has the largest grain sizes, but the cobalt is still found in the smallest size fractions after comminution. The reason for that is that small grains are removed from the larger carrollite grains during the grinding process, leading to a higher cobalt grade within the fines.
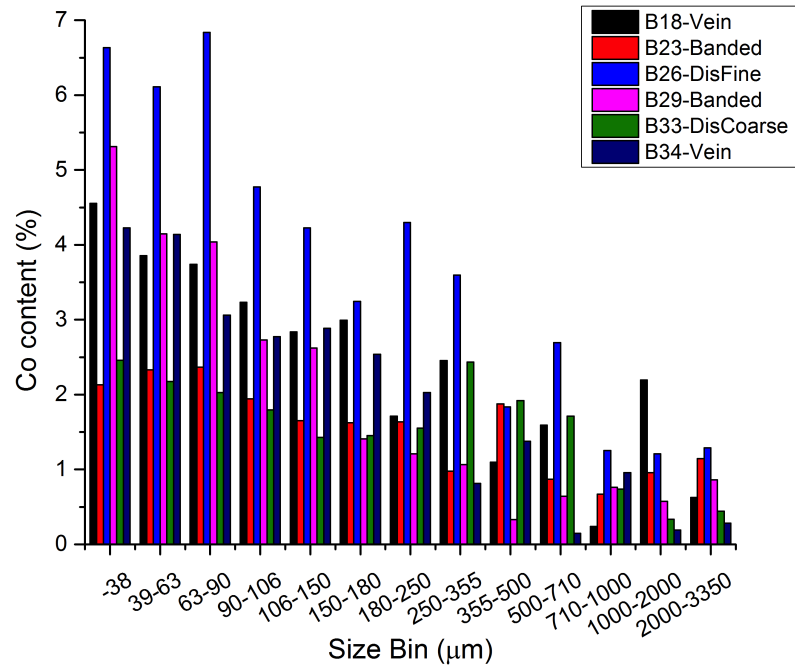
Figure 6.52: Co (%) per Size Fraction for Ground Samples

The cumulative cobalt recovery for the ground samples is shown in Figure 6.53. When comparing this with Figure 6.50, the cobalt has progressed more towards the fines for all samples. B23 still has a large fraction of the cobalt in the coarser ore samples. B29 also has a higher cobalt recovery for the coarser fraction, but the recovery for the finer fractions is similar to the other samples.
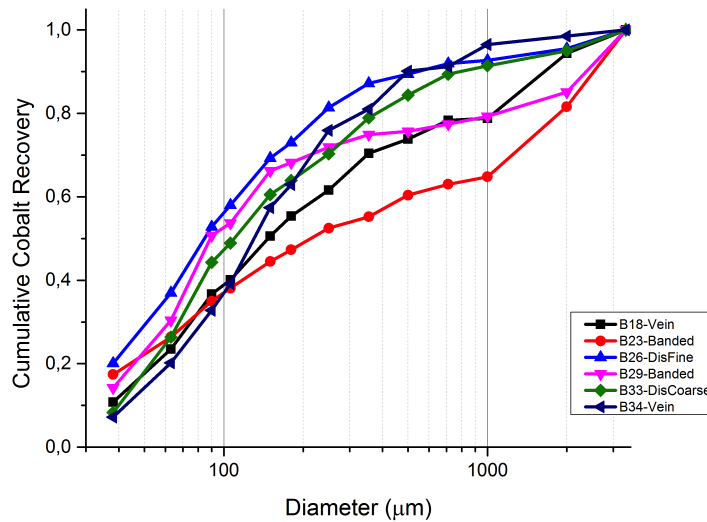
Figure 6.53: Cumulative Cobalt Recovery per Size Fraction for Ground Samples

Histograms of the cobalt recovery comparing the crushing and grinding step are shown in Figure 6.54, 6.55 and 6.56. It is interesting to see that B23 and B29 both have a larger amount of cobalt in the coarsest fraction, more than the other samples. B18 and B34 are quite comparable, but B18 has a high cobalt recovery in the second coarsest fraction. B26 and B33 show a comparable trend for the cobalt recovery, which is increasing towards the finer fractions. This transition of cobalt from the coarser to the finer particles during the grinding process, potentially confirms the brittleness statement that was made when measuring the surface hardness of a large carrollite area in section 6.3.3.
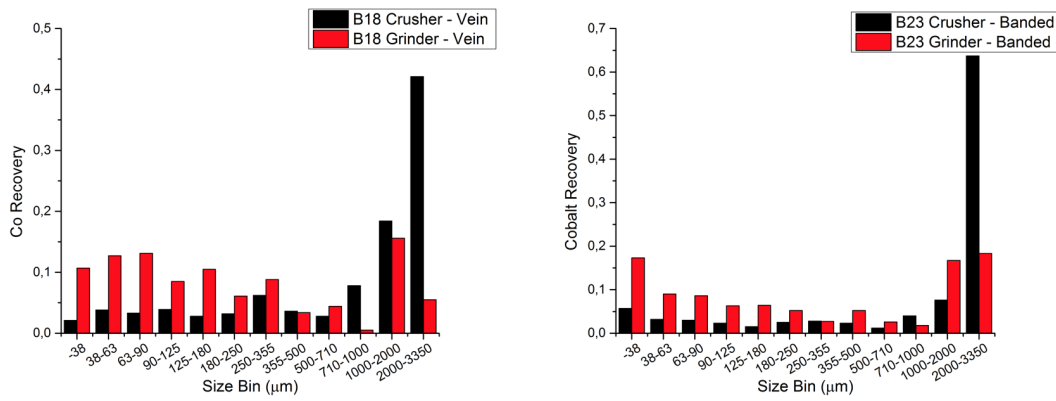
Figure 6.54: Cobalt Recovery Histogram of Crushed and Ground Ore of B18 and B23
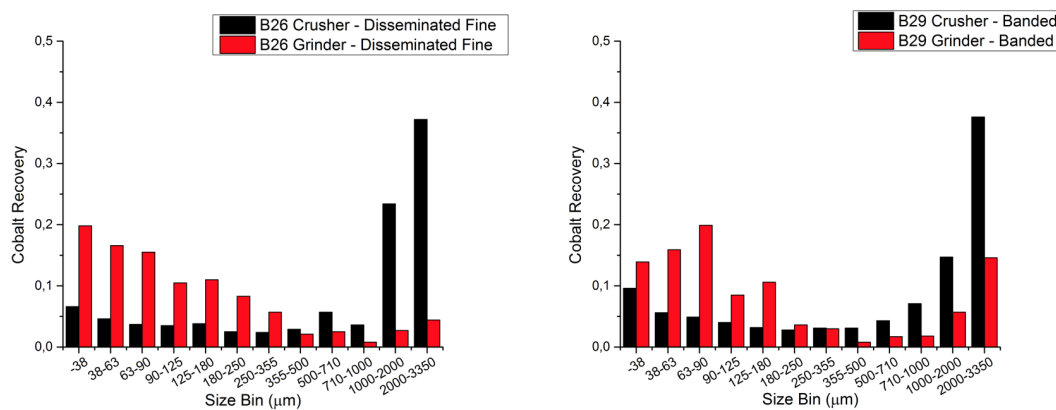
Figure 6.55: Cobalt Recovery Histogram of Crushed and Ground Ore of B26 and B29
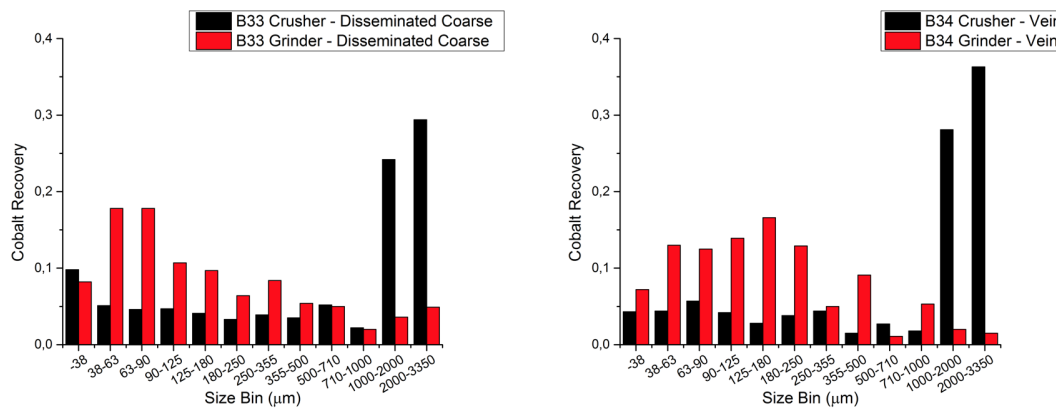
Figure 6.56: Cobalt Recovery Histogram of Crushed and Ground Ore of B33 and B34

The response of the ore to the grinding process was evaluated by considering the retaining mass in a 106 μm sieve every three minutes. The outcome is shown in Figure 6.57. This graph represents the sensitivity of the ore to the grinding process, as per time step the increase in mass of fines can be identified. The steeper the trend, the larger the increase of fines per grinding time step. It appears that the response can be divided into three different groups.

The response of B18 and B34 is initially different, but converges towards the same values. Both are classified as a vein texture. B23 and B29 show to have a similar trend, with a constant offset in the amount of fines

present. B26 and B33 appear to have an identical response to the grinding process, where the lines converge after twelve minutes of grinding and continue to have a similar trend. Additional grinding time is required to study the continuation of the trends. This is a parameter that can be used in geometallurgical domaining, as it shows a difference in grind-ability for different ore samples.
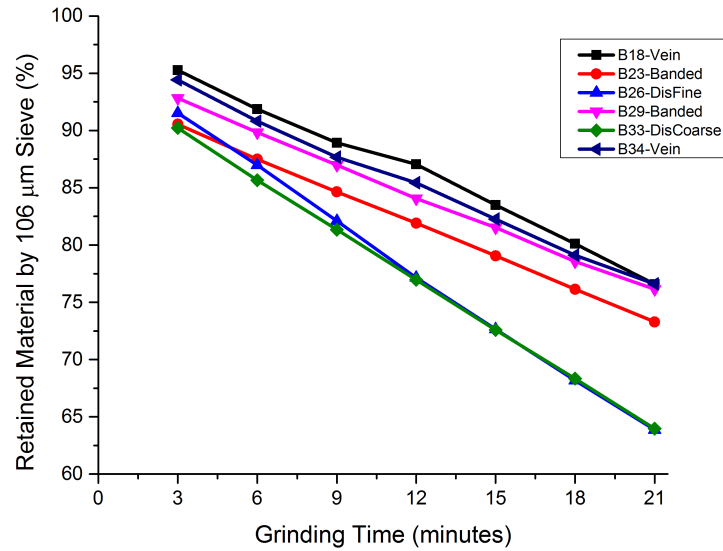
Figure 6.57: Mass Fraction Retained by 106 μm Sieve per Three Minutes of Grinding

The slopes of the trends are shown in Table 6.12, confirming the division based on Figure 6.57. This value needs to be interpreted as the increase in percentage of ore with a size below 106 μm per minute of grinding.

Table 6.12: Slope of 106 μmm Mass Percentage Retained Trends

Sample	B18 - Vein	B23-Banded	B26-DisFine	B29-Banded	B33-DisCoarse	B34-Vein
106 μm slope	-1.06	-0.96	-1.52	-0.92	-1.44	-1.00

A relationship between the cobalt transition from the coarse fraction to the fines fraction and the surface hardness was studied, but no trend could be identified. The results have shown a difference in the response of different mineral textures to the comminution process. The responses cannot quantitatively be linked to measured parameters such as the Leeb Hardness or mineral texture. Performing comminution experiments is thus still an essential part of quantifying the differences between the geometallurgical zones in a geometallurgical model. The Leeb Hardness - mill p_{80} relationship for mineral textures needs further verification by performing the same experiment on more samples.

6.6.4. Comminution Classes

Based on the experiments a geometallurgical division can be made when applying the comminution properties of the six samples to the complete sample set. The division is as follows, with class 1 being the most resistant to comminution and class 3 the least.

1. Comminution Class 1 - Banded Texture Type

2. Comminution Class 2 - Vein Texture Type

3. Comminution Class 3 - Disseminated Texture Type

This is based on the following assumptions:

- Mineral texture is the main factor influencing comminution behaviour of the ore.

- Resistance to comminution can be quantified by the slopes of the comminution trends of Figure 6.57.

This division is based only on six experiments. To confirm the class division additional comminution experiments are required, considering all the different sample bags. This will provide additional data about the influence of texture and surface hardness on the comminution properties.

6.6.5. Evaluation of Characterisation Methods Influencing Comminution Properties

It has been concluded that the mineral texture is the main factor influencing the behaviour of the ore in a comminution process. According to that statement, only the CT scan and QEMSCAN are characterisation methods that can be used to classify to which comminution class a sample belongs. The CT scan and QEMSCAN both have two main disadvantages: the methods are time consuming and require an experienced operator. The Equotip has shown potential in determining how coarse or fine a PSD can be within a texture class, but that potential requires validation.

The data gathered using portable XRF and FTIR spectroscopy cannot directly be linked to the comminution properties. The comminution phase is the first step in mineral processing and normally followed by several other steps. Both portable XRF and FTIR spectroscopy have potential in providing information that can be used for the processes following the comminution phase. Considering that at this moment Mutanda Mining uses only the Co and Cu grade in the resource model, the gangue elements found through portable XRF provide a whole new insight in elemental variation throughout the deposit.

FTIR spectroscopy takes it a step further, as it allows for determining how the gangue mineralogy varies throughout the deposit. For the current operation, FTIR characterisation can provide data about what zones will influence the leaching process, as samples containing dolomite can easily be identified. For the future processing plant, it can provide information regarding the gangue minerals that can be expected in the flotation process and help the operators decide whether different flotation chemicals are required. Portable XRF and FTIR spectroscopy are geometallurgical tools that are easy to use, easy to interpret and have a high data throughput. Unfortunately the tools could not be used for defining the classes required in this thesis, as no textural information is obtained, but the potential for the following processing steps is there.

6.7. Simulated Crushing

6.7.1. Comminution Class Simulation Input

Bruno gives pre determined values of crush-ability and abrasiveness for a range of minerals, including quartz and dolomite. These values are combined with the quartz and dolomite content of the samples determined using QEMSCAN to interpolate a value for the abrasiveness and crush-ability. The results are shown in Table 6.13. These values are also directly the input values for the simulations. The moisture and gravel content are set to zero.

Table 6.13: Simulation Input for Different Comminution Classes

Stream	Density	Crush-ability	Abrasiveness
Class 1	2.82	42.2	342
Class 2	3.50	55.1	1271
Class 3	3.70	62.4	1788

6.7.2. Simulation Results

The results for all the different crushers when processing a feed pre-defined by Bruno are shown in Table 6.14. The table consists of the mass percentage that goes to the undersize pile, the mass percentage that goes to the oversize pile, the number of crushing units and sieves, and the energy consumption as calculated by Bruno.

A set up with Crusher type WF100, G1012 or Barmac VI consumes the least energy, as Bruno did not provide any energy consumption data for these crushers. The selection of an appropriate crusher is made on the trade off between energy consumption, the number of units and the undersize percentage. Based on those

three criteria, the GP 100 has the best overall performance and is thus selected for quantifying differences in energy requirements for the comminution classes.

Table 6.14: Simulated Performance of Different Crushers in Bruno

Crusher	Undersize (%)	Oversize (%)	Number of Units	Energy Usage (*kWh/t*)	Comments
Jaw	36	64	5	11.39	Same set up as in lab tests
GP 100	100	0	2	6.56	
WF 100	99	1	2	0.56	WF100 consumes no energy
G1012	100	0	2	0.57	G1012 consumes no energy
HP100	95	5	4	16.07	
HIS	99	1	4	7.82	
HIS Obsolete	94	6	3	4.45	
Barmac	86	14	5	4.79	
Barmac VI	66	34	5	1.47	VI consumes no energy

The simulated flowsheet of the jaw crusher set up that was used in the laboratory crushing experiments is shown in Figure 6.58. The limitation of this set up is clear: five jaw crushers put in series produce a maximum undersize of 36%. This performance cannot be improved, as the final two sieves contribute negligible material to the undersize pile (indicated by the thin orange stream). It can be concluded that a jaw crusher alone is not suitable for crushing ore below 3.35 *mm* on an industrial scale.
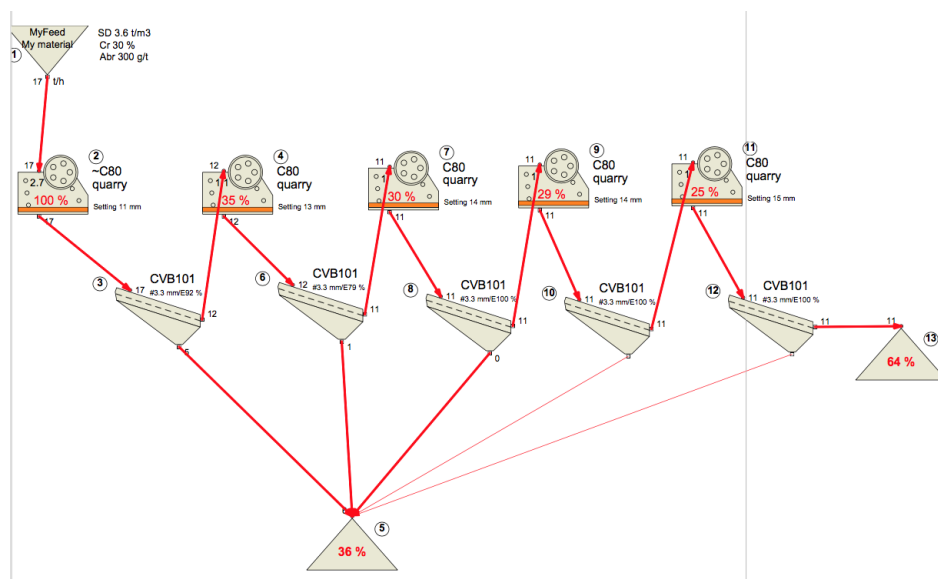
Figure 6.58: Jaw Crusher Set Up in Bruno

The optimal flowsheet using crusher GP100 is shown in Figure 6.59. The improvement compared to the jaw crusher set up in Figure 6.58 is significant, as 100% of the feed goes to the undersize product pile whilst only using two crushing and sieving stages. This crusher set up is used to quantify the energy consumption for the different geometallurgical classes.
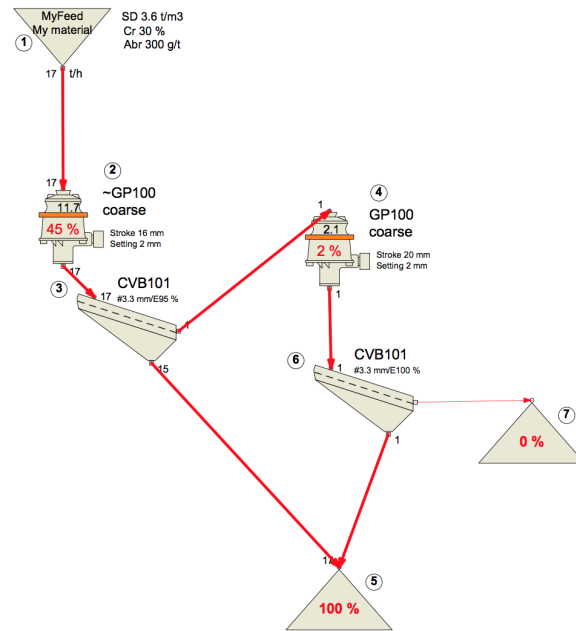
Figure 6.59: Optimum Crushing Set Up in Bruno

The simulated PSDs for class 1, 2 and 3 are shown in Figure 6.60. Class 1 is the most resistant to the crushing process, whereas class 2 is in the middle and class 3 is the most affected. This result is comparable to the differences found using experiments, where the PSD of the samples from class 1 were shifted the most to the right and class 3 the furthest to the left.
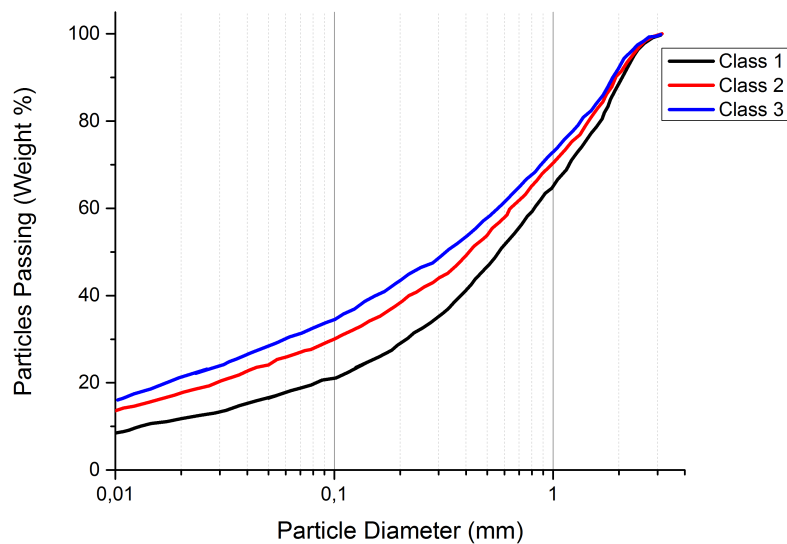
Figure 6.60: Particle Size Distribution of the Three Different Simulated Streams

Table 6.15 shows the energy consumption of the designed circuit for the three different feed streams. Only for class 1 stream a single crusher is sufficient, the other streams all require two crushing units. The most interesting data is the difference in energy consumption. Similar to the PSD position, class 1 requires the most energy, about 27% more than class 3. Class 2 requires more energy than class 3, but less than class 1.

Table 6.15: Simulated Performance of Different Input Streams

Stream	Undersize (%)	Number of Crushers	Capacity Used (%)	Energy Consumption (*kWh/t*)
Class 1	100	1	34	5.32
Class 2	100	2	35	5.00
Class 3	100	2	57	4.20

Figure 6.61 shows the difference between the simulated and experimentally obtained PSD for class 1. There is a large difference between the two PSDs, as the simulated PSD is shifted more to the left and thus is finer. That is also the case for class 2 and 3, the PSDs can be found in Appendix F. When comparing the differences it can be noted that the differences are similar for all three simulations and experiments. This means that the calculated energy requirements should not be used as exact numbers, but can be used for comparative ends.
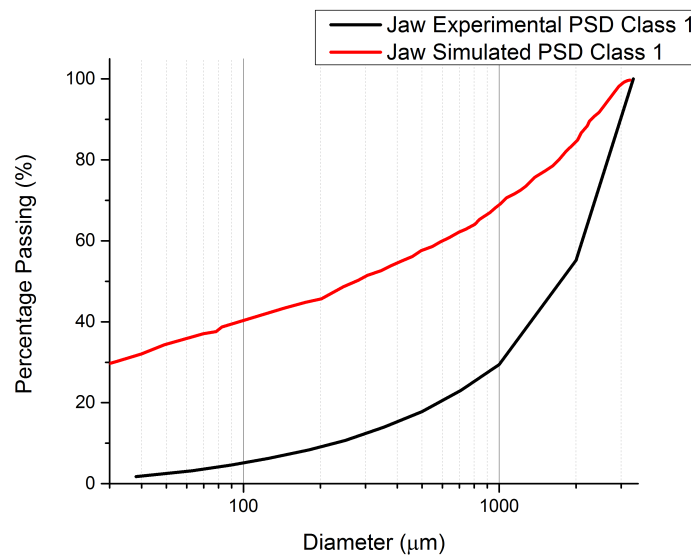
Figure 6.61: Experimental vs. Simulated Crusher PSD for Comminution Class 1

The differences could be caused by:

1. Incorrect simulation input settings. The mineralogy is more complex and is influenced by harder materials (e.g. bornite, chalcopyrite and carrollite).

2. Large difference in throughput. The laboratory experiments used between 220 and 360 grams, the simulations assumed a steady state of 16 tons per hour. Material present in the crusher is required for an optimum crushing step, explaining the much larger volume of fines.

3. Differences in equipment set up. It is possible that the simulated crusher had a much smaller gape than the experimental crusher. Both were set at the minimum gape.

It has been considered to alter the experimental PSDs using empirically defined scale up equations. For this type of crusher, no scale up relationship could be found that was simple enough to rely solely on the knowledge that was gathered during the laboratory experiments.

Using simulation techniques an attempt has been made to study the differences between the energy requirements of different ore types in a crushing circuit. The used approach has limitations, but it is assumed that the inter-sample differences are similar both in the laboratory and simulation respectively. The simulated results can be used as an indication for the energy requirements of different ore types, but should not be presented as deterministic results.

7

Conclusions and Recommendations

Based on the analyses and results that were presented and discussed in the previous chapters, it is possible to draw a set of conclusions and recommendations.

7.1. Conclusions

The portable XRF showed a large variation in cobalt content, ranging from 0% to 22.5% for the sulphide samples and from 0 to 34% for the weathered samples. Also, variation in polluting elements such as K, Mg, Al, Fe and Ca has been identified. Using the QEMSCAN a clear division could be made between the weathered zone and the sulphide zone, as both zones are very different in mineralogy. In the weathered zone five different texture types could be distinguished and both heterogenite and kolwezite could be identified as cobalt carrying minerals. In the sulphide zone six different texture types were present and carrollite was identified as the only cobalt containing mineral. Using the QEMSCAN, variability in mineral associations and average grain sizes was assessed for the sulphide zone. The CT scan images showed that the valuable mineralisation found using QEMSCAN is continuous in 3D, but it was not possible to distinguish between the different types of valuable mineralisation due to small density differences. Variation in the textural properties could be identified using both QEMSCAN and CT scan.

For the Equotip a calibration method has been developed, as it was shown that below a certain threshold mass the measured surface hardness decreases with mass. The calibration allowed to compare samples whilst having a normalised mass. After this calibration, it was possible to identify zones of different surface hardness, which varied for different mineral textures. On a more detailed scale, the Equotip could be used to study the impact of different gangue mineralogy on the surface hardness. Within a sample, areas with a mix of carrollite and quartz had a higher surface hardness than an area with a mix of carrollite and Mg silicates. On a different sample, an area with a mix of quartz, carrollite and Mg silicates had a higher surface hardness than an area containing only carrollite. That implied that zones of pure carrollite are potentially quite brittle.

Fourier Transformed InfraRed has shown to be useful in characterising the gangue minerals and in some cases also carrollite. Carrollite could only be identified if no other IR active minerals were present, meaning that in some cases FTIR can be used to identify zones containing cobalt. The fundamental vibrations of bonds could be seen for eight different minerals. Four pure spectra could be identified and an additional eight mixed spectra. Using those twelve spectra to interpret the 325 gathered spectra, an attempt has been made to quantify the mineralogy. The modal mineralogy through FTIR contained fewer detail than the QEMSCAN data and in the most cases carrollite was not identified, but was in good agreement for the identified minerals. The spectra allowed for refining of the QEMSCAN mineralogy, as it was possible to differentiate between talc or serpentine and muscovite or illite. FTIR has shown to be a useful geometallurgical tool, but mainly for metallurgical purposes, such as detecting minerals with high acid consumption. No information can be obtained about the mineral texture, which has been the main factor influencing the comminution behaviour. This means that FTIR data cannot be directly linked to comminution influencing properties.

When linking the surface hardness to the comminution experiments, it appeared that the surface hardness is related to variation of the Particle Size Distribution within a mineral texture class. The higher the

surface hardness, the coarser the Particle Size Distribution. A relatively high cobalt grade was found in the fines of the ground samples for all textures, potentially confirming the brittleness of pure carrollite. In total three different comminution classes have been identified for the sulphide zone using laboratory comminution tests. These classes are based on the increase in fines with a particle diameter below 106 μm per minute of grinding. This increase in fines is related to the carrollite texture class. Three textural comminution classes have been identified: banded, vein and disseminated texture type. In order to quantify differences in the comminution behaviour of the samples, laboratory experiments have been required: solely characterising the material is not enough at this moment. Using simulation, it has been possible to quantify the energy requirements for the comminution classes: the differences can be up to 27% for the crushing phase.

7.2. Recommendations

It was mentioned in the thesis that the chemical data obtained using the portable XRF requires calibration. That should be one of the first steps in future work on the project. The calibration is done by performing both quantitative laboratory XRF and pXRF measurements on identical samples. Copper and cobalt grade of the two tests can be plotted against each other, after which a calibration constant can be derived.

As mineral texture has shown to be the main factor of influence for comminution behaviour, it is recommended to determine at what resolution a CT scan can be used to determine differences in texture type. If differences can be distinguished within a number of minutes, it could be used as a geometallurgical domaining tool.

Additional FTIR measurements on known pre-defined mixtures with known mineralogy and grain sizes, will confirm that the observed spectra in this thesis are representative for the mineral mixtures. It is also recommended to use a range of grain sizes, as that will provide insights in the influence of grain size on the mixing of these specific spectra.

The surface hardness appeared to linked to the coarseness of a particle size distribution within a comminution class. For this to be confirmed, additional surface hardness measurements and comminution experiments will be required. This makes the Equotip potentially a very useful tool in determining the optimum residence time of subclasses within texture types, as for the post comminution steps a fine particle size will be required.

Following the comminution tests, additional processing and metallurgical experiments will be required. This will give insights in the variability of required consumables, processing steps and eventual recovery of metals throughout the deposit. These differences can be used to develop a complete simulated flowsheet, allowing to study the influence of the resource variability on industrial scale.

In order to get an indication of the influence of these mineralogical, processing and metallurgical parameters on the mining sequence two scenarios need to be evaluated. One scenario should consider the basic block model and develop an optimum mining sequence, whilst the second scenario will consider the block model containing the additional geometallurgical parameters. The difference in Net Present Value between the two scenarios allows for quantifying the value of the geometallurgical sequencing approach.

Finally, it is important to study the influence of the gangue minerals on the eventual tailings and to assess the influence of those tailing on the environment. That would make the geometallurgical study a complete one.

Bibliography

[1] J. C. Ø. Andersen, G. K. Rollinson, B. Snook, R. Herrington, and R. J. Fairhurst, October 2009. Use of QEM-SCAN® for the characterization of Ni-rich and Ni-poor goethite in laterite ores. *Minerals Engineering*, 22(13):1119–1129.

[2] K. F. E. Anderson, F. Wall, G. K. Rollinson, and C.J. Moon, October 2014. Quantitative mineralogical and chemical assessment of the Nkout iron ore deposit, Southern Cameroon. *Ore Geology Reviews*, 62:25–39.

[3] H. Aoki and Y. Matsukura, February 2008. Estimating the unconfined compressive strength of intact rocks from Equotip hardness. *Bulletin of Engineering Geology and the Environment*, 67(1):23–29.

[4] B. D. Ballard et al., November 2007. Quantitative mineralogy of reservoir rocks using Fourier transform infrared spectroscopy. In *SPE Annual Technical Conference and Exhibition*, pages 1–8. Society of Petroleum Engineers.

[5] M. Becker, J.A. Jardine, M.A .and Miller, and M. Harris, June 2016. X-ray computed tomography–a geometallurgical tool for 3d textural analysis of drill core. In *Proceedings of the 3rd AusIMM International Geometallurgy Conference*, pages 231–240, Melbourne, June 2016. Australasian Institute of Mining and Metallurgy.

[6] A. Benedictus, P. Berendsen, and A.M. Hagni, December 2008. Quantitative characterisation of processed phlogopite ore from Silver City Dome District, Kansas, USA, by automated mineralogy. *Minerals Engineering*, 21(15):1083–1093.

[7] J. Benndorf, October 2015. Lectures in resource modelling and reserve estimation. TU Delft Course.

[8] D. Bennett and D. La Rosa, June 2016. Geometallurgy - bridging the gap between mine and mill: a case study of the Degrussa geometallurgy program. In *Proceedings of the 3rd AusIMM International Geometallurgy Conference*, pages 77 – 88, Melbourne, June 2016. Australasian Institute of Mining and Metallurgy.

[9] J. Bertaux, F. Frohlich, and P. Ildefonse, May 1998. Multicomponent analysis of FTIR spectra: quantification of amorphous and crystallized mineral phases in synthetic and natural sediments. *Journal of Sedimentary Research*, 68(3):440–447.

[10] M.R. Bloemsma, September 2015. *Development of a Modelling Framework for Core Data Integration using XRF Scanning*. PhD thesis, Delft University of Technology.

[11] M. Boni, G. Rollinson, N. Mondillo, G. Balassone, and L. Santoro, May 2013. Quantitative mineralogical characterization of Karst bauxite deposits in the Southern Apennines, Italy. *Economic Geology*, 108(4): 813–833.

[12] D. Bradshaw, October 2014. The role of process mineralogy in improving the process performance of complex sulphide ores. In *Proceedings of the XXVII International Mineral Processing Congress*, pages 1–23, Santiago, Chile, October 2014. International Mineral Processor's Conference.

[13] N.W. Brand and C.J. Brand, February 2014. Performance comparison of portable XRF instruments. *Geochemistry: Exploration, Environment, Analysis*, 14(2):158–172.

[14] M. Brissette, V. Mihajlovic, and S. Sanuri, October 2014. Geometallurgy: New accurate test work to meet required accuracies of mining project development. In *Proceedings of the XXVII International Mineral Processing Congress*, pages 200–209, Santiago, Chile, October 2014. International Mineral Processor's Conference.

[15] A.R. Butcher, T.A. Helms, P. Gottlieb, R. Bateman, S. Ellis, and N.W. Johnson, October 2000. Advances in the quantification of gold deportment by QEMSCAN. In *Seventh Mill Operators Conference, Kalgoorlie, Western Australia*, pages 267–272. Australasian Institute of Mining and Metallurgy.

[16] J.L.H. Cailteux, A.B. Kampunzu, C. Lerouge, A.K. Kaputo, and J.P. Milesi, September 2005. Genesis of sediment-hosted stratiform copper-cobalt deposits, Central African Copperbelt. *Journal of African Earth Sciences*, 42(1):134–158.

[17] R. Chaigneau, February 2017. Physical processing. Reader AESB 3342, TU Delft Course.

[18] E. Chait and R. Schiller, June 2016. Adding copper recovery and acid consumption variables to the geological model of the Quebrada Blanca. In *Proceedings of the 3rd AusIMM International Geometallurgy Conference*, pages 257 – 266, Melbourne, June 2016. Australasian Institute of Mining and Metallurgy.

[19] R. Clark, G. Swayze, R. Wise, E. Livo, T. Hoefen, R. Kokaly, and S. Sutley, 2007. Usgs spectral library. URL http://speclab.cr.usgs.gov/spectral-lib.html.

[20] R.N. Clark, June 1999. Spectroscopy of rocks and minerals, and principles of spectroscopy. In A. N. Rencz, editor, *Manual of remote sensing*, volume 3, chapter 1, pages 3–58. John Wiley and Sons, Chichester, UK.

[21] V. Cnudde and M.N. Boone, August 2013. High-resolution X-ray computed tomography in geosciences: a review of the current technology and applications. *Earth-Science Reviews*, 123:1–17.

[22] M.A. Coombes, A. Feal-Pérez, L.A. Naylor, and K. Wilhelm, December 2013. A non-destructive tool for detecting changes in the hardness of engineering materials: application of the Equotip durometer in the coastal zone. *Engineering Geology*, 167:14–19.

[23] F.K. Crundwell, M.S. Moats, V. Ramachandran, T.G. Robinson, and W.G. Davenport, 2011. Production of cobalt from the copper–cobalt ores of the central african copperbelt. In *The Extractive Metallurgy of Nickel, Cobalt and Platinum Group Elements*, chapter 30, pages 377–391. Elsevier Ltd, Oxford, United Kingdom.

[24] Q. Dehaine, L.T. Tijsseling, and H.J. Glass, July 2017. Cobalt geology, geometallurgy and geomicrobiology (CoG3) project progress report. Update Presentation for National History Museum.

[25] S. Dewaele, P. Muchez, H. El Desouky, M. Haest, and W. Heijlen, April 2008. Multiphase origin of the base metal deposits in the Lufilian fold-and-thrust belt, Katanga (Democratic Republic of Congo). *Journal of African Earth Sciences*, 46:455–469.

[26] S. Dunham, J. Vann, and S. Coward, September 2011. Beyond geometallurgy—gaining competitive advantage by exploiting the broad view of geometallurgy. In *The First AUSIMM International Geometallurgy Conference*, pages 115–124, Melbourne, September 2011. Australasian Institute of Mining and Metallurgy.

[27] K.G. Fisher, L.G. Treadgold, and G. Fisher, June 2008. Design considerations for the cobalt recovery circuit of the KOL (KOV) copper/cobalt refiner, DRC. Presentation at ALTA Nickel Cobalt Conference.

[28] L. Fisher, M. F Gazley, A. Baensch, S. J. Barnes, J. Cleverley, and G. Duclaux, February 2014. Resolution of geochemical and lithostratigraphic complexity: a workflow for application of portable X-ray fluorescence to mineral exploration. *Geochemistry: Exploration, Environment, Analysis*, 14(2):149–159.

[29] M.F. Gazley and L.A. Fisher, February 2014. A review of the reliability and validity of portable x-ray fluorescence spectrometry (pXRF) data. *Mineral Resource and Ore Reserve Estimation–The AusIMM Guide to Good Practice*, pages 69–82.

[30] Y. Ghorbani, M. Becker, J. Petersen, S.H. Morar, A. Mainza, and J.P. Franzidis, October 2011. Use of X-ray computed tomography to investigate crack distribution and mineral dissemination in sphalerite ore particles. *Minerals Engineering*, 24(12):1249–1257.

[31] Glencore, November 2013. Mutanda Mining Sarl - site visit November 2013. Presentation available online for visitors.

[32] W.R. Goodall and P.J. Scales, April 2007. An overview of the advantages and disadvantages of the determination of gold mineralogy by automated mineralogy. *Minerals Engineering*, 20(5):506–517.

[33] W.R. Goodall, P.J. Scales, and A.R. Butcher, July 2005. The use of QEMSCAN and diagnostic leaching in the characterisation of visible gold in complex ores. *Minerals Engineering*, 18(8):877–886.

[34] P. Gottlieb, G. Wilkie, D. Sutherland, E. Ho-Tun, S. Suthers, K. Perera, B. Jenkins, S. Spencer, A. Butcher, and J. Rayner, April 2000. Using quantitative electron microscopy for process mineralogy applications. *The Journal of The Minerals, Metals & Materials Society*, 52(4):24–25.

[35] D. Haberlah, C. Strong, D. Pirrie, G.K. Rollinson, P. Gottlieb, P.P.W.S.K. Botha, and A.R Butcher, December 2011. Automated petrography applications in Quaternary science. *Quaternary Australasia*, 28(2):3–12.

[36] G.E.M. Hall, G.F. Bonham-Carter, and A. Buchar, March 2014. Evaluation of portable x-ray fluorescence (pxrf) in exploration and mining: Phase 1, control reference materials. *Geochemistry: Exploration, Environment, Analysis*, 14(2):99–123.

[37] E.M. Harper, G. Kavlak, and T.E. Graedel, December 2011. Tracking the metal of the goblins: Cobalt's cycle of use. *Environmental science & technology*, 46(2):1079–1086.

[38] R. Herman, November 2016. Technical mineral resource estimate update report: Mutanda south copper deposit, DRC. Technical Report R1125-2016-GMS, Riaan Herman Consulting, 1063 Kyalami st, Raslouw Glen 0157, Centurion, South Africa.

[39] W. Herres and J. Gronholz, 1984. Understanding FT-IR data processing: part 1. *Bruker Analytische Meßtechnik GmbH.*

[40] R.D. Hewson and T.J. Cudahy, January 2013. TIR hyperspectral interpretation of quartz crystallinity and composition within silicate bearing rocks. In *Geoscience and Remote Sensing Symposium (IGARSS), 2013 IEEE International*, pages 3076–3079. IEEE.

[41] X Hou, Y. He, and B.T. Jones, August 2004. Recent advances in portable X-ray fluorescence spectrometry. *Applied Spectroscopy Reviews*, 39(1):1–25.

[42] Innov-X, March 2010. Delta HHXRF Analysers - manual and limits of detection. Innov-X-Systems. http://usenvironmental. com/download/manuals/Olympus.

[43] P. Itävuo, M. Vilkko, A. Jaatinen, and K. Viilo, April 2013. Dynamic modeling and simulation of cone crushing circuits. *Minerals Engineering*, 43:29–35.

[44] J. Jackson, A.J. McFarlane, and K. Olson Hoal, September 2011. Geometallurgy-back to the future: scoping and communicating geomet programs. In *GeoMet 2011-1st AusIMM International Geometallurgy Conference 2011*, pages 125–131, Melbourne, September 2011. Australasian Institute of Mining and Metallurgy.

[45] L. Keeney, November 2008. EQUOtip hardness testing: Ernest Henry (including a guide on how to use EQUOtip). Technical Report GeMIII (Amira P843) - Technical Report 2, GeMIII.

[46] G.S. King and J.L. Macdonald, June 2016. The business case for early-stage implementation of eometallurgy - an example from the Productora Cu-Mo-Au Deposit, Chile. In *Proceedings of the 3rd AusIMM International Geometallurgy Conference*, pages 125–134, Melbourne, June 2016. Australasian Institute of Mining and Metallurgy.

[47] R.P. King, February 1994. Comminution and liberation of minerals. *Minerals Engineering*, 7(2-3):129–140.

[48] R.P. King, 2012. Particle populations and distribution functions. In C.L. Schneider and E.Al King, editors, *Modeling and simulation of mineral processing systems*, chapter 2, pages 7–55. Society for Mining, Metallurgy and Exploration, Englewood, Colorado, second edition.

[49] P.H. Koch and J. Rosenkranz, February 2017. Texture-based liberation models for comminution. In *Konferens i Mineralteknik 2017, Luleå 7-8 February 2017*, pages 83–96. Luleå University of Technology.

[50] K. Kongolo, M.D. Mwema, A.N. Banza, and E Gock, December 2003. Cobalt and zinc recovery from copper sulphate solution by solvent extraction. *Minerals Engineering*, 16(12):1371–1374.

[51] F.A. Kruse, June 2002. Combined SWIR and LWIR mineral mapping using MASTER/ASTER. In *Geoscience and Remote Sensing Symposium, 2002. IGARSS'02. 2002 IEEE International*, volume 4, pages 2267–2269. IEEE.

[52] P. Lamberg, February 2011. Particles-the bridge between geology and metallurgy. In *Konferens i mineralteknik 2011: 08/02/2011-09/02/2011*. Luleå University of Technology.

[53] V. Liebezeit, K. Ehrig, A. Robertson, D. grant, and M. Smith, June 2016. Embedding geometallurgy into mine planning practices - practical examples at olympic dam. In *Proceedings of the 3rd AusIMM International Geometallurgy Conference*, pages 135–144. Australasian Institute of Mining and Metallurgy.

[54] LME, April 2017. London metal exhange - metal prices. URL http://www.lme.com/metals/.

[55] N.O. Lotter, L.J. Kormos, J. Oliveira, D. Fragomeni, and E. Whiteman, June 2011. Modern process mineralogy: two case studies. *Minerals Engineering*, 24(7):638–650.

[56] C. Lund, June 2013. *Mineralogical, chemical and textural characterisation of the Malmberget iron ore deposit for a geometallurgical model*. PhD thesis, Luleå University of Technology.

[57] C. Lund and P. Lamberg, April 2014. Geometallurgy–a tool for better resource efficiency. *European Geologist*, 37:39–43.

[58] A.S. Macfarlane and T.P. Williams, November 2014. Optimizing value on a copper mine by adopting a geometallurgical solution. *Journal of the Southern African Institute of Mining and Metallurgy*, 114(11): 929–935.

[59] L. Mancini, C. De Camillis, and D. Pennington, November 2013. Security of supply and scarcity of raw materials. towards a methodological framework for sustainability assessmen. *European Commission, Joint Research Centre, Institute for Environment and Sustainability,*, page 41.

[60] A. Matteson and M.M. Herron, 1993. Quantitative mineral analysis by Fourier transform infrared spectroscopy. In *Society of Core Analysts Conference Paper*, number 9308, pages 1–15.

[61] Mbendi, October 2015. Nickel and cobalt mining in democratic republic of the congo.

[62] F.W. McQuiston and L.J. Bechaud, 1968. Metallurgical sampling and testing. *Surface mining. New York: The American Institute of Mining, Metallurgical and Petroleum Engineers*, pages 103–121.

[63] F. Mees, R. Swennen, M. Van Geet, and P. Jacobs, January 2003. Applications of X-ray computed tomography in the geosciences. *Geological Society, London, Special Publications*, 215(1):1–6.

[64] Mindat.org, 2017. Mindat.org - mineral database. URL https://www.mindat.org.

[65] P.A. Montoya, L. Keeney, R. Jahoda, J. Hunt, R. Berry, U. Drews, V. Chamberlain, and S. Leichliter, September 2011. Geometallurgical modelling techniques applicable to prefeasibility projects–La Colosa case study. In *The First AUSIMM International Geometallurgy Conference*, pages 103–114, Melbourne, September 2011. Australasian Institute of Mining and Metallurgy.

[66] C.J. Moon, M.K.G. Whateley, A.M. Evans, W.L. Barrett, T. Bell, J. Milsom, , and B.C. Scott, 2006. Ore, mineral economics and mineral exploration. In C.J. Moon, M.K.G. Whateley, and A.M. Evans, editors, *Introduction to Mineral Exploration*, chapter 1. Blackwell Publishing, Oxford, United Kingdom, second edition.

[67] S. Morrell, 2004. Predicting the specific energy of autogenous and semi-autogenous mills from small diameter drill core samples. *Minerals Engineering*, 17(3):447–451.

[68] G.M. Mudd, Z. Weng, S.M. Jowitt, I.D. Turnbull, and T.E. Graedel, 2013. Quantifying the recoverable resources of by-product metals: The case of cobalt. *Ore Geology Reviews*, 55:87–98.

[69] A. Mwanga, 2014. *Test methods for characterizing ore Comminution Behavior in Geometallurgy*. PhD thesis, Luleå University of Technology.

[70] A. Mwanga, J. Rosenkranz, and P. Lamberg, July 2017. Development and experimental validation of the geometallurgical comminution test (GCT). *Minerals Engineering*, 108:109–114.

[71] T.J. Napier-Munn, S. Morrell, R.D. Morrison, and T. Kojovic, 1996. Models of comminution processes. In T.J. Napier-Munn, editor, *Mineral comminution circuits: their operation and optimisation*, volume 2, chapter 2, pages 10–33. JKMRC, University of Queensland, Brisbane, Australia.

[72] NHM, 2017. National History Museum - CoG3 project overview. URL http://www.nhm.ac.uk/our-science/our-work/sustainability/cog3-cobalt-project.html.

[73] G. Notesco, V. Kopačková, P. Rojík, G. Schwartz, I. Livne, and E.B. Dor, July 2014. Mineral classification of land surface using multispectral LWIR and hyperspectral SWIR remote-sensing data. a case study over the Sokolov lignite open-pit mines, the Czech Republic. *Remote Sensing*, 6(8):7005–7025.

[74] J.A. Ober, January 2017. Mineral commodity summaries 2017. URL https://minerals.usgs.gov/minerals/pubs/mcs/2017/mcs2017.pdf.

[75] S. Okawa, M. Ohoka, and A. Funato, 1999. Application of hardness tester to rock specimens. In *Proceedings of the 29th symposium of rock mechanics*, pages 256–260, Minneapolis, Minnesota, 1999. JCSE.

[76] A. Parbhakar-Fox, B. Lottermoser, and D.J. Bradshaw, 2013. Cost-effective means for identifying acid rock drainage risks: integration of the geochemistry-mineralogy-texture approach and geometallurgical techniques. In *The Second AusIMM International Geometallurgy Conference (GeoMet) 2013*, volume 1, pages 143–154, Melbourne, 2013. Australasian Institute of Mining and Metallurgy.

[77] R.D. Pascoe, M.R. Power, and B. Simpson, April 2007. QEMSCAN analysis as a tool for improved understanding of gravity separator performance. *Minerals Engineering*, 20(5):487–495.

[78] I. Plyusnina, 1978. Study of structural disorder of chalcedonies by infrared spectroscopy. *Soviet Physics Doklady*, 23(6):363–265.

[79] A.S. Povnnennykh, 1978. The use of infrared spectra for the determination of minerals. *American Mineralogist*, 63:956–959.

[80] SA Proceq, 1977. Equotip operations instructions. *PROCEQ SA, Zurich*.

[81] M.S. Ramsey and P.R. Christensen, January 1998. Mineral abundance determination: Quantitative deconvolution of thermal emission spectra. *Journal of Geophysical Research: Solid Earth*, 103(B1):577–596.

[82] L. Robb, 2013. Hydrothermal processes. In *Introduction to ore-forming processes*, chapter Two, pages 198–202. Blackwell Publishing, Oxford, United Kingdom, first edition.

[83] G.K. Rollinson, J.C.Ø. Andersen, R.J. Stickland, M. Boni, and R. Fairhurst, July 2011. Characterisation of non-sulphide zinc deposits using QEMSCAN®. *Minerals Engineering*, 24(8):778–787.

[84] P.-S. Ross, A. Bourke, and B. Fresia, February 2014. Improving lithological discrimination in exploration drill-cores using portable X-ray fluorescence measurements:(1) testing three Olympus Innov-X analysers on unprepared cores. *Geochemistry: Exploration, Environment, Analysis*, pages 2012–163.

[85] R.A.V. Rossel, D.J.J. Walvoort, A.B. McBratney, L.J. Janik, and J.O. Skjemstad, March 2006. Visible, near infrared, mid infrared or combined diffuse reflectance spectroscopy for simultaneous assessment of various soil properties. *Geoderma*, 131(1):59–75.

[86] J.W. Salisbury, L.S. Walter, and N. Vergo, 1987. Mid-infrared (2.1-25 um) spectra of minerals. Open File Report 87-263, US Geological Survey,.

[87] H. Sanderson, March 2017. Cobalt's meteoric rise at risk from congo's katanga. URL https://www.ft.com/content/bc8dc13c-07db-11e7-97d1-5e720a26771b?mhq5j=e3.

[88] L. Santoro, G.K. Rollinson, M. Boni, and N. Mondillo, June 2015. Automated scanning electron microscopy (QEMSCAN®)-based mineral identification and quantification of the Jabali Zn-Pb-Ag nonsulfide deposit (Yemen). *Economic Geology*, 110(4):1083–1099.

[89] D. Sheppard, N. Hume, and H. Sanderson. Glencore to buy Gertler out of its DRC copper and cobalt mines. URL `https://www.ft.com/content/bdeaf748-f20a-11e6-8758-6876151821a6?mhq5j=e3`.

[90] V. Singh and R. Venugopal, November 2014. Effect of morphology on breakage and liberation characteristics of minerals and coal. *Minerals and Metallurgical Processing*, 31(4):182–192.

[91] K.C. Sole and O.S. Tinkler, June 2016. Copper solvent extraction: Status, operating practices, and challenges in the African Copperbelt. *Journal of the Southern African Institute of Mining and Metallurgy*, 116 (6):553–560.

[92] W.R Stockwell, September 2017. Fourier Transform Infrared Spectroscopy. URL `https://chem.libretexts.org/LibreTexts/Howard_University/Howard%3A_Physical_Chemistry_Laboratory/14._Fourier_Transform_Infrared_Spectroscopy_(FTIR)`.

[93] B. Swartz, S. Donegan, and S. Amos, 2009. Processing considerations for cobalt recovery from Congolese copperbelt ores. In *Proceedings Hydrometallurgy Conference 2009*, pages 385–400.

[94] J.L. Thomson and J.W. Salisbury, July 1993. The mid-infrared reflectance of mineral mixtures (7–14 μm). *Remote Sensing of Environment*, 45(1):1–13.

[95] L.T. Tijsseling, August 2017. Mutanda visit report. Summary of week on site.

[96] J. Vargas, C. Lozano, and C. Bisso, October 2014. Geometallurgical model of sag milling at minera esperanza. In *Proceedings of the XXVII International Mineral Processing Congress*, pages 240–247, Santiago, Chile, October 2014. IMPC.

[97] W. Verwaal and A. Mulder, December 1993. Estimating rock strength with the Equotip hardness tester. *International Journal of Rock Mechanics and Mining Sciences & Geomechanics*, 30(6):659–662.

[98] K. Viilo, 2011. Porcess simulation. In *Crushing and Screening Handbook*, chapter Six, pages 22–24. Metso Minerals,, Tampere, Finland, six edition.

[99] T.G. Vizcarra, E.M. Wightman, N.W. Johnson, and E.V. Manlapig, April 2010. The effect of breakage mechanism on the mineral liberation properties of sulphide ores. *Minerals Engineering*, 23(5):374–382.

A

QEMSCAN Samples

Photos of the sulphide thin sections that were analysed using QEMSCAN.
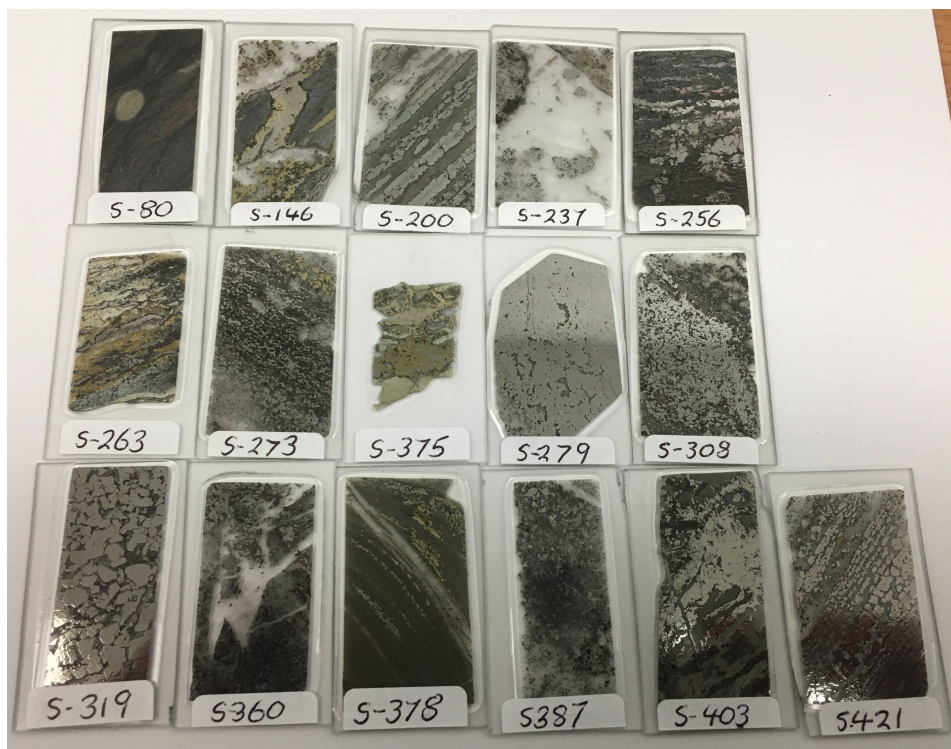
Figure A.1: Thin Sections QEMSCAN Sulphide Batch 1
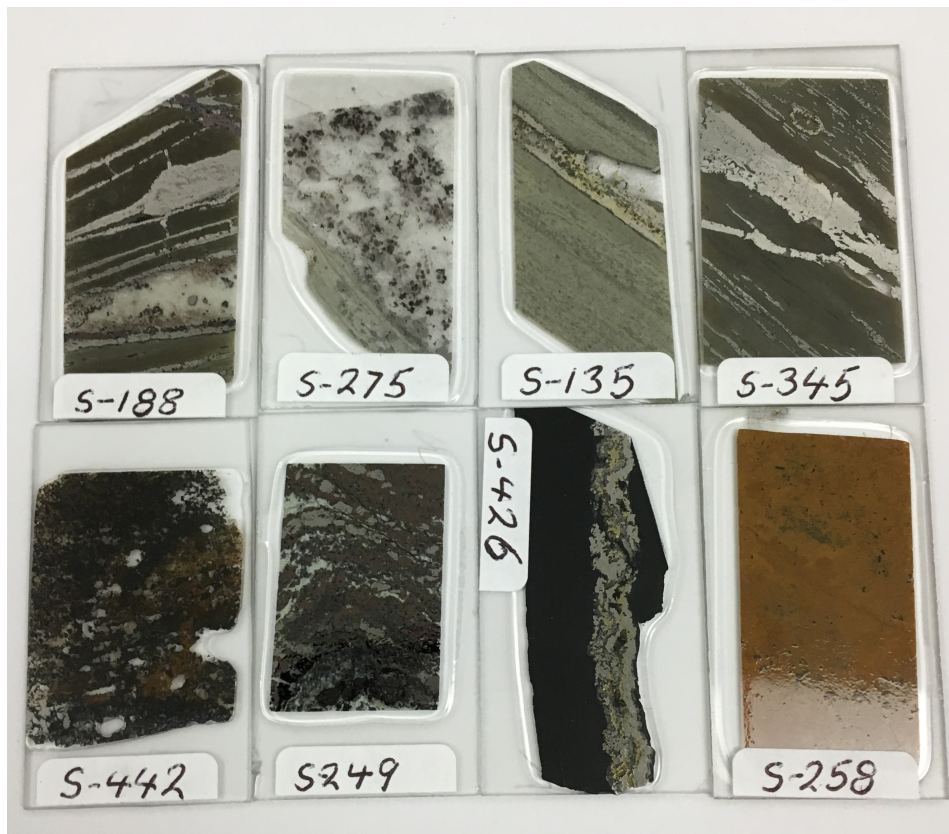
Figure A.2: Thin Sections QEMSCAN Sulphide Batch 2

B

QEMSCAN Mineral Description

Color coding and description of the minerals as identified by QEMSCAN.

Mineral Category	Mineral Description
Background	All resin/mounting media and related edge effects
Carrollite	Any phase with Co,Cu,S
Chalcopyrite	Any phase with Fe,Cu,S, (Fe>Cu) such as Chalcopyrite
Bornite	Any phase with Cu,Fe,S, (Cu>Fe) such as Bornite
Chalcocite	Any phase with Cu,S, includes mostly Chalcocite with minor Covellite
Pyrite	Any phase with Fe,S such as Pyrite/Marcasite.
Barite	Any phase with Ba,S,O
Gypsum	Any phase with Ca,S,O.
Cu Oxide	Copper Oxides such as Cuprite and Tenorite
Pseudomalachite	Any phase with Cu,P,O,H.
Malachite	Copper Carbonates such as Malachite and Azurite (Cu,O,C), includes Cu-Fe Ox/CO3
Chysocolla	Any phase with Cu,Al,Na,Si. Includes low Fe & Mg
Heterogenite	Any phase with Co,O,H. May include Fe
Kolwezite	Any phase with Co,Cu,O,C. Includes Fe Kolwezite (Co,Cu,O,C,Fe)
Cupro-Asbolane	Any phase with Cu,Co,Mn,Fe,O and Cu,Co,Mn,O. May include Si & has variable chemistry
Cupro-Asbolane (Cl)	Any phase with Cu,Co,Mn,Fe,O & Cl. May include Si & has variable chemistry
Co Mn Al	Any phase with Co,Mn,Al. May include Lithiophorite, Masrite (S poor), Asbolane, Cobaltoan Rhodochrosite
Fe-Ox/CO3	Fe oxides & carbonates such as Siderite, Goethite, Hematite, Magnetite, Mn-Fe oxides.
Rutile	Any phase with Ti,O (Rutile/Anatase/Brookite).
Ilmenite	Any phase with Fe,Ti,O.
Dolomite	Any phase with Ca,Mg,O,C.
Fe Dolomite/Ankerite	Any phase with Ca,Mg,O,C, with low Fe
Apatite	Any phase with Ca,P,O.
Magnesite	Any phase with Mg,O,C
Quartz	Quartz and other silica minerals
Plagioclase	Plagioclase Feldspars: phases with Na,Al,Si,O to Ca,Al,Si,O.
K-feldspar	K-Feldspars (Orthoclase, Sanidine, Microcline): any phase with K,Al,Si,O
Muscovite/Illite	Any phase with K,Al,Si,O. Includes Muscovite/Lepidolite Mica, Fe Muscovite & Illite.
Biotite	Any phase with Fe,Al,K Si,Mg,O (Fe>Mg). May include other Biotite, Zinnwaldite
Phlogopite	Any phase with Mg,Fe,Al,K Si,O (Mg>Fe) such as Phlogopite
Magnesiochlorite	Any phase with Mg,Al,Si,O such as Magnesiochlorite, and other similar minerals
Mg silicates	Any phase with Mg,Si,O such as Talc, the Serpentine Group, Sepiolite
Kaolinite	Any phase with Al,Si,O such as Kaolinite/Halloysite/Dickite (Al:Si equal ratio approx.)
Zircon	Any phase with Zr,Si,O
Monazite	Includes Monazite (Ce-La-Nd,P,O) & Xenotime , and possibly other REE minerals
Others	Any other mineral not included above.

Mineral Name

- Background
- Carrollite
- Chalcopyrite
- Bornite
- Chalcocite
- Pyrite
- Barite
- Gypsum
- Cu Oxide
- Pseudomalachite
- Malachite
- Chysocolla
- Heterogenite
- Kolwezite
- Cupro-Asbolane
- Cupro-Asbolane (Cl)
- Co Mn Al
- Fe-Ox/CO3
- Rutile
- Ilmenite
- Dolomite
- Fe Dolomite/Ankerite
- Apatite
- Magnesite
- Quartz
- Plagioclase
- K-feldspar
- Muscovite/Illite
- Biotite
- Phlogopite
- Magnesiochlorite
- Mg silicates
- Kaolinite
- Zircon
- Monazite
- Others

Figure B.1: Mineral Description and Color Coding of QEMSCAN Samples

FTIR Spectra Mineral Data per Pixel

The results of the minerals found in the spectra per pixel are displayed here, a 1 means that the mineral could be identified in the spectrum and a 0 means that it was not present in the spectrum.

Table C.1: Overview of Minerals Measured using FTIR for S-237, S-258 and S-273

Sample	Pixel	Dolomite	Quartz
S-237	1	1	1
	2	1	1
	3	1	1
	4	1	1
	5	1	1
	6	1	1
	7	1	1
	8	1	1
	9	1	1
	10	1	1
	11	1	1
	12	1	1
	13	1	1
	14	1	1
	15	1	1
		Dolomite	**Quartz**
S-258	1	1	1
	2	1	1
	3	1	1
	4	1	1
	5	1	0
	6	1	1
	7	1	1
	8	1	1
	9	1	1
	10	1	1
	11	1	1
	12	1	1
		Quartz	**Dolomite**
S-273	1	1	1
	2	1	1
	3	1	1
	4	1	1
	5	1	1
	6	1	1
	7	1	1
	8	1	1
	9	1	1
	10	1	1
	11	1	1
	12	1	1
	13	1	1
	14	1	1
	15	1	1

Table C.2: Overview of Minerals Measured using FTIR for S-279, S-360 and S-421

Sample	Pixel	Quartz	Carrollite
S-279	1	1	1
	2	0	1
	3	1	1
	4	1	1
	5	1	1
	6	0	1
	7	1	1
	8	1	1
	9	1	1
	10	0	1
	11	0	1
	12	0	1
	13	1	1
		Dolomite	**Quartz**
S-360	1	1	1
	2	1	1
	3	1	1
	4	1	1
	5	1	1
	6	1	1
	7	1	1
	8	1	1
	9	1	1
	10	1	1
	11	1	1
	12	1	1
		Dolomite	**Serpentine**
S-421	1	1	1
	2	1	1
	3	1	1
	4	1	1
	5	1	1
	6	1	1
	7	1	1
	8	1	1
	9	1	1
	10	1	1

Table C.3: Overview of Minerals Measured using FTIR for S-135, S-146 and S-256

Sample	Pixel	Illite	Quartz	K-feldspar
S-135	1	1	1	1
	2	1	1	1
	3	1	1	1
	4	1	0	0
	5	1	1	0
	6	1	1	0
	7	1	1	1
	8	0	1	1
	9	1	1	1
	10	1	1	1
	11	1	1	1
	12	1	1	1
		Dolomite	**Quartz**	**Muscovite**
S-146	1	1	1	1
	2	1	0	1
	3	1	0	1
	4	1	1	1
	5	1	0	1
	6	1	1	1
	7	1	0	1
	8	1	0	1
	9	1	1	1
	10	1	0	1
	11	1	1	1
	12	0	0	1
	13	0	1	1
	14	1	1	1
		Quartz	**Dolomite**	**Chlorite**
S-256	1	1	1	1
	2	1	1	1
	3	1	1	1
	4	1	0	0
	5	1	0	0
	6	1	1	1
	7	1	0	1
	8	1	0	1
	9	1	0	1
	10	1	0	0
	11	1	0	0
	12	0	0	1
	13	1	0	0
	14	1	0	0
	15	1	0	1
	16	1	0	0

Table C.4: Overview of Minerals Measured using FTIR for S-135, S-146 and S-256

Sample	Pixel	Quartz	Dolomite	Serpentine
S-275	1	1	0	0
	2	1	1	0
	3	1	1	0
	4	1	1	1
	5	1	1	0
	6	1	1	0
	7	1	1	0
	8	1	1	1
	9	1	1	0
	10	1	1	1
	11	1	1	0
	12	1	1	1
	13	1	1	0
	14	1	1	0
		Quartz	**Dolomite**	**Serpentine**
S-308	1	1	1	1
	2	1	1	1
	3	1	1	1
	4	1	1	0
	5	1	0	0
	6	1	1	0
	7	0	1	1
	8	1	1	1
	9	1	1	1
	10	1	0	0
	11	1	1	1
	12	1	1	1
	13	1	1	1
	14	1	1	1
	15	1	1	1
		Serpentine	**Quartz**	**Carrollite**
S-314	1	1	1	1
	2	1	1	1
	3	1	1	1
	4	1	1	1
	5	1	1	1
	6	1	1	1
	7	1	1	1
	8	1	1	1
	9	1	1	1
	10	1	1	1
	11	1	0	1
	12	1	1	1
	13	1	1	1
	14	1	1	1
	15	1	1	1

Table C.5: Overview of Minerals Measured using FTIR for S-345, S-387 and S-426

Sample	Pixel	Quartz	Talc	Chlorite
S-345	1	1	1	
	2	1	1	1
	3	1	1	1
	4	1	1	0
	5	1	1	1
	6	1	1	1
	7	1	1	1
	8	1	1	1
	9	1	1	1
	10	1	1	1
	11	1	1	1
	12	1	1	1
	13	1	1	1
	14	1	1	1
	15	1	1	1
		Quartz	**Dolomite**	**Serpentine**
S-387	1	1	0	1
	2	1	0	0
	3	1	0	0
	4	1	1	0
	5	1	1	0
	6	1	0	0
	7	1	0	0
	8	1	1	0
	9	1	1	0
	10	1	1	1
	11	1	1	0
	12	1	1	0
		Quartz	**K-feldspar**	**Illite**
S-426	1	1	0	1
	2	1	1	1
	3	1	1	1
	4	1	1	0
	5	1	0	0
	6	1	1	1
	7	1	1	0
	8	1	1	1
	9	1	1	1
	10	1	1	1
	11	1	1	1

Table C.6: Overview of Minerals Measured using FTIR for S-188, S-200 and S-249

Sample	Pixel	Quartz	Chlorite	Talc	Dolomite
S-188	1	1	1	1	0
	2	1	1	1	1
	3	1	1	1	0
	4	1	1	1	0
	5	1	1	1	1
	6	1	1	1	0
	7	1	1	1	1
	8	1	1	1	0
	9	1	1	1	0
	10	1	1	1	0
	11	1	1	1	0
	12	1	1	1	1
	13	1	1	1	0
	14	1	1	1	0
		Quartz	**Dolomite**	**Chlorite**	**Talc**
S-200	1	1	1	1	1
	2	1	1	1	1
	3	1	1	1	1
	4	1	1	1	1
	5	1	1	0	1
	6	1	1	0	1
	7	1	1	0	1
	8	1	1	1	1
	9	1	1	0	1
	10	1	1	0	1
	11	1	1	0	1
	12	1	1	1	1
	13	1	1	0	0
	14	1	1	0	1
	15	1	1	0	0
	16	1	1	0	1
		Dolomite	**Quartz**	**Talc**	**Chlorite**
S-249	1	0	1	1	1
	2	1	1	1	1
	3	1	1	1	1
	4	1	1	1	1
	5	1	1	1	1
	6	1	1	1	1
	7	1	1	1	1
	8	1	1	1	1
	9	1	1	1	1
	10	1	1	1	1
	11	1	1	1	1

Table C.7: Overview of Minerals Measured using FTIR for S-263 and S-278

Sample	Pixel	Chlorite	Quartz	Dolomite	Talc
S-263	1	1	1	1	0
	2	1	0	1	0
	3	1	0	1	0
	4	1	1	1	1
	5	1	1	1	0
	6	1	1	1	0
	7	1	1	1	0
	8	1	0	1	0
	9	1	1	1	1
	10	1	1	1	0
	11	1	1	1	1
	12	1	1	1	1
		Quartz	**Talc**	**Chlorite**	**Dolomite**
S-278	1	1	1	1	0
	2	1	1	1	0
	3	1	1	1	0
	4	1	1	1	1
	5	1	1	0	0
	6	1	1	0	0
	7	1	1	1	1
	8	1	1	1	0
	9	1	1	1	1
	10	1	1	1	0
	11	1	1	1	0
	12	1	1	1	0
	13	1	1	1	0
	14	1	1	0	0
	15	1	1	0	1

D

FTIR vs. QEMSCAN Mineralogy

Each figure shows the modal mineralogy of per sample, measured using the FTIR data and the pixel approach and the modal mineralogy measured using the QEMSCAN.

S-135

FTIR		QEMSCAN	
Illite	35%	Carrollite	6,07
K-feldspar	29%	Chalcopyrite	9,68
Quartz	35%	Bornite	0,02
		Chalcocite	0,00
		Dolomite	0,29
		Fe Dolomite	0,02
		Apatite	0,13
		Magnesite	0,00
		Quartz	21,96
		K-feldspar	48,63
		Muscovite/Illite	8,39
		Biotite	1,06
		Phlogopite	0,01
		Magnesiochlorite	0,30
		Mg silicates	0,00

S-146

FTIR		QEMSCAN	
Quartz	21%	Carrollite	22,31
Dolomite	36%	Chalcopyrite	18,55
Muscovite	42%	Bornite	0,02
		Chalcocite	0,01
		Dolomite	15,03
		Fe Dolomite	0,86
		Apatite	0,96
		Magnesite	0,00
		Quartz	16,86
		K-feldspar	2,30
		Muscovite/Illite	17,32
		Biotite	1,10
		Phlogopite	0,79
		Magnesiochlorite	2,15
		Mg silicates	0,11

S-188

FTIR		QEMSCAN	
Quartz	30%	Carrollite	30,85
Dolomite	9%	Chalcopyrite	0,89
Chlorite	30%	Bornite	9,83
Talc	30%	Chalcocite	0,68
		Dolomite	7,87
		Fe Dolomite	0,58
		Apatite	0,25
		Magnesite	0,03
		Quartz	12,41
		K-feldspar	0,00
		Muscovite/Illite	0,00
		Biotite	0,00
		Phlogopite	0,01
		Magnesiochlorite	17,28
		Mg silicates	18,14

Figure D.1: FTIR vs. QEMSCAN Mineralogy of S-135 , S-146 and S-188

S-200

FTIR		QEMSCAN	
Quartz	31%	Carrollite	44,74
Dolomite	31%	Chalcopyrite	0,35
Chlorite	12%	Bornite	4,79
Talc	27%	Chalcocite	0,03
		Dolomite	24,07
		Fe Dolomite	0,66
		Apatite	1,60
		Magnesite	0,09
		Quartz	13,38
		K-feldspar	0,00
		Muscovite/Illite	0,00
		Biotite	0,00
		Phlogopite	0,00
		Magnesiochlorite	3,24
		Mg silicates	6,69

S-237

FTIR		QEMSCAN	
Quartz	50%	Carrollite	9,34
Dolomite	50%	Chalcopyrite	0,13
		Bornite	1,05
		Chalcocite	0,02
		Dolomite	55,36
		Fe Dolomite	0,58
		Apatite	0,05
		Magnesite	0,07
		Quartz	32,59
		K-feldspar	0,00
		Muscovite/Illite	0,00
		Biotite	0,00
		Phlogopite	0,00
		Magnesiochlorite	0,14
		Mg silicates	0,59

S-249

FTIR		QEMSCAN	
Quartz	23%	Carrollite	13,52
Dolomite	26%	Chalcopyrite	3,50
Chlorite	26%	Bornite	51,63
Talc	26%	Chalcocite	0,19
		Dolomite	16,82
		Fe Dolomite	0,14
		Apatite	0,03
		Magnesite	0,03
		Quartz	7,44
		K-feldspar	0,00
		Muscovite/Illite	0,00
		Biotite	0,00
		Phlogopite	0,00
		Magnesiochlorite	3,34
		Mg silicates	2,28

Figure D.2: FTIR vs. QEMSCAN Mineralogy of S-200, S-237 and S-249

S-256

FTIR		QEMSCAN	
Quartz	57%	Carrollite	17,84
Dolomite	14%	Chalcopyrite	3,67
Chlorite	29%	Bornite	30,83
		Chalcocite	4,37
		Dolomite	4,80
		Fe Dolomite	0,45
		Apatite	0,13
		Magnesite	0,01
		Quartz	17,34
		K-feldspar	0,00
		Muscovite/Illite	0,00
		Biotite	0,00
		Phlogopite	0,52
		Magnesiochlorite	13,47
		Mg silicates	1,31

S-258

FTIR		QEMSCAN	
Quartz	52%	Carrollite	0,03
Dolomite	48%	Chalcopyrite	0,21
		Bornite	0,03
		Chalcocite	0,12
		Dolomite	66,49
		Fe Dolomite	26,37
		Apatite	0,26
		Magnesite	0,00
		Quartz	4,14
		K-feldspar	0,00
		Muscovite/Illite	0,00
		Biotite	0,01
		Phlogopite	0,00
		Magnesiochlorite	0,54
		Mg silicates	0,06

S-263

FTIR		QEMSCAN	
Quartz	24%	Carrollite	14,65
Dolomite	32%	Chalcopyrite	2,20
Chlorite	32%	Bornite	8,62
Talc	11%	Chalcocite	3,12
		Dolomite	9,53
		Fe Dolomite	0,90
		Apatite	0,78
		Magnesite	0,00
		Quartz	5,62
		K-feldspar	0,01
		Muscovite/Illite	0,00
		Biotite	0,00
		Phlogopite	0,19
		Magnesiochlorite	45,93
		Mg silicates	1,79

Figure D.3: FTIR vs. QEMSCAN Mineralogy of S-256, S-258 and S-263

S-273

FTIR		QEMSCAN	
Quartz	50%	Carrollite	34,17
Dolomite	50%	Chalcopyrite	4,71
		Bornite	0,06
		Chalcocite	0,01
		Dolomite	5,16
		Fe Dolomite	0,01
		Apatite	0,04
		Magnesite	0,00
		Quartz	55,05
		K-feldspar	0,00
		Muscovite/Illite	0,00
		Biotite	0,00
		Phlogopite	0,00
		Magnesiochlorite	0,17
		Mg silicates	0,37

S-275

FTIR		QEMSCAN	
Quartz	45%	Carrollite	5,93
Dolomite	42%	Chalcopyrite	1,39
Serpentine	13%	Bornite	0,09
		Chalcocite	0,00
		Dolomite	19,28
		Fe Dolomite	0,18
		Apatite	0,47
		Magnesite	0,07
		Quartz	68,62
		K-feldspar	0,00
		Muscovite/Illite	0,00
		Biotite	0,00
		Phlogopite	0,00
		Magnesiochlorite	1,56
		Mg silicates	2,20

S-278

FTIR		QEMSCAN	
Quartz	33%	Carrollite	8,93
Dolomite	9%	Chalcopyrite	8,60
Chlorite	24%	Bornite	0,06
Talc	33%	Chalcocite	0,01
		Dolomite	1,73
		Fe Dolomite	0,04
		Apatite	0,05
		Magnesite	0,01
		Quartz	27,55
		K-feldspar	0,00
		Muscovite/Illite	0,00
		Biotite	0,00
		Phlogopite	0,00
		Magnesiochlorite	17,42
		Mg silicates	34,83

Figure D.4: FTIR vs. QEMSCAN Mineralogy of S-273, S-275 and S-278

S-279

FTIR		QEMSCAN	
Quartz	38%	Carrollite	88,11
Carrollite	62%	Chalcopyrite	2,78
		Bornite	0,05
		Chalcocite	0,03
		Dolomite	0,41
		Fe Dolomite	0,03
		Apatite	0,05
		Magnesite	0,00
		Quartz	6,38
		K-feldspar	0,00
		Muscovite/Illite	0,00
		Biotite	0,00
		Phlogopite	0,00
		Magnesiochlorite	0,91
		Mg silicates	0,73

S-308

FTIR		QEMSCAN	
Quartz	37%	Carrollite	49,88
Dolomite	34%	Chalcopyrite	0,77
Serpentine	29%	Bornite	8,27
		Chalcocite	6,94
		Dolomite	13,69
		Fe Dolomite	0,28
		Apatite	0,23
		Magnesite	0,02
		Quartz	14,64
		K-feldspar	0,02
		Muscovite/Illite	0,00
		Biotite	0,00
		Phlogopite	0,51
		Magnesiochlorite	2,73
		Mg silicates	0,68

S-314

FTIR		QEMSCAN	
Quartz	32%	Carrollite	71,96
Serpentine	34%	Chalcopyrite	0,53
Carrollite	34%	Bornite	10,06
		Chalcocite	0,15
		Dolomite	0,15
		Fe Dolomite	0,00
		Apatite	0,19
		Magnesite	0,00
		Quartz	11,28
		K-feldspar	0,00
		Muscovite/Illite	0,00
		Biotite	0,00
		Phlogopite	0,00
		Magnesiochlorite	3,14
		Mg silicates	2,22

Figure D.5: FTIR vs. QEMSCAN Mineralogy of S-279, S-308 and S-314

S-345				S-360				S-387			
FTIR		QEMSCAN		FTIR		QEMSCAN		FTIR		QEMSCAN	
Quartz	35%	Carrollite	37,61	Quartz	50%	Carrollite	13,46	Quartz	57%	Carrollite	4,00
Chlorite	30%	Chalcopyrite	1,09	Dolomite	50%	Chalcopyrite	0,61	Dolomite	33%	Chalcopyrite	1,20
Talc	35%	Bornite	0,06			Bornite	7,54	Serpentine	10%	Bornite	5,18
		Chalcocite	0,02			Chalcocite	0,03			Chalcocite	0,03
		Dolomite	0,15			Dolomite	54,46			Dolomite	12,64
		Fe Dolomite	0,01			Fe Dolomite	2,45			Fe Dolomite	0,14
		Apatite	0,10			Apatite	0,49			Apatite	0,08
		Magnesite	0,01			Magnesite	0,01			Magnesite	0,01
		Quartz	14,38			Quartz	20,11			Quartz	67,62
		K-feldspar	0,01			K-feldspar	0,00			K-feldspar	0,00
		Muscovite/Illite	0,00			Muscovite/Illite	0,00			Muscovite/Illite	0,00
		Biotite	0,00			Biotite	0,00			Biotite	0,00
		Phlogopite	0,54			Phlogopite	0,00			Phlogopite	0,00
		Magnesiochlorite	15,87			Magnesiochlorite	0,29			Magnesiochlorite	0,10
		Mg silicates	29,20			Mg silicates	0,26			Mg silicates	8,57

Figure D.6: FTIR vs. QEMSCAN Mineralogy of S-345, S-360 and S-387

S-403				S-421				S-426			
FTIR		QEMSCAN		FTIR		QEMSCAN		FTIR		QEMSCAN	
Quartz	40%	Carrollite	51,10	Quartz	50%	Carrollite	50,34	Illite	29%	Carrollite	19,09
Dolomite	20%	Chalcopyrite	1,35	Serpentine	50%	Chalcopyrite	0,53	K-feldspar	32%	Chalcopyrite	6,78
Serpentine	40%	Bornite	3,02			Bornite	6,12	Quartz	39%	Bornite	0,02
		Chalcocite	0,03			Chalcocite	0,29			Chalcocite	0,00
		Dolomite	3,79			Dolomite	35,51			Dolomite	0,01
		Fe Dolomite	0,08			Fe Dolomite	1,21			Fe Dolomite	0,00
		Apatite	4,92			Apatite	0,06			Apatite	3,75
		Magnesite	0,01			Magnesite	0,57			Magnesite	0,00
		Quartz	27,57			Quartz	0,24			Quartz	22,99
		K-feldspar	0,00			K-feldspar	0,00			K-feldspar	30,47
		Muscovite/Illite	0,00			Muscovite/Illite	0,00			Muscovite/Illite	14,74
		Biotite	0,00			Biotite	0,00			Biotite	0,37
		Phlogopite	0,00			Phlogopite	0,00			Phlogopite	0,04
		Magnesiochlorite	2,62			Magnesiochlorite	0,34			Magnesiochlorite	0,32
		Mg silicates	5,19			Mg silicates	3,95			Mg silicates	0,02

Figure D.7: FTIR vs. QEMSCAN Mineralogy of S-403, S-421 and S-426

E
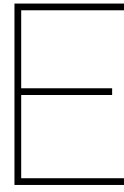
Comminution Samples Leeb Hardness Information

Information about the factors influencing Leeb Hardness and measured Leeb Hardness of the samples used in the comminution tests.

Table E.1: Information Influencing Leeb Hardness and Results Surface Hardness Tests Used in Comminution Experiments

Sample Bag	Number	Mass	Hits	Average Leeb	Max Leeb	Min Leeb	StDev	Adjustment Factor	Adjusted Leeb	Adjusted Average
MM 18	1	62.59	7	565	679	435	72	10.07	622	614
	2	73.29	10	509	642	420	76	9.28	556	
	3	69.30	7	560	602	523	34	9.58	613	
	4	43.87	4	593	701	394	139	11.77	662	
MM 23	1	147.17	8	680	753	581	58	6.28	722	686
	2	152.08	10	611	695	515	64	6.12	649	
MM 26	1	159.45	10	767	864	680	65	5.86	812	844
	2	103.01	5	811	819	802	7	7.9	875	
MM 29	1	101.30	7	765	806	650	55	7.96	826	830
	2	128.23	8	818	850	762	28	6.99	875	
	3	83.45	5	726	770	680	37	8.56	788	
MM 34	1	126.9	8	549	603	484	40	7.04	587	523
	2	64.83	5	457	565	396	65	9.91	502	
	3	75.32	3	438	473	383	48	9.13	478	

F

Simulation vs. Experimental Crusher Results

Particle Size Distribution deduced from the simulated and experimental crushing experiments.
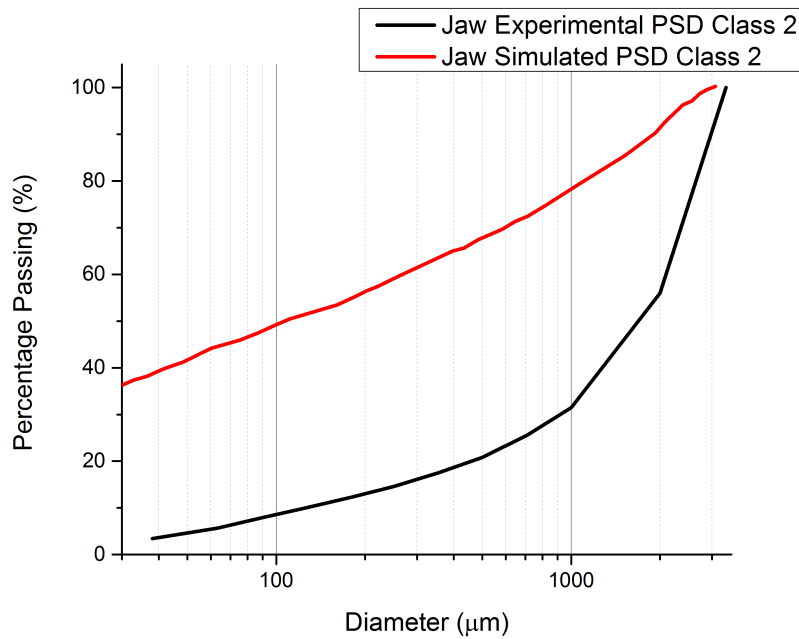

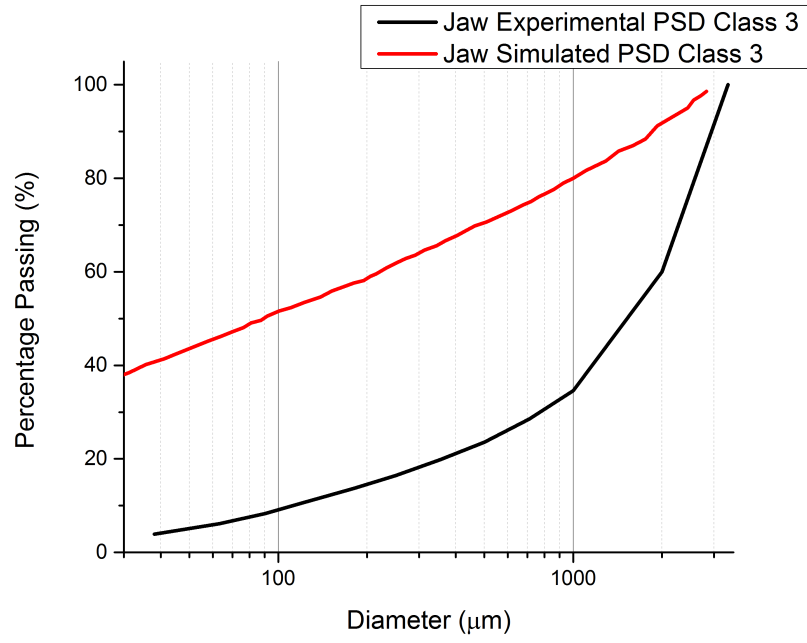Figure F.1: Simulation vs. Experimental Crusher PSD for Comminution Class 2

Figure F.2: Simulation vs. Experimental Crusher PSD for Comminution Class 3